FEATURE INVESTIGATION USING MICRO COMPUTED TOMOGRAPHY WITHIN MATERIALS

By

GHAZAL SOKHANSEFAT

Bachelor of Science in Civil Engineering, Surveying
K. N. Toosi University of Technology
Tehran, Iran
2010

Master of Science in Surveying Engineering/GIS
University of Tehran
Tehran, Iran
2013

Submitted to the Faculty of the
Graduate College of the
Oklahoma State University
in partial fulfillment of
the requirements for
the Degree of
DOCTOR OF PHILOSOPHY
May, 2018

FEATURE INVESTIGATION USING MICRO

COMPUTED TOMOGRAPHY WITHIN MATERIALS

Dissertation Approved:

Dr. M. Tyler Ley

Dr. Julie A. Hartell

Dr. Stephen A. Cross

Dr. Allen Apblett

ACKNOWLEDGEMENTS

After an intensive period of 4 years, it is my pleasure to acknowledge the role of many individuals who were instrumental for completion of my Ph.D. dissertation.

I would first like to acknowledge with gratitude, the support and love of my family – my husband, Masoud Moradian; my mother, Farideh; and my brothers, Rashid and Farshad. They all kept me going and I could have not done this work without them. I would also thank my late father and brother, Mansour and Farshid, for their assistance in my studies. Their memory will be with me always.

I would particularly like to single out my academic advisor, Dr. M. Tyler Ley for giving my first opportunity to work with his team. Without his help and counsel, always generously and unstintingly given, the completion of this work would not have been possible. I would also like to acknowledge helpful suggestion from my committee members, Dr. Julie A. Hartell, Dr. Stephen A. Cross, and Dr. Allen Apblett.

This work would not materialize without the funding received from the United State National Science Foundation (NSF). My thanks also go out to Dr. Joseph J. Biernacki (Tennessee Technological University) and Dr. Jason Weiss (Oregon State University) for their thoughtful comments on my papers.

Finally I would like to acknowledge my research lab colleagues: Qinang Hu, Daniel Cook, Riyadh Alturki, Amir Behravan, David Porter, Jake LeFlore, and Chad Stevenson. It was a great pleasure working with them and I appreciate their idea and help.

Name: GHAZAL SOKHANSEFAT

Date of Degree: MAY, 2018

Title of Study: FEATURE INVESTIGATION USING MICRO COMPUTED TOMOGRAPHY WITHIN MATERIALS

Major Field: CIVIL ENGINEERING

Abstract: This work uses micro computed tomography, as a direct non-destructive tool, to investigate internal 3D microstructure of different materials at multiple length scales to provide insights that are of interest to the scientific community on a variety of different problems.

In the first chapter, the 3D microstructure of three types of manufactured biomass microsphere particles was investigated before and after fast pyrolysis. The results show that the particle size, biomass components, and volume of air decrease during fast pyrolysis.

Next, concrete mixtures with different aggregate gradations and workability were prepared to study the aggregate packing in hardened concrete. The results show that low distance between aggregates and areas where no aggregates are observed correspond with mixtures of poor workability in the fresh concrete. These findings suggest that segregation of the coarse aggregate plays an important role in the workability of fresh concrete.

In addition, the role of critical degree of saturation and air void system on the crack propagation of cement mortar subjected to freeze-thaw cycles was investigated. The results show that cracking occurred in non-air entrained mortar subjected to a single freeze-thaw cycle when the critical degree of saturation was near 100%. These microcracks mostly initiate and propagate from the paste-aggregate interface or from within aggregate. In addition, materials were observed to form within the pores after freezing.

Finally, the role of air void system on the freeze-thaw damage of the cement paste was investigated. The results show that severe frost damage occurred in the surface of the non-air entrained cement paste ponded with KI solution after 63 freeze-thaw cycles. It was also observed that the average distance between air voids in the non-air-entrained was ≈ 1.8x higher than the average distance between air voids in the air-entrained samples. In addition, most of the air voids (≈ 75%) in both non-air-entrained and air-entrained samples are distributed in size ranges between 15 to 60 μm.
These observations show that X-ray imaging is a powerful method that provides new insights into physical properties and morphology of biomass particles, workability of flowable concrete, and freeze-thaw performance of concrete.

TABLE OF CONTENTS

Chapter Page

Chapter Page

LIST OF TABLES

Table Page

LIST OF FIGURES

Figure Page

Figure Page

Figure Page

CHAPTER I

INTRODUCTION

1.1. Introduction

Demands for materials with desirable properties are important for almost all industries. They open the door to new technologies in various fields such as chemical, construction, biomedical, and electrical engineering. Properties of a material are related to its structure [1, 2]. Therefore, better understanding of the microstructure of a material will allow insights into improving their characteristics and producing materials that are high quality, sustainable and cost-efficient.

The smallest particle size that can be seen with the unaided human eye is 0.1 mm (100 Micron) [3]. This is roughly equal to the width of 2 human hairs. However, a range of microscopy techniques have been developed to investigate the microstructure of materials. Optical or light microscope was the first generation of microscope to uses visible light and a system of lenses to observe small objects [4]. Further developments came with electron microscopy such as scanning electron microscopy (SEM) or transmission electron microscopy (TEM) [5, 6]. Although these techniques provide images with high resolutions, the observations can be only made on the exposed surface and often in high vacuum and with special sample preparation. These observations may not necessarily be representative of the material being investigated [7, 8]. What is needed is a technique that investigates the 3D microstructure of materials with minimal sample preparation.

X-ray computed tomography (XCT) is a powerful non-destructive tool that can be used to investigate the 3D microstructure of materials. It has been widely used in medical science to investigate biological organisms [9-11]. This method has also been used to study construction materials. Some examples include cement hydration [10, 12], aggregate spatial distribution [13-15], transport properties [16, 17], crack propagation [18-20], and air void distribution [21-23]. In this method, a series of 2D X-ray radiographs are captured from different viewing angles and the collected data sets are used to build a 3D measurement of the internal structure called a tomograph. The tomograph can be then used for qualitative and quantitative analyses [24-27]. The gray values in the produced images corresponds to X-ray absorption which is a function of density and composition of the material [28, 29]. The gray value contrast can be used to separate the materials into different constituent phases [15, 19, 21].

In this dissertation, XCT is used in to study different features within materials. First, it is used to investigate 3D microstructure of manufactured biomass microsphere particles before and after fast pyrolysis. Next, characterization of aggregate gradation in hardened concrete mixtures was investigated. In addition, it is used to provide 3D measurements of Portland cement mortar and paste subjected to freeze-thaw cycles.

These observations show that XCT is a novel and powerful method that provides new insights into the physical properties and morphology of materials and is a step to improve material characteristics. These 3D measurements can also help with the development of different models for materials.

1.2. Research Objectives

Four fundamental tasks can be drawn from this work:

1. 3D microstructure of the three spray dried biomass sources – switchgrass, crystalline cellulose, and tall fescue before and after pyrolysis to understand thermal transformations for these different materials.

2. The effect of aggregate packing on the workability of concrete mixtures.

3. The role of critical degree of saturation (DOS) and air void system on the crack propagation of Portland cement mortar subjected to freeze-thaw cycles.

4. The role of air void system on the freeze-thaw damage of the cement paste.

CHAPTER II

MICROSTRUCTURE OF BIOMASS PARTICLES BEFORE AND AFTER FAST PYROLYSIS AS OBSERVED BY X-RAY COMPUTED TOMOGRAPHY

Abstract

This work uses X-ray computed tomography (XCT) to study the 3D microstructure of manufactured biomass microsphere particles before and after fast pyrolysis. The XCT method was used for the direct non-destructive 3D imaging at a spatial resolution of 1 μm/voxel of three types of biomass particles in raw and charred conditions: switchgrass, crystalline cellulose, and tall fescue. Based on the investigation of eight individual particles from each biomass type, three main constituents were identified: air voids, biomass, and high absorption materials. The results show that the particle size, biomass components, and volume of air decrease during fast pyrolysis. These observations provide new insights into physical properties and morphology of biomass particles that can guide the development of biomass pyrolysis models that include morphological changes and associated effects.

Keywords: X-ray Computed Tomography, Segmentation, Fast pyrolysis, porosity, Biochar.

2.1. Introduction

Biofuels derived from renewable carbonaceous resources have become a widely studied subject

for energy applications such as green and alternative fuels [30-35]. Annually, 220 billion tons of waste biomass are produced in the world [36, 37]. Annual biomass availability in the United States is about 680 million dry tons, which is enough to produce, e.g. 54 billion gallons of ethanol or 19% of the 2010 U.S power consumption [38]. The U.S. Department of Energy hopes to replace 30% of fossil fuels with biofuels by 2030 [39, 40]. The most common resources of waste biomass are wood, agricultural residue, wood waste, and food waste [36, 41, 42]. Due to the cost-effectiveness of biofuel feed sources, producing liquid transportation fuels from agricultural residue, wastes, and energy crops such as straws and forage crops, e.g. switch grass and tall fescue, continues to be investigated [43-46].

Fast pyrolysis, the method that converts biomass to valuable products such as bio-oil and biochar under fast heating rates, is an efficient way to reduce dependence on non-renewable petroleum feedstocks, which cause greenhouse gas emissions [47, 48]. Despite many efforts to develop biomass pyrolysis processes, there are still various fundamental challenges. One of the obstacles includes the commercialization of pyrolytic biofuels, which depend on the quality and stability of bio-oils [49, 50]. The varying nature of biomass feedstocks is another challenge of fast pyrolysis [39]. Numerous studies have concentrated on pyrolysis of cellulose, hemicellulose, and lignin the main components of biomass [51-56]. Previous research has developed kinetics models to predict the behavior of biomass pyrolysis [57-61]. However, the amounts of fast pyrolysis products are affected by the physical characteristics of the biomass including particle size, density and shape [citation]. Therefore, a better understanding of the microstructure of biomass before and after pyrolytic heating could offer improvements in the understanding of thermochemical conversion and pyrolysis product distribution. This information could also be valuable in modeling combustion reactions.

Among the various techniques for microstructure characterization of waste biomass, X-ray micro computed tomography (XCT) measurements have potential to provide important insights into

biomass microstructure. These measurements can be in the form of 2D radiographs or a 3D tomograph. In this method, a series of 2D X-ray radiographs are obtained from different viewing angles in the form of a stack of 2D sample slices and the results are used to create a 3D rendering of the internal structure called a tomograph [62, 63].

Recent research using XCT has provided important insights into fuel sources and their combustion products. Previous work wherein XCT and electron probe microanalysis were combined investigated the 3D microstructure and distribution of chemical constituents within fly ash particles, a waste product from coal combustion [21, 64]. Other work has used XCT to characterize oil shale pyrolysis [65-70].

The XCT results provide non-destructive measurements of different cross-sections that can be analyzed to extract quantitative and morphological information such as pore connectivity and size distribution and the percentages and distribution of different components within the biomass particle. One drawback to XCT is that it cannot directly measure the chemistry of the materials investigated. However, these materials will have different X-ray absorption and therefore different gray values based on their composition and density [21, 71].

This paper investigates three biomass sources – switchgrass, crystalline cellulose and tall fescue in raw and charred conditions. Samples were produced by a spray drying process developed by Zolghadr et al. [72]. The process involves the production of s biomass microspheres from finely milled biomass flour.

The aim of this paper is to study the 3D microstructure of the three spray dried biomass sources – switchgrass, crystalline cellulose, and tall fescue before and after pyrolysis. The insights from these measurements are critical to understand thermal transformations for these different materials. Such data sets could also provide much needed initial and final conditions for numerical models currently under development [73].

2.2. Methodology

2.2.1. Material and sample preparation

Three types of biomass particles including switchgrass, crystalline cellulose, and tall fescue in raw and charred conditions were examined. These microsphere samples were produced by a spray drying process developed by Zolghadr et al. [72]. In this process, all biomass particles are dried for 24 h at 60°C, and then cut into pieces ≈ 5 cm in length. Next biomass particles are ground in a coffee mill for 10 min to obtain the particles of ≈ 1 mm. Finally, the materials are ball milled using a SPEX SamplePrep 8000M Mixer/Mill with a 45 mL alumina milling vial with 9.53 mm spherical alumina milling media. For the ball milling of switchgrass and tall fescue, two 5.5 g lots of grounded material (with the size of ≈ 1 mm) from each biomass type were milled for 30 min. The resulting materials are combined and milled for 3.5 h to obtain a fine flour. Crystalline cellulose, however, was directly milled for 4 h since it had an acceptable starting particle size. The charred particles are produced from the pyrolysis of raw particles with a heating rate of 200◦C/min in maximum temperature 900°C and purge rate of 100 cc/min. Figure 2.1 shows an example of investigated particles in both the raw and charred condition.

Fig. 2.1. An example of switchgrass particles in raw and charred condition observed under an optical microscope.

For imaging, the biomass particles were placed on the tip of a graphite rod by using 5 min epoxy under an optical microscope. For each kind of biomass particle, one specimen with approximately 8 to 10 particles was prepared.

2.2.2. XCT

The tomographs of the biomass particles were collected with Xradia MicroXCT-410 from Zeiss. The scan setting for all biomass specimens used an X-ray generator voltage of 40 KeV with an exposure time of about 3 s per projection. Each tomograph consisted of 3200 projections. Depending on the field of view, the source and detector distance were varied and produced radiographs that varied from 0.70 to 0.95 μm per pixel. This means that a recognizable object is roughly three times this size.

The reconstruction process was performed by XMReconstructor and XM3d viewer software was used for 3D visualization of the reconstructed images. Figure 2.2 shows an example 3D view of raw switchgrass particles. The reconstructed 3D image and 3D slice view of a single switchgrass particle are also shown in Figure 2.2.

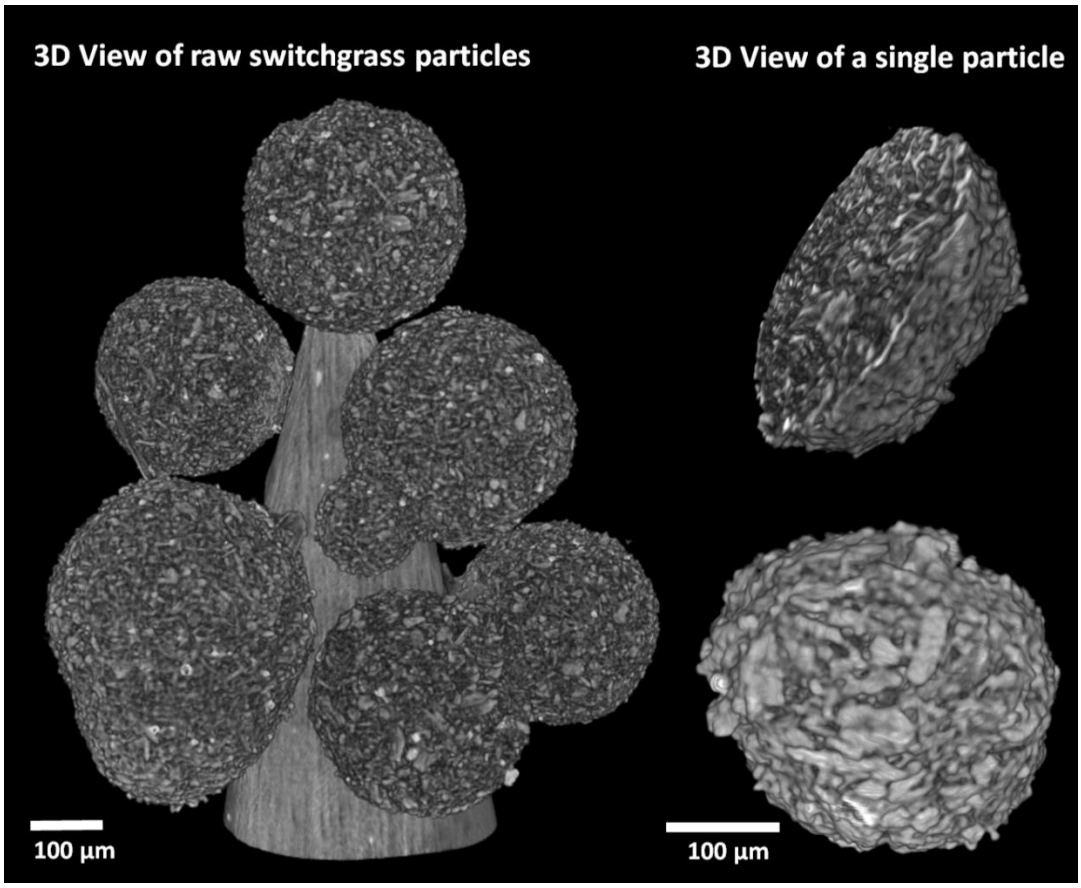

Fig. 2.2. A typical XCT dataset showing 3D tomography of switchgrass particles. An overview of a single particle, as well as a slice view, is shown on the right side.

2.2.3. Image Segmentation

While images of these materials are helpful, it is also possible to make quantitative statements about the distribution and makeup of the materials. To do this the XCT images must be segmented or separated into different components. The separation process of the different constituents is called segmentation.

Figure 2.3 shows an example of a 2D cross-section of the reconstructed tomograph and corresponding grayscale histogram for a raw switchgrass particle. Based on inspection of the cross-sections and the histogram, there are materials with three different and distinct gray values.

These different gray values represent materials with different densities: very low, intermediate and very high – these constituents have been labeled air, biomass, and high density materials respectively. These materials are noted in Figure 2.3.

The high absorption material has an X-ray absorption that is similar to those reported for metals [74-76]. While no chemical analysis was done for this work, it is expected that these materials are introduced by the grinding medium, which was aluminum oxide. It is not uncommon to find trace amounts of grinding medium within a material as the grinding media and mill erosion. The dark gray regions have the same gray values as the air around the particle and are thus identified as air voids. All intermediate gray values are assumed to be biomass particles or agglomerates.

There is some overlap in the gray values for the constituents mostly due to resolution effects at particle edges which makes quantitative segmentation more challenging. To decide on a useful segmentation range for each constituent, local regions of the cross-section were investigated that were clearly one of the three constituents. An example of such a "typical" region is shown as the dashed polygon in Figure 2.3. For each constituent, 20 different typical regions were selected and the average and standard deviation (STD) of the gray value for each constituent were recorded.

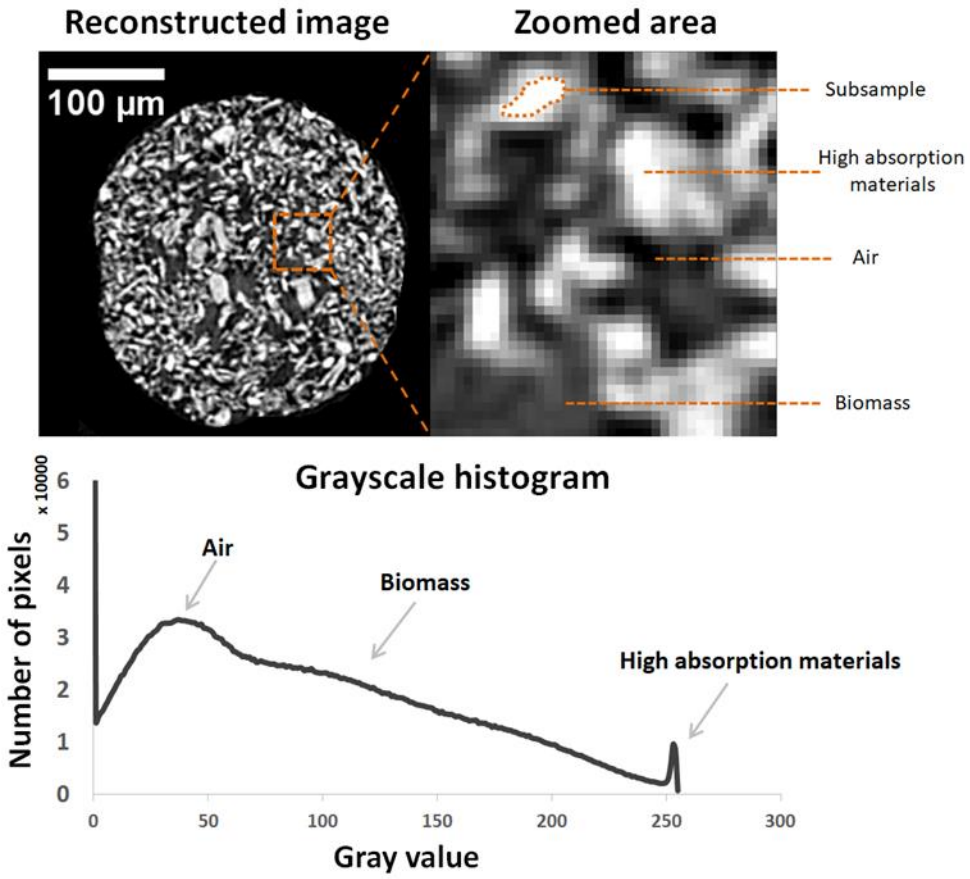

Fig. 2.3. An example of 2D cross-section of the reconstructed and corresponding grayscale histogram for a raw switchgrass particle. Zoomed area is highlighted as the dashed line in the reconstructed images.

Different multiples of the standard deviations were investigated to examine how it changes the results for each material. Figure 2.4 shows two example of 2D cross-sections, a zoomed area, and the segmented images of the zoomed area acquired from 2.5 standard deviations of the mean. The segmented image shows the voids in black, the high absorption in white, and the biomass in gray. The thresholds obtained from different standard deviations are shown in the grayscale histogram of the raw and charred switchgrass particles. If the gray value is assumed to be normally distributed for each biomass constituent, between 69% and 99.7% of the materials would be within one and three standard deviations away from the mean, respectively. Therefore, by visual

inspections of segmented images obtained from each threshold results, it was decided that the best threshold for segmentation is 2.5 standard deviations for the air and high absorption materials. The remaining material was then assigned to be biomass and is shown as gray in figure 2.4. An example segmentation result for each constituent in the raw and charred switchgrass particle is shown in Figure 2.5. This figure shows the voids in black, the high absorption in white, and the biomass in gray in the final segmentation results. This segmentation method was also applied to other biomass particle images. Based on the images in Figure 2.4, this method seems to slightly overestimate the amount of biomass and underestimate the air in the samples.

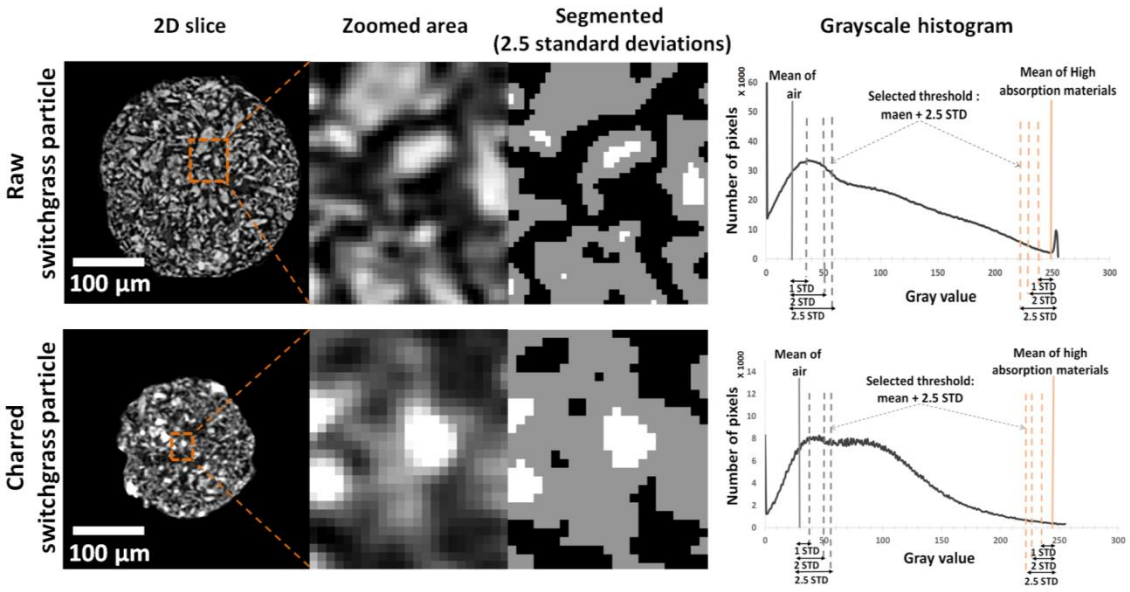

Fig. 2.4. An example of a 2D cross-section, a segmented image with the 2.5 standard deviations as a threshold, and corresponding grayscale histogram for a raw and charred switchgrass particle. Zoomed area is highlighted as orange dash line in the reconstructed images.

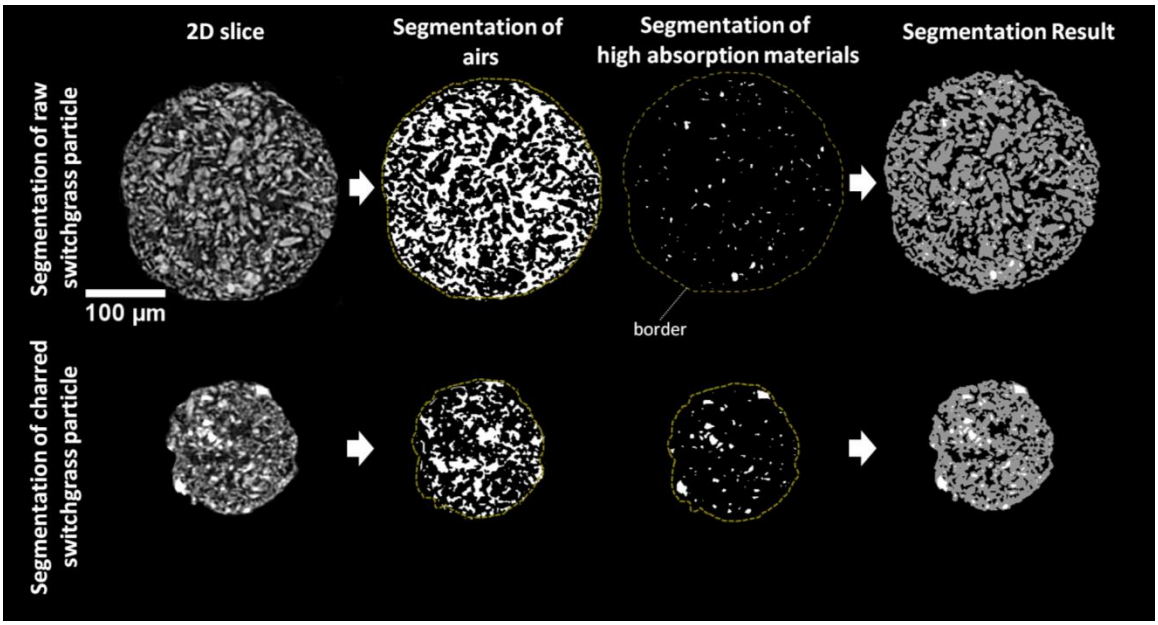

Fig. 2.5. An example of segmentation results for each constituent of raw and charred switchgrass particle.

The segmented biomass images were then used for further quantitative analyses such as the average volume distribution of biomass constituents at different distances from the surface of the particle. In this process, shells of equal thickness at the resolution of the scan were created from the surface toward the center of each particle. The volume percentage of high absorption, biomass, and air in each shell was then calculated by dividing the volume of each constituent in the shell to the total volume of the shell. The first few shells on the outside surface and near the core of the particle are not comparable to the bulk of the particle because of irregular surfaces and a low volume of material at the particle core. For this reason, these regions are not reported.

2.3. Results and Discussion

2.3.1. 3D Microstructure of biomass particles

Examples of 3D reconstructions of the segmented XCT data for all samples in raw and charred conditions are shown in Figure 2.6. In this figure, air is transparent, biomass is gray, and high absorption material is gold. Particles are not perfectly round and have some irregularities in their surface. In addition, different types of biomass have different apparent (overall) particle size. Table 2.1 shows the average particle size of biomass constituents and volume percentage of constituents for each biomass sample. The volume percentages were estimated by dividing the volume percentages of each constituent by the total volume of the particle.

In this table, switchgrass has the highest average particle size before charring and the lowest average particle size after charring. Therefore, it seems that the thermal process impacts the size of the switchgrass particles more than other biomass particles. In addition, switchgrass has the highest volume percentage of air voids and the lowest volume percentage of high absorption materials and biomass compared to the rest of the samples before pyrolysis. This means that the raw switchgrass particles are less dense than other biomass samples. On the other hand, the volume percentage of biomass and air in crystalline cellulose is similar to the tall fescue particles; however, crystalline cellulose has a higher volume percentage of high absorption materials compared to the tall fescue particles. Therefore, it seems that crystalline cellulose is denser than tall fescue in the raw form. Table 2.2 shows the density of raw biomass particles calculated by dividing the average mass of 100 individual particles for each biomass type to their measured average volume. In this calculation, the volume of each particle was determined by characterizing the effective diameter by taking three images of the same particle from different angles. According to Table 2.2, the density of crystalline cellulose is greater than tall fescue and the density of the tall fescue is greater than switchgrass which qualitatively matches the results obtained from XCT.

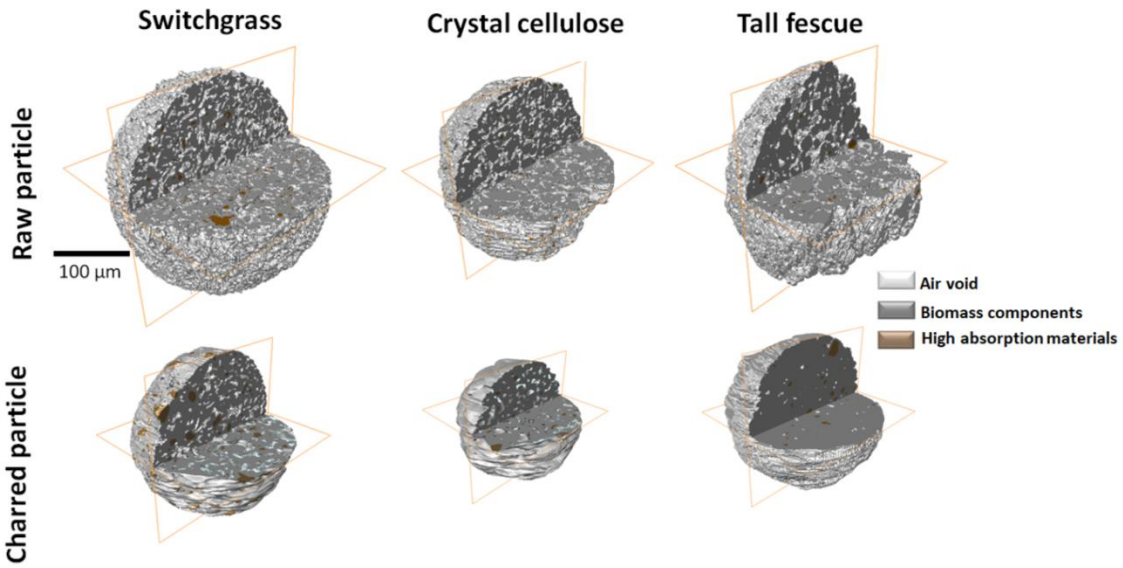

Fig. 2.6. 3D examples of segmented XCT data for all samples in raw and charred conditions.

Table 2.1. Average particle size and volume of biomass constituents for different biomass types in raw and charred conditions.

Biomass name		Number of particles	Average particle size (µm)	STD (µm)	Air voids		Biomass component*		High absorption materials	
					Volume (%)	STD	Volume (%)	STD	Volume (%)	STD
Switchgrass	Raw	8	261.1	16.4	36.9	4.81	62.3	4.8	0.8	0.3
	Charred	8	100.1	3.6	27.8	1.24	68.1	1.5	4.19	0.9
Crystalline cellulose	Raw	8	206.5	19.4	31.2	0.72	67.6	1.1	1.26	0.4
	Charred	8	118.1	5.3	18.9	0.73	78.7	0.8	2.46	0.2
Tall fescue	Raw	8	220.3	28.3	31.5	1.26	67.6	1.2	0.9	0.1
	Charred	8	147.3	8.1	2.5	0.51	95.5	1.1	2.01	0.7

*Biomass refers to the char (residue) fraction for “charred” samples and to the unreacted raw biomass for the “raw” samples.

Table 2.2. Average density of raw biomass particle.

Biomass name	Density (g/cc)
Raw switchgrass	1.281
Raw crystalline cellulose	1.334
Raw Tall fescue	1.289

2.3.2. Change in volume of biomass constituents

The 3D constituent data were used to investigate the average volume of the constituents taken from 8 particles for each type of biomass. This is shown in Figure 2.7. It should be noted that the variations observed between average volume shown in Figure 2.7 and volume percentage shown in Table 2.1 are caused by the differences in particle size or actual volume of the biomass particles before and after charring resulted in larger surface/volume in the charred particles compared to the raw particles.

According to this figure, by charring the particles, the average volume of the air and biomass decreased in all biomass types. The air volume in the charred switchgrass and crystalline cellulose is decreased by 4x and in the charred tall fescue particle, it is 34x lower than the volume of air voids in the raw condition. The biomass volume is 3x, 2x, and 1.5x lower than the volume of biomass in the raw condition in the charred switchgrass, crystalline cellulose, and tall fescue, respectively. Therefore, tall fescue particle has the highest decrease in average air volume (34x) and the lowest decrease in average biomass volume (1.5x) of the materials investigated.

By comparing the biomass particles, it was observed that the air volume in the charred switchgrass is 1.4x higher than the charred crystalline cellulose, and the air volume in the crystalline cellulose char is 6x higher than the tall fescue's char. For combustion, char with higher porosity has more combustion efficiency since the higher porosity can better control the rates of

diffusion of chemical species during the combustion process [77-80]. Therefore, it seems that the char of the switchgrass has the highest combustion efficiency and the tall fescue char has the lowest combustion efficiency among the investigated biomass particles. However, the reactivity of char is more complicated subject and it does not just depend on the porosity. It was reported that ash content and its distribution in the carbon matrix, active surface area, the carbon surface, and the carbon atom bonding are also controlling the reactivity of char [79, 80]. Therefore, further investigation is needed to better understand the reactivity of the char.

As expected, the average absolute volume of the high absorption materials is almost constant in both raw and charred samples since these high absorption materials are likely the residual materials from the grinding medium and the charring process is not expected to change these materials.

In addition, almost 98% of high absorption materials volume for raw and charred crystalline cellulose was found to be smaller than 200 μm^3. This finding suggests that high absorption materials size distribution in the raw and charred crystalline cellulose is finer (mostly smaller than 200 μm^3) compared to the volume distribution of other biomass particles. This could be caused by the difference between grinding process of crystalline cellulose and the other biomass particles. As mentioned in the method section, the crystalline cellulose particles were finer and therefore, it was ball milled less than other biomass particles which could create finer high absorption materials distribution in this sample compared to the other samples.

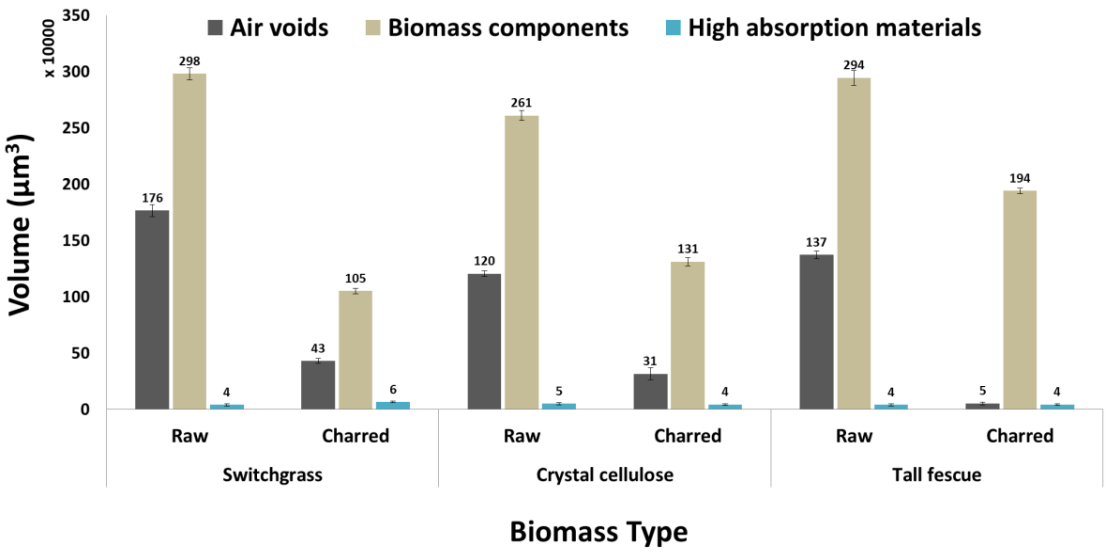

Fig. 2.7. Average volume taken from 8 individual particles for each biomass sample in raw and charred conditions. A standard error is reported for each calculation.

2.3.3. Spatial distribution of biomass constituents

The size distribution of each biomass constituents is also investigated and the results are shown in Figure 2.8. This figure shows the cumulative size distribution of the high absorption materials for all samples in raw and charred conditions and size distribution of air for charred tall fescue. This analysis shows that the air voids for all particles are interconnected except for the charred tall fescues. According to the air size distribution, ≈ 90% of the air voids in the charred tall fescue shown in Figure 2.8 are smaller than 400 µm. A 3D rendering and 2D slice of the segmented air voids for raw and charred conditions are shown in Figure 2.9 to visualize the connectivity of the air voids.

The connectivity of the voids of the biomass microspheres can prevent mass transfer problems during fast pyrolysis and avoid secondary reactions during the pyrolysis process.

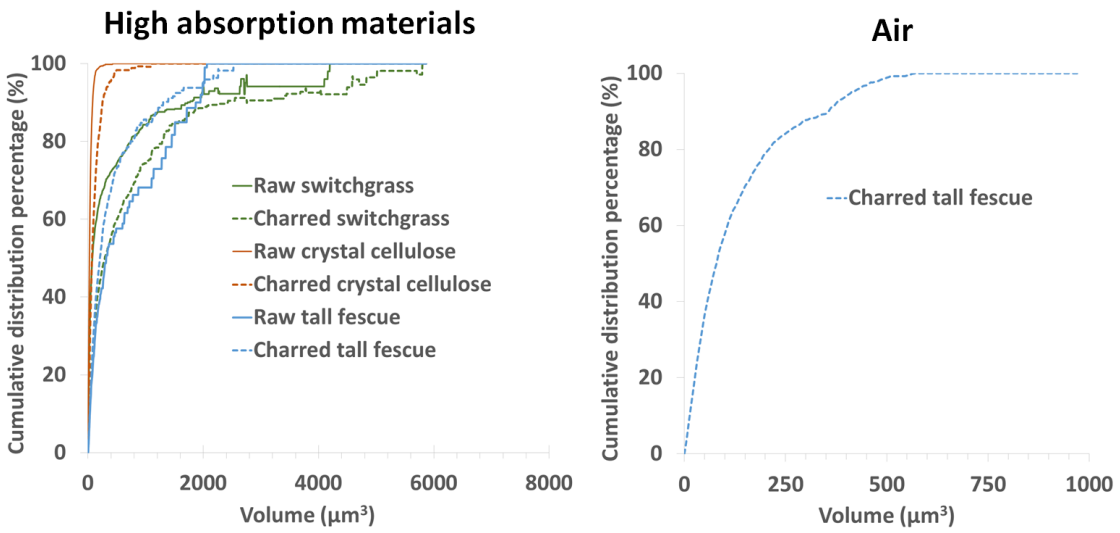

Fig. 2.8. Average size distribution of biomass constituents for all samples in raw and charred conditions.

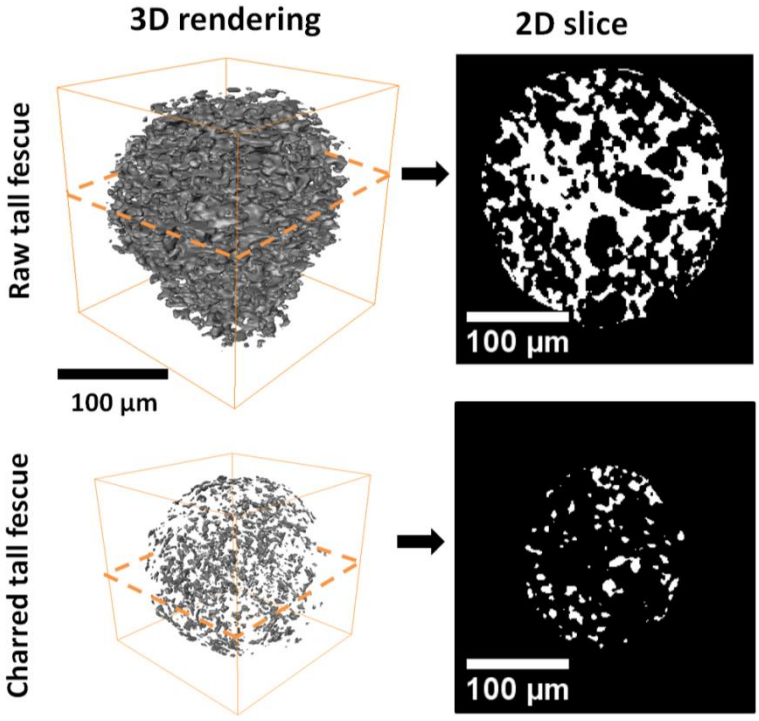

Fig. 2.9. 3D rendering and a 2D slice of the segmented air voids for different tall fescue particles before and after charring.

To give more insights, the volume distribution of each constituent at different distances from the surface by using a series of shells from the surface to the core is shown in Figure 2.10. In this figure, each curve is obtained by calculating the average from eight different particles for each kind of biomass sample.

The volume percentages of the air, biomass, and high absorption materials for all three types of raw biomass particles are almost constant at different distances from the surface of the raw biomass particles. In the charred condition, a similar trend was also observed except for the high absorption materials. This slight difference in the behavior of the high absorption may be caused by the reduced volume of the charred particles.

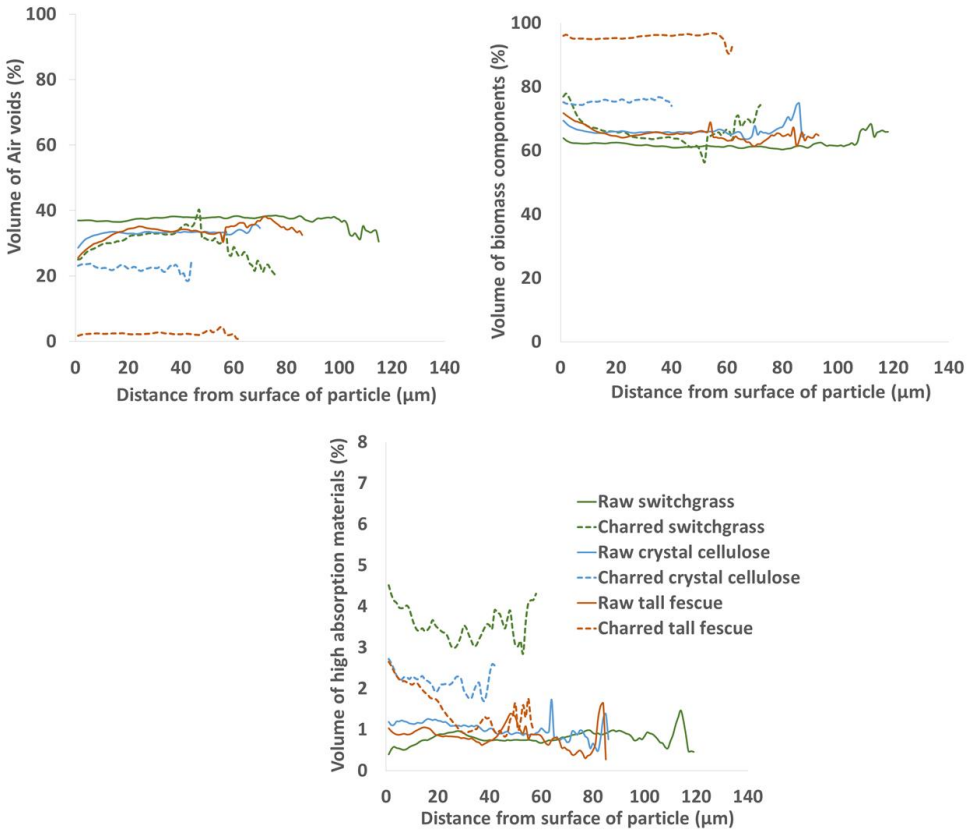

Fig. 2.10. Average volume distribution of biomass constituents at different distances from the surface of particles. Charred particles are shown with dash lines.

2.4. Summary and Conclusions

The 3D microstructure of switchgrass, crystalline cellulose, and tall fescue biomass particles in raw was charred condition are investigated using XCT. This work is unique as it can provide 3D quantitative insights into the volume and distribution of the constituents in the biomass particles before and after charring. The following conclusions could be drawn from this work:

- XCT is a useful tool to investigate the 3D microstructure of manufactured biomass particles before and after charring.
- The raw switchgrass particles have a lower density than other raw biomass samples since they had the highest air content and the lowest high absorption materials compared to the other raw particles.
- In contrast, raw crystalline cellulose was denser than raw tall fescue since it had higher high absorption materials compared to the tall fescue particles while the air content was similar in both particles.
- Switchgrass had a char with a porosity that was 1.4x higher compared to the crystalline cellulose char and 8.6x higher porosity compared to the tall fescue char.
- High absorption materials in crystalline cellulose in both raw and charred states are at least 2x smaller than the size of high absorption materials in other biomass particles.
- Except the charred tall fescue, air voids in all specimens are connected.
- The volume distribution of matter and voids was constant over the depth for the charred and raw materials.

These 3D microstructure findings will be useful for a better understanding of biomass microstructure and provide new insights into biomass characterization before and after charring.

Work is ongoing to investigate 3D microstructure for more kinds of biomass particles before and after charring for different pyrolysis conditions.

CHAPTER III

INVESTIGATION OF CONCRETE WORKABILITY THROUGH CHARACTERIZATION OF AGGREGATE GRADATION IN HARDENED CONCRETE USING X-RAY COMPUTED TOMOGRAPHY

Abstract

Concrete mixtures with different aggregate gradations and workability were prepared and X-ray computed tomography (XCT) is used to study the aggregate packing in hardened concrete. The workability of the mixtures was measured and then the aggregate spacing and distribution in the hardened concrete was investigated with a XCT scan of 40 μm resolution. These results show that low distance between aggregates and areas where no aggregates are observed correspond with mixtures of poor workability in the fresh concrete. These findings suggest that segregation of the coarse aggregate plays an important role in the workability of fresh concrete. These observations provide important insights into workability of flowable concrete. Furthermore, this work can help with the development of aggregate packing models.

Keywords: Aggregate size distribution, Segregation, workability, X-ray Computed Tomography, Segmentation.

3.1. Introduction

Typically, more than 70% of the volume of concrete is occupied by aggregates. This means that the optimization of aggregate gradation can improve concrete constructability, workability, cohesiveness, and reduce production expenses [81-85]. Optimized graded concrete can also reduce segregation and shrinkage of concrete by maximizing the volume of aggregate and minimizing the cement paste content required to provide adequate workability [86-88]. In addition, appropriate aggregate proportions can improve the workability and pumping of concrete [89].

Several empirical gradation charts have been developed to guide the design of optimized aggregate gradation such as the Power 45 Curve [90-92], Individual Percent Retained Chart [93, 94], Coarseness and Workability Chart [95, 96] and the Tarantula Curve [93, 97, 98]. The Tarantula Curve is the most recent of these design charts. It combines features of the other design procedures with several new insights and will be the primary tool used to investigate concrete mixtures. Furthermore, the limits of the Tarantula Curve were based on the workability limits of concrete mixtures. This means that when a mixture is outside of the limits of the Tarantula Curve then the mixture would be expected to decrease in workability compared to a mixture that has a gradation that is within the Tarantula Curve. In addition, recent work has shown that when the gradation of any coarse aggregate has more than 20% retained on a single sieve than there is observable decrease in the workability [99].

In this work the workability of concrete is characterized by measuring the rheological properties with the Bingham parameters - yield stress and plastic viscosity [100]. Rheometers typically measure torque and deflection angle of vane at a range of fixed angular velocities and correlate the results with rheological parameters [101, 102].

While these tools have proven to be useful to help design concrete mixtures, more information is needed to understand why certain aggregate gradations cause poor workability of the fresh concrete.

X-ray computed tomography (XCT) is a powerful and non-destructive tool that can be used to create 3D visualizations of the internal structure of materials. This technique has been widely used in previous work to identify the engineering properties of cementitious materials such as cement hydration [103, 104], concrete durability [105, 106], aggregate size distribution [14, 107, 108], air void distribution [109, 110], and crack propagation [18, 20, 111]. In this method, a 3D visualization or tomograph can be created by capturing 2D X-ray images or radiographs from different angles. The 3D data can then be used for qualitative and quantitative investigations [21, 112, 113]. The gray value in XCT tomographs correlates to the X-ray absorption of the material. The X-ray absorption can indicate the chemical composition and density of the imaged materials [71, 114]. The difference in the gray value or the contrast of the images can then be evaluated to separate the images into regions of different constituents. This process is called segmentation [21].

In this paper, concrete mixtures with similar mixture proportions but different aggregate distributions of the coarse aggregates are investigated. Next, hardened samples from these mixtures are investigated with XCT to determine the internal spacing and arrangement of the aggregates in the concrete to try and find a reason for the changes in workability.

3.2. Materials and Methods

3.2.1. Materials, mixture design, and aggregate gradation

All mixtures were prepared using ASTM C150 Portland cement (Type I), water to cementitious ratio (w/cm) of 0.45, with a 20% replacement of an ASTM C 618 Class C fly ash by mass. The chemical composition of the cement and fly ash are shown in Table 3.1. All coarse aggregates were a crushed limestone that is widely used in concrete production. The nominal maximum size of the coarse aggregate is 19 mm (0.75 in.) and 9.5 mm (0.375 in.) for the intermediate. A local natural sand was used as the fine aggregate.

In a subset of the samples, an X-ray contrast agent was added to the water to enhance the contrast between paste and aggregate in the XCT measurements. For this work, a KI salt was used to the mixture at 5% of the weight of the water used in the mixture design. This KI concentration was obtained from preliminary experiments to achieve an appropriate contrast between paste and aggregates.

The concrete mixtures investigated have the same volume of ingredients but have different aggregates size distributions. These details are shown in Table 3.2. The workability of the mixtures was determined by the ICAR rheometer and the slump test developed by The University of Texas at Austin [102].

The aggregate gradations used in this study and the limits from the Tarantula Curve are shown in Figure 3.1. In this figure, the first two samples contain no KI solution in their mixture design - while the rest of the samples have the KI solution in their mixture. The samples with the aggregate gradation outside, near the limit, and inside of the Tarantula Curve are shown in red, yellow, and green, respectively. The gray dashed-line represents the boundaries of the Tarantula curve. The fine and coarse sand limits are also shown.

The sample IDs are selected based on the gradation of aggregates and its comparison with the Tarantula Curve. The Mixture ID is used to give insight into the gradation of the mixture. The first entry indicates if the mixture is inside, outside, or at the limit of the Tarantula Curve. The next two numbers in the ID shows the percentage of aggregate retained on the 12.7 mm sieve (1/2″) and the 4.76 mm (#4) respectively. As an example, In_18,15 is a mixture inside of the Tarantula Curve with 18% aggregates retained on the 12.7 mm sieve and 15% aggregates retained on the 4.76 mm sieve.

Table 3.1. Chemical composition of ordinary Portland cement.

	Chemical Composition (mass %)								Phase concentration (%)			
	SiO_2	CaO	Al_2O_3	MgO	Fe_2O_3	SO_3	K_2O	Na_2O	C_3S	C_2S	C_3A	C_4AF
Type I ordinary portland cement	21.1	62.1	4.7	2.4	2.6	3.2	0.3	0.2	56.7	17.8	8.16	7.8
Type C Fly Ash	16.95	40.98	17.22	10.28	7.4	2.41	0.17	1.13	-	-	-	-

Table 3.2. Summary of the mixture designs.

Mixture ID	Coarse (kg/m^3)	Int. (kg/m^3)	sand (kg/m^3)	Cement (kg/m^3)	Fly ash (kg/m^3)	Water (kg/m^3)
In_17,17	478	461	883	268	67	150
In_11,10	586	564	680	268	67	150
In_18,15	666	357	804	268	67	150
Limit_20,13	731	293	803	268	67	150
Limit_16,19	578	444	803	268	67	150
Out_22,10	804	221	803	268	67	150
Out_14,22	506	516	803	268	67	150

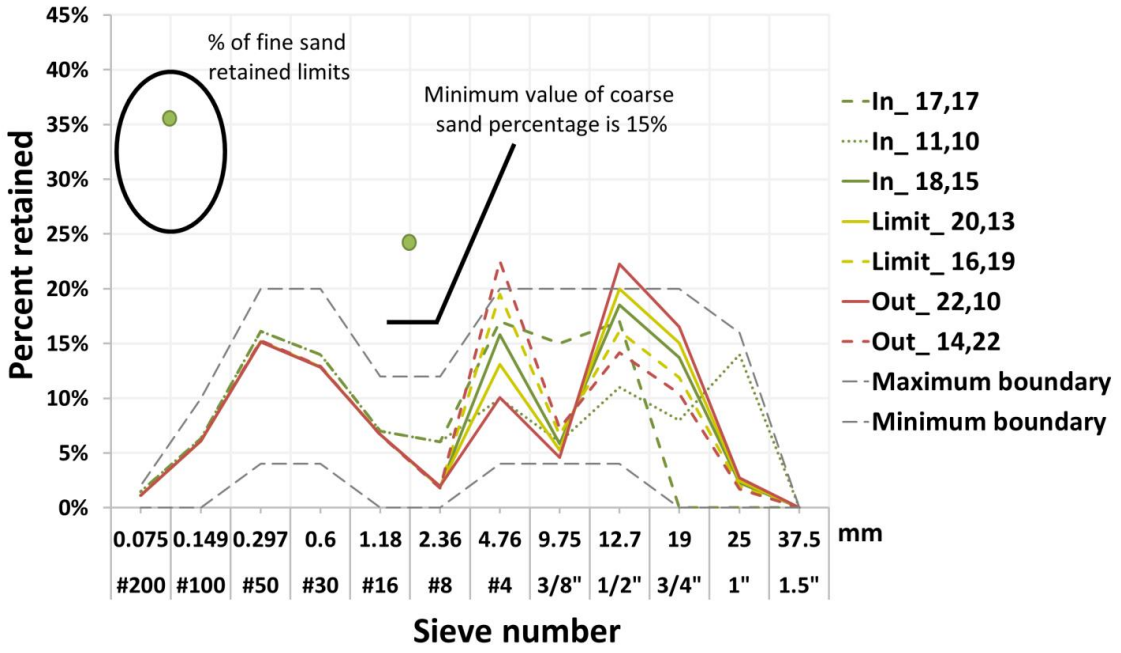

Fig. 3.1. Aggregate gradation of investigated samples. The Tarantula Curve boundaries are shown with the gray dashed lines.

3.2.2. Sample preparation and XCT

The concrete mixtures were cast in molds with nominal dimensions of 30.5 × 30.5 × 30.5 cm (12″ × 12″ × 12″). Typically, minimal sample preparation is needed when using XCT. However, the resolution of XCT images can be significantly affected by the sample thickness. Therefore, one core 6.35 cm (2.5 in.) in diameter and 15.24 cm (6 in.) in height were drilled from each specimen and used for the experiment. This is shown in Figure 3.2.

Each specimen was then scanned by a ZEISS XRADIA 410 with photon energy of 150 keV at a spatial resolution of 40 μm/voxel. The scan settings are summarized in Table 3.3. The imaged volume was a cylinder 4.37 cm (1.72 in.) in diameter and 4.4.37 cm (1.72 in.) in height located in the middle of the specimen as shown in Figure 3.2. The analyses were conducted on a 3 × 3 × 3 cm (1.2″ × 1.2″ × 1.2″) cube from the core of the imaged volume as the volume of interest (VOI) to avoid edge artifacts. In addition, another VOI with the same size from another region of the

samples Out_22,10 and Out_14,22 were scanned to evaluate the repeatability of the observations. These two samples were selected as they had poor workability and the aggregate gradation was outside the recommended limits of the Tarantula Curve.

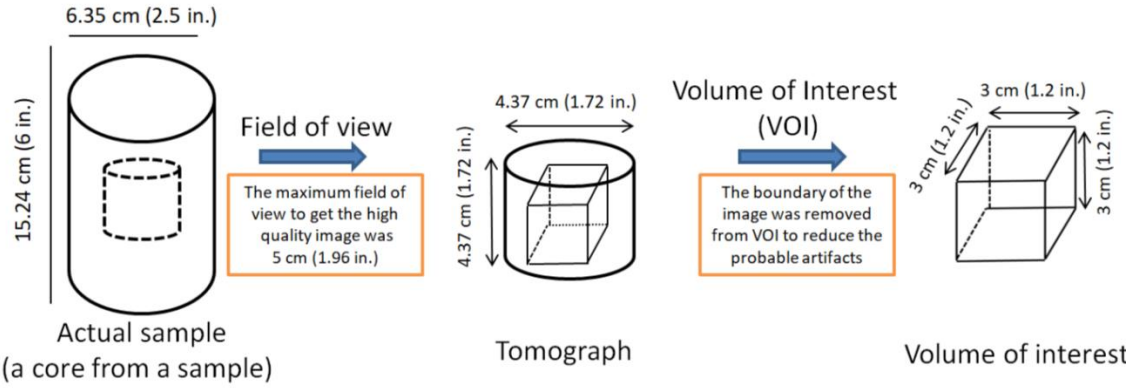

Fig. 3.2. Location and dimension of the imaged volume and VOI.

Table 3.3. X-ray scan setting.

Resolution	45 µm/pixel
Source energy	150 keV
Optical magnification	0.4X
Total scan time	4 h
Number of projections	2800
Exposure time	3.5 s

The XCT datasets were then reconstructed by XMReconstructor software package of Zeiss XRADIA 410 in order to create a stack of 2D slices. Figure 3.3 shows an example of 3D rendering, a 2D reconstructed image, and a histogram of the gray value in the 3D data set. The constituents with higher X-ray absorptions appear with lighter gray value while the materials with a lower X-ray absorption appear with darker gray value.

The major concrete constituents are air voids, aggregates, and OPC paste. The air voids have the lowest X-ray absorption while the aggregates have the highest X-ray absorption in XCT dataset.

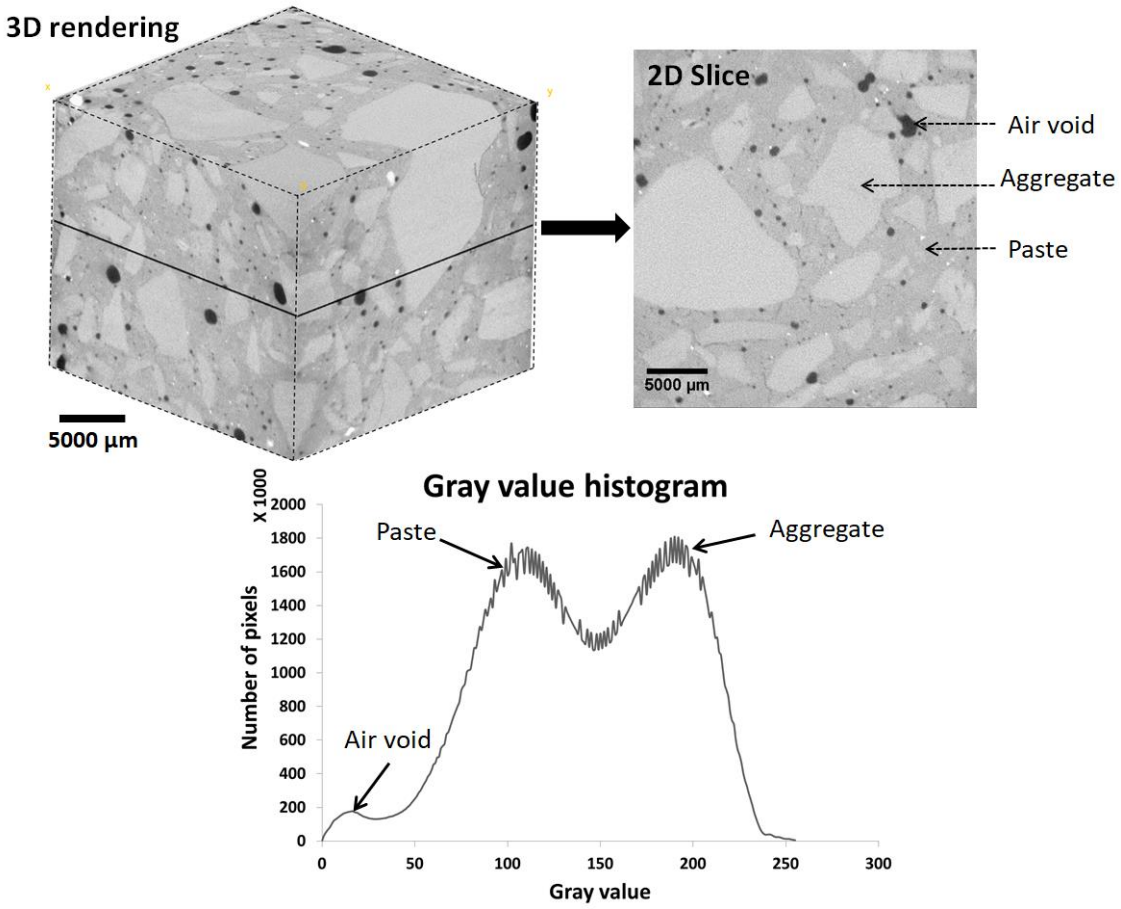

Fig. 3.3. A typical XCT dataset showing 3D rendering, 2D cross section of the reconstructed image, and corresponding gray scale histogram.

3.2.3. Segmentation and constituent data analysis

A multistep segmentation method is used to separate concrete constituents. First, a median filter was used to reduce the noise while preserving the edges. The segmentation method used for each component is discussed in the following sections.

3.2.3.1. Segmentation of air voids

Using a single gray value is a common way in image analysis to segment or separate constituents from images. The Otsu method is the most common method to do this. In this popular method, a

single threshold value is selected by minimizing the mean square errors between the original and binarized images. More information about this method can be found in other publications [114-117]. This method works well for air void segmentation because there is minimal overlap between the air void and the aggregates and paste as shown in Figure 3.3. Figure 3.4 gives an overview of how this method is completed.

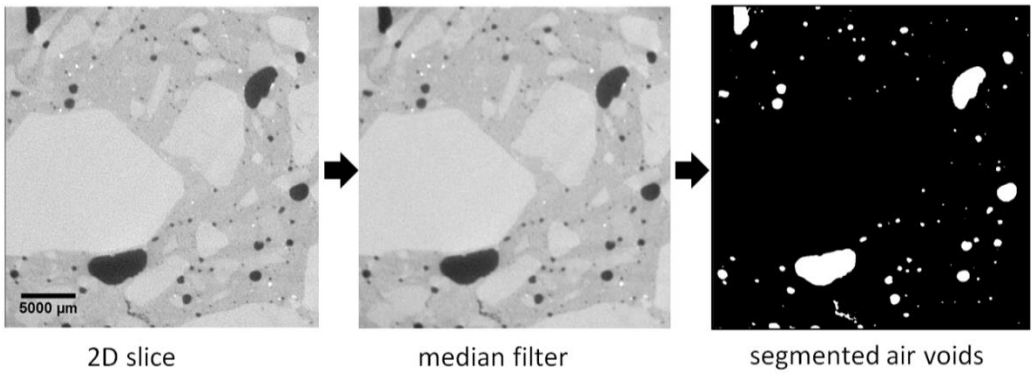

Fig. 3.4. Procedure for air void segmentation.

3.2.3.2. Segmentation of aggregates and paste

While the Otsu thresholding method was useful to segment the air voids, it was not helpful to separate the aggregates from the paste since the peaks in the gray level histogram overlap. In order to resolve this issue, image pre-processing and post-processing was used first and then the Otsu method was used. This procedure for fine and coarse aggregates is shown in Figure 3.5. To segment the coarse aggregates, a median filter with a radius of 5 pixels was applied on the reconstructed image. A larger radius filter creates intensive smoothing and eliminates some details; however, it is useful to identify the larger objects in the image. The Otsu thresholding was then applied to the filtered image. However, the resulting image contained some kind of distortion as shown in Figure 3.5. Therefore, two morphological analyses “erosion” and “fill holes” were used to distinguish aggregates and fill probable spots inside of the segmented aggregate created by noise. In this process, erosion removes voxels from the outer surface of the objects in a binary

image to separate the connected aggregates, while the filling operator fills holes in a binary image [118-120].

In order to segment the fine aggregates, a 3-pixel radius median filter with was used in the reconstructed image. The median filter removes noise in the reconstructed image without blurring the edge when the radius is small [121, 122]. The Otsu thresholding method was then applied to the filtered image. Next, the previously segmented coarse aggregates were subtracted and a morphological operator (erosion) was applied to the result to remove the connection between the fine aggregates. Finally, the results obtained from the fine and coarse aggregate segmentation were combined to generate the segmented aggregate image.

After identifying the air voids and the aggregates, the remaining materials were assumed to be the cement paste.

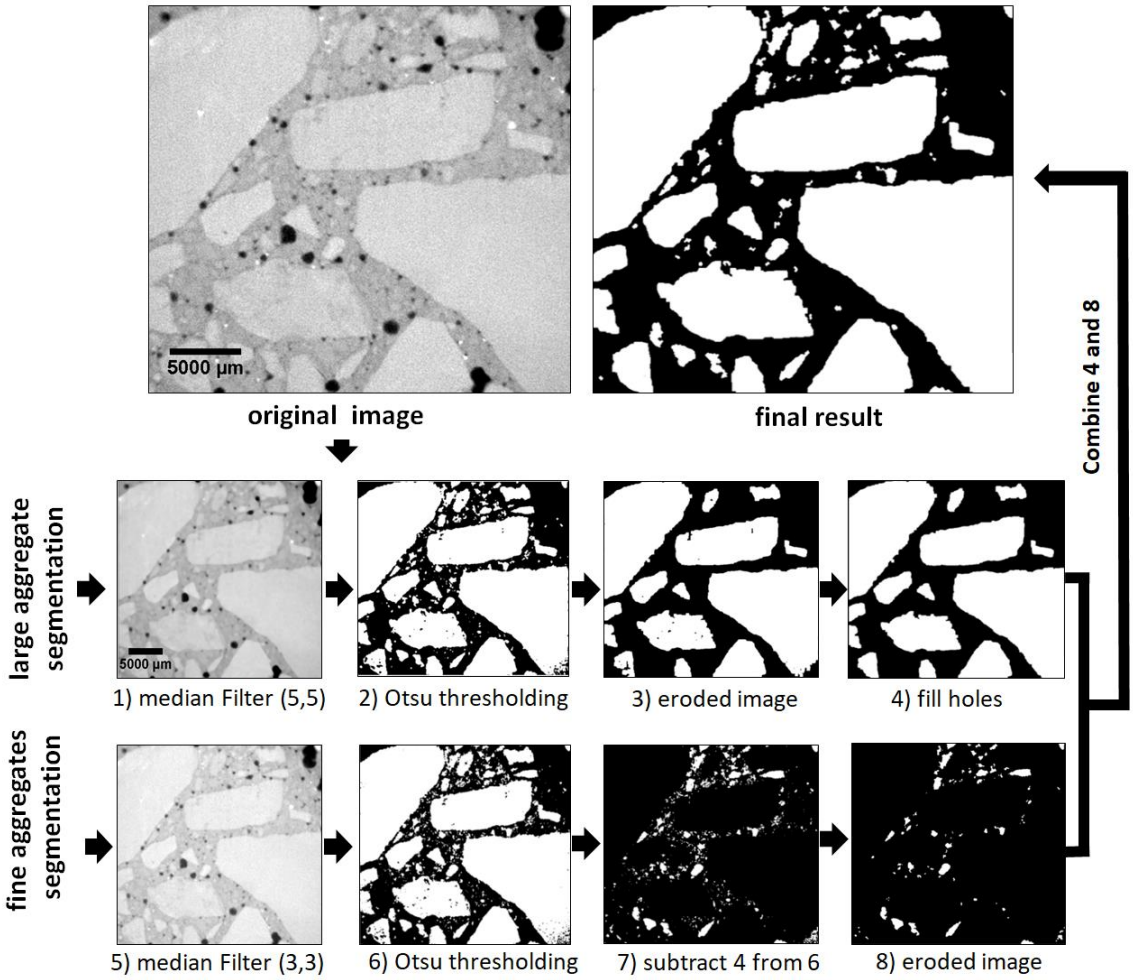

Fig. 3.5. Segmentation process of aggregates.

This aggregate segmentation method was successful to identify the majority of the coarse aggregates while there was an underestimation in the segmentation of fine aggregates. To further evaluate the accuracy of the method, the aggregate volume measured from the mixture design is compared to the volume measured by XCT in Table 3.4. The volume of coarse aggregate is on average different by 0.18 cm^3; however, the volume difference in the aggregates smaller than 4.76 mm (fine aggregates) is different by on average -5.09 cm^3.

This difference in the estimated volume of the fine aggregate could be caused by the low contrast between gray values of the paste and fine aggregate. This would estimate some fine aggregates

as paste. In addition, there are fine aggregates that are smaller than the resolution of the XCT (40 µm) and so these cannot be detected. To overcome these issues the paste and fine aggregate were combined and considered to be mortar. This allowed the average difference in the estimated mortar volume to be underestimated by-0.16 cm^3. This would still allow the air voids and coarse aggregates to still be investigated.

Table 3.4. Comparison of the aggregate volume in VOI calculated by XCT data and mixture design.

Mixture ID	Coarse aggregate Vol. (cm^3)			Mortar Vol. (cm^3)			Agg < 4.76 mm (fine agg) Vol. (cm^3)		
	XCT	Mixture Design	Diff.	XCT	Mixture design	Diff.	XCT	Mixture design	Diff.
In_17,17	12.12	11.37	0.75	14.88	15.63	-0.76	0.62	6.94	-6.32
In_11,10	12.29	11.37	0.92	15.71	15.63	0.08	0.84	6.94	-6.11
In_18,15	13.51	13.12	0.38	13.50	13.88	-0.38	0.57	5.18	-4.61
Limit_20,13	13.01	13.12	-0.11	13.93	13.88	0.05	0.32	5.18	-4.86
Limit_16,19	13.07	13.12	-0.05	13.93	13.88	0.05	0.24	5.18	-4.94
Out_22,10_1	13.07	13.12	-0.05	13.93	13.88	0.05	0.49	5.18	-4.69
Out_22,10_2*	13.05	13.12	-0.07	13.41	13.88	-0.47	0.35	5.18	-4.83
Out_14,22_1	13.11	13.12	-0.02	13.91	13.88	0.03	0.567	5.18	-4.61
Out_14,22_2**	13.21	13.12	-0.09	13.82	13.88	-0.06	0.6	5.18	-4.85
Average	12.94	12.73	0.18	14.11	14.27	-0.16	0.51	5.57	-5.09

***** Repeat scan of Out_22,10 sample.
****** Repeat scan of Out_14,22 sample.

3.2.3.3. Size and spatial distribution of aggregates

The 3D segmented XCT datasets were used to classify the aggregates based on their size. This process was able to investigate each aggregate in the hardened concrete and identify the size and location. This is similar to completing a digital sieve analysis. In this procedure, the 3D outer shell of each aggregate was identified. Next, the 3D distance between any two pixels on the outer shell of each aggregate was calculated and the maximum distance was identified as the aggregate size. Figure 3.6 shows the raw and segmented data set from the In_17,17 sample. In this figure,

different aggregate sizes are shown with different colors in the segmented image. It should be noted that because of the underestimation in the aggregates smaller than 4.76 mm (fine aggregates), the paste and fine aggregate are considered to be mortar. More information about 3D segmented dataset of other samples can be found in the Appendix A.

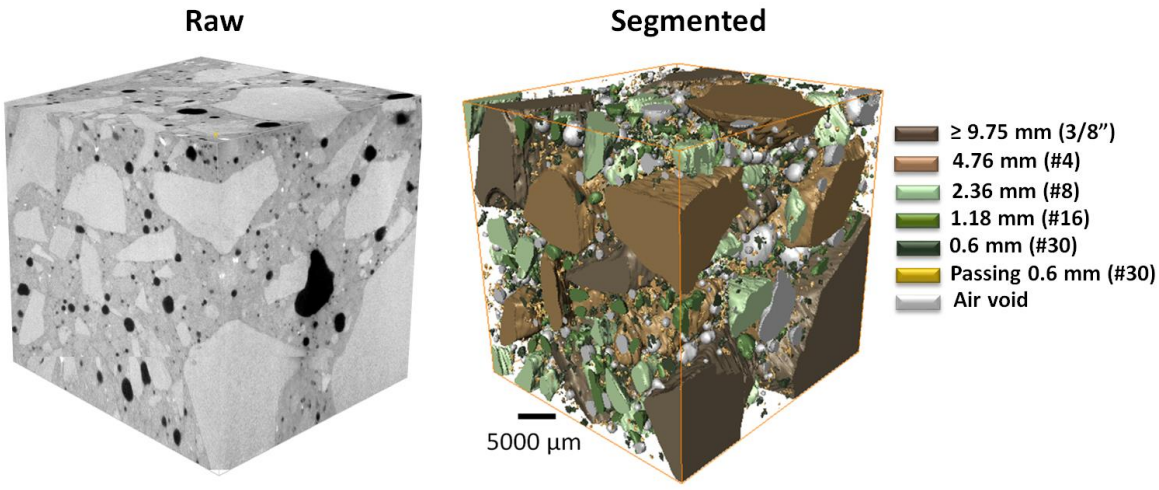

Fig. 3.6. 3D rendering of the raw and segmented XCT data obtained from In_17,17 sample.

The distance of aggregates in different samples was investigated by measuring the average distance between the surface of the aggregate in question and the nearest neighbor aggregate particle. The 2D schematic diagram of nearest-neighbor aggregate distance calculations is shown in Figure 3.7. The results are reported as cumulative plots and also as a distribution. Since this analysis is only focused on aggregates 4.76 mm or larger with all of these others treated as part of the mortar, then these numbers show the average thickness of the mortar between the coarse aggregates. A low average spacing of coarse aggregates means a small amount of mortar. A higher average spacing would mean a thicker layer of mortar between the aggregates. These values will be compared to the workability performance of the mixtures.

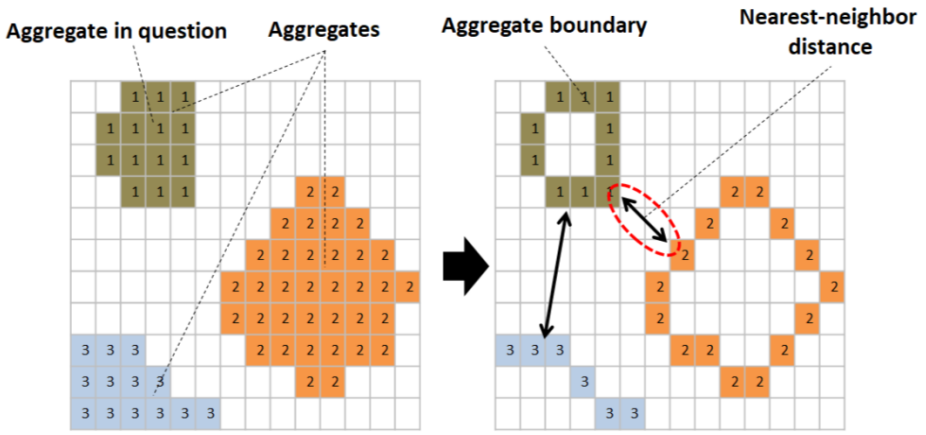

Fig. 3.7. 2D schematic diagram of nearest-neighbor aggregate distance calculation.

Also, the aggregate volume distributions at different cross sections in three directions were analyzed. In this process, the percentage of coarse aggregate volume in each cross section is calculated by dividing the number of pixels segmented as aggregate to the total number of pixels in that cross-section. As an example, for the aggregate volume distribution in z-direction, the aggregate volume distribution at different cross sections in x-y-plane from the origin of VOI along the z-axis was determined. This 3D analysis gives useful information about how aggregates are distributed along different directions within the concrete.

3.3. Results and Discussion

3.3.1. Workability measurements

Table 3.5 shows four different workability results of fresh concrete mixtures measured by slump and rheometer tests. In this table, each workability result is evaluated based on five different ranking shown in Table 3.6. More details about the workability ranking can be found in other publication [123].The average workability performance scales for each measurement is then reported as the overall workability shown in Table 3.5. As an Example, the static yield, dynamic

yield, plastic viscosity, and slump measured for sample In_18,15 were 1397.8 Pa, 471.1 Pa, 17.75 Pa/sec, and 190 mm, respectively. According to Table 3.6, the workability performance scale of each test for this sample was determined as 2, 2, 3, and 1, for static yield, dynamic yield, plastic viscosity, and slump, respectively. Therefore, the average workability performance of this sample was ranked as 2.25 and then the overall workability is reported as good In Table 3.5.

Table 3.5. Workability of the mixtures.

Mixture ID	Static Yield (Pa)	Dynamic Yield (Pa)	Plastic Viscosity (Pa/sec)	Slump (mm)	Overall workability	Is it inside the Tarantula curve
In_17,17	797	415	11.8	140	Good	Yes
In_11,10	1077	378	8.3	190	Good	Yes
In_18,15	1397.8	471.1	17.75	190	Good	Yes
Limit_20,13	1868.58	498.93	18.97	140	Moderate	Yes
Limit_16,19	2265.4	546.4	23.3	127	Moderate	Yes
Out_22,10	2662.78	518.13	29.5	152	Poor	No
Out_14,22	2639.17	619	30	102	Unusable	No

Table 3.6. Workability performance scale for each test based on Cook [123].

Workability performance scale for each test	Static Yield (Pa)	Dynamic Yield (Pa)	Plastic Viscosity (Pa/sec)	Slump (mm)
Excellent (1)	<1000	<250	<10	25-51
Good (2)	1000-1500	250-500	10-15	76-101
Moderate (3)	1500-2000	500-1000	15-20	127-152
Poor (4)	>2000	>1000	>25	178-203
Unusable (5)	Too stiff	Too stiff	Too stiff	>229

Figure 3.8 shows some observations of the mixtures Out_22,10, Limit_20,13, and In_18,15. Segregation was observed in sample Out_22,10 which had has more than 20% aggregates retained on a single sieve. The other mixtures appeared to be more uniform and cohesive. This

observation of segregation is important and will be discussed in more detail later.

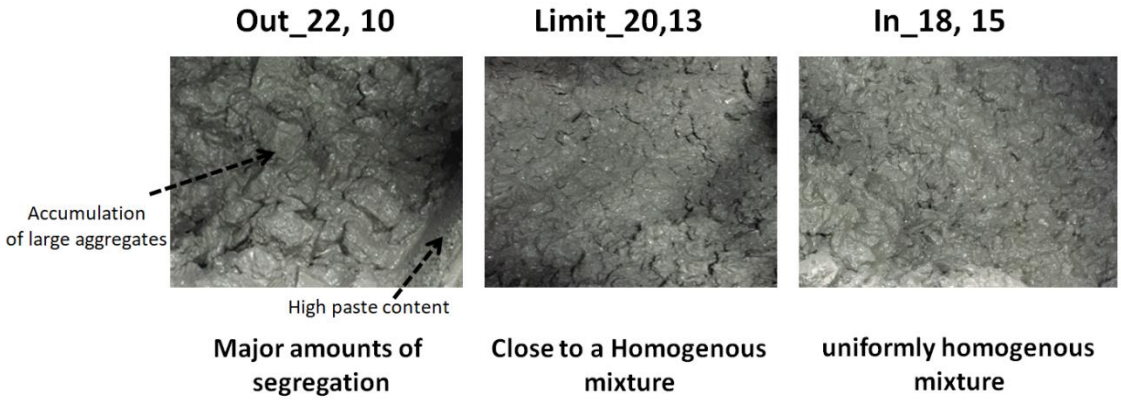

Fig. 3.8. An example of mixture homogeneity observed in the samples Out_22,10, Limit_20,13, and In_18,15.

3.3.2. Distance between aggregates

While the observations during mixing and the 3D rendering of concrete constituents provide important qualitative insights, it would be more helpful to quantify the aggregates distribution within the samples. Figures 3.9 and 3.11 demonstrate the nearest-neighbor distance between aggregates for different sizes grouped by their sieve size with both the distribution and cumulative percentage shown. Figure 3.9 investigates the nearest-neighbor distance between all investigated coarse aggregates (4.76 mm or larger). Figure 3.10 shows the aggregates larger than 9.75mm. Samples with the aggregate gradations inside, near, and outside of the Tarantula Curve are shown in green, yellow, and red, respectively. In addition, a second scan of the samples Out_22,10 and Out_14,22 is shown in orange. These scans were taken as repeat scans to see if similar trends were observed in other regions of the sample.

According to Figure 3.9, there is not a noticeable trend in the mixtures that are inside or outside of the suggested limits. However, when comparing the spacing of the aggregates that are 7.95 mm in diameter and larger (Figure 3.10), there is a difference in the observed performance. For

three of the four samples investigated with an aggregate content > 20% retained on a single sieve, there is a large percentage of aggregates with a spacing less than 600 μm. The cumulative percentage also provides important insights for these samples. About 75% of aggregates in these three have an aggregate distance smaller than 600 μm compared to the other samples in the cumulative percentage graph for aggregates retained on ≥ 9.75 mm sieve.

This close spacing of the aggregates can be explained from poor packing or congestion of aggregates in the mixture from adding too much of a single sieve size. These same mixtures were also observed to have poor or unusable workability. This suggests that this close spacing may be responsible for the decrease in workability of these mixtures.

A repeat scan of Out_22,10_2 also contains more than 20% retained on a sieve but it does not show the same performance. This sample also has about 50% of the volume investigated taken by a single large aggregate. Image of this are shown in Figure 3.11.

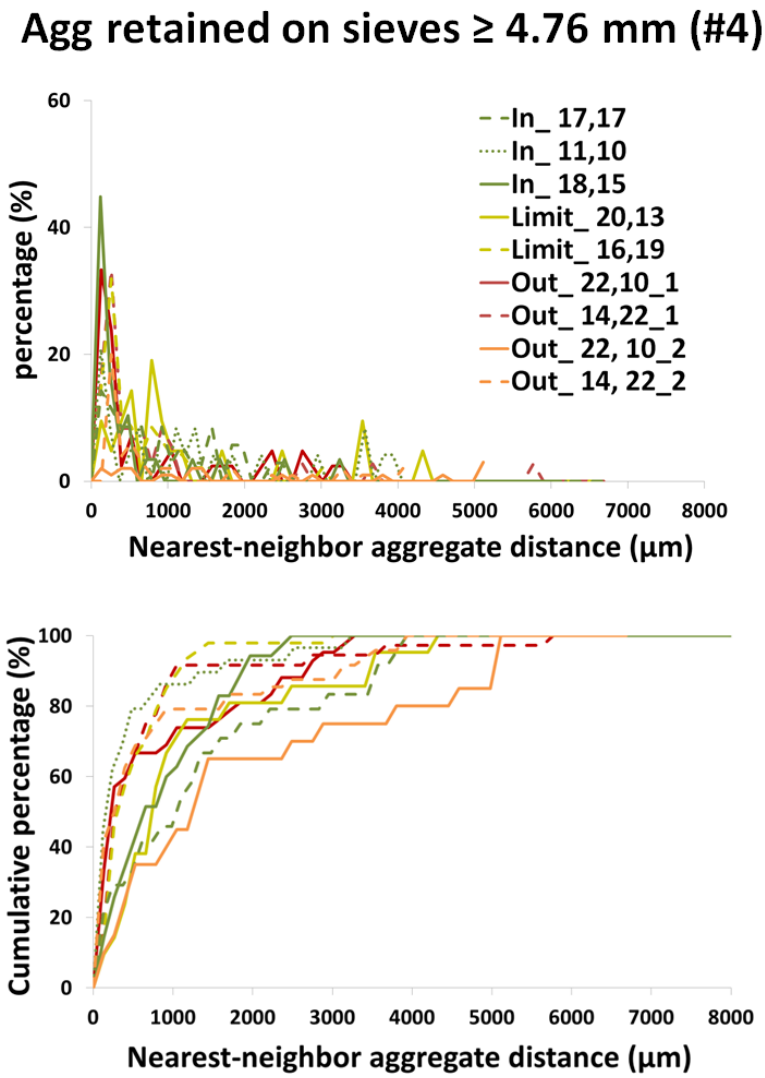

Fig. 3.9. Nearest-neighbor distance between aggregates retained on sieves ≥ 4.76 mm (#4).

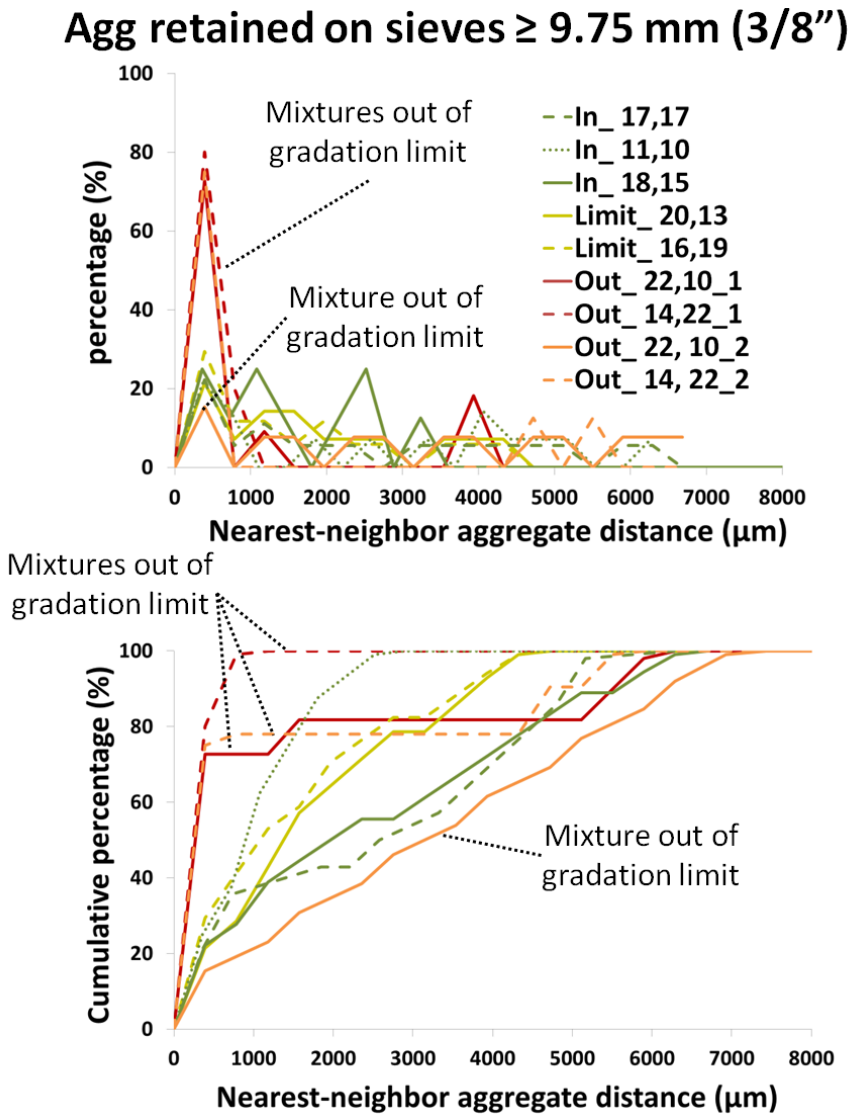

Fig. 3.10. Nearest-neighbor distance between aggregates retained on sieves ≥ 9.75mm (3/8″).

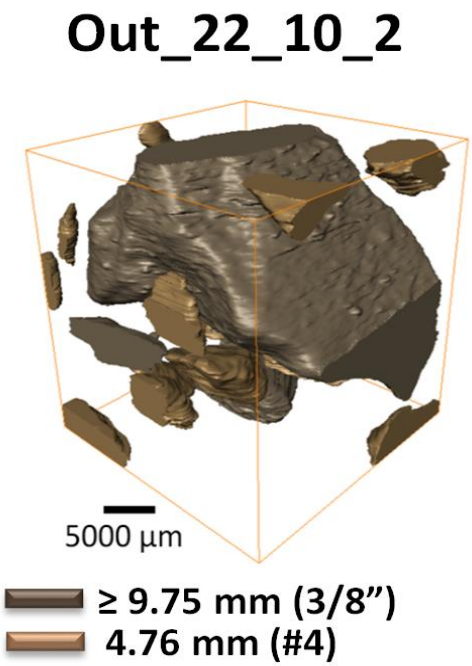

Fig. 3.11. 3D renderings of different aggregate sizes for the sample Out_22,10_2.

To provide further insights, the percentages of aggregates at different spacing for selected samples are shown with the corresponding 3D data sets in Figure 3.12. One sample within the limits (In_18,15) and two samples out of the limits (Out_22,10_1 and Out_14,22_1) are shown. In the graph, ≈ 80% of aggregates in the samples with the aggregate gradation outside of the Tarantula Curve are at distance closer than 1000 µm. The samples within or on the boarder have only ≈ 25% aggregate at this distance. The 3D renderings show that the aggregates cluster in certain regions of the sample. This means the aggregates are segregating. For example, the 3D renderings of the sample Out_14,22_1 show that the aggregates are clustered at the bottom. A similar trend was also observed for sample Out_22,10_1, but the aggregates are accumulated on the right of the 3D rendering. The sample In_18,15 seems to have a random aggregate distribution with no observable clustering. This is also supported by the quantitative analysis completed on the aggregate spacing as it also shows a uniform distribution of the aggregate

spacing and so this seems to explain the improved workability for the mixtures with < 20% retained on a specific sieve.

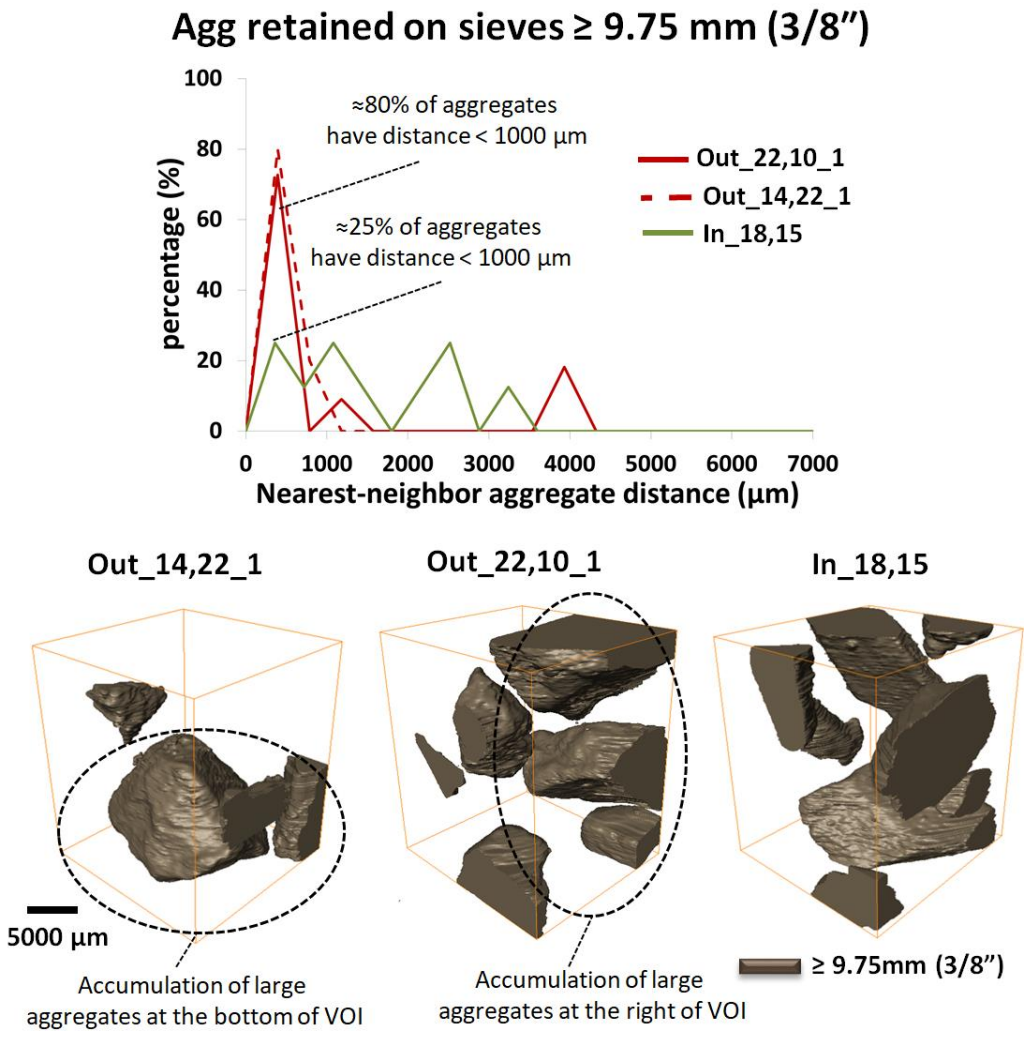

Fig. 3.12. 3D rendering and nearest-neighbor distance between aggregates for samples Out_22,10_1, Out_14,22_1, and In_18,15 in different sieve sizes.

3.3.3. Aggregate volume distribution at different cross sections

The previous analysis focused on aggregate spacing. This work focuses on quantifying the volume of aggregate at different locations. This analysis can determine the uniformity of the aggregate distribution. Figure 3.13 shows the volume of aggregates when investigated from three

different directions for samples Out_14,22_1, Out_14,22_2, Out_22,10_1, Out_22,10_2, and In_18,15. The volumes of aggregates at other cross sections are shown in the appendix A but these show similar results to In_18,15. For the samples investigated that were outside of the suggested 20% limit, there are locations where no aggregate is observed. For example, sample Out_14,22_1 has regions where no aggregate was observed on the cross section for the three directions investigated. Also, for sample Out_22,10_1, there was no aggregate observed in the bottom 7500 □m for the investigation along the Y axis. A similar observation was made for samples Out_14,22_2 and Out_22,10_2. A repeat scan of sample Out_14,22_2 has no aggregate in bottom and top 2000 µm along the Z and Y axis, respectively. In addition, for the sample Out_22,10_2, there was no aggregate observed in the distance of 2500 µm and 27,000 µm along the Y axis; however, as mentioned before, because of the existence of a large aggregate in the investigated VOI, the performance of this sample could be different from the other samples with aggregate gradation out of the recommended limits. This lack of aggregate means that there are locations with only mortar. This suggests that there is a non-uniform distribution of aggregates within these samples. However, for sample In_18,15 and the others shown in the Appendix A, every cross section investigated contained at least 10% aggregate and most contained at least 20% aggregate. This means that the aggregate is more uniformly distributed in these samples.

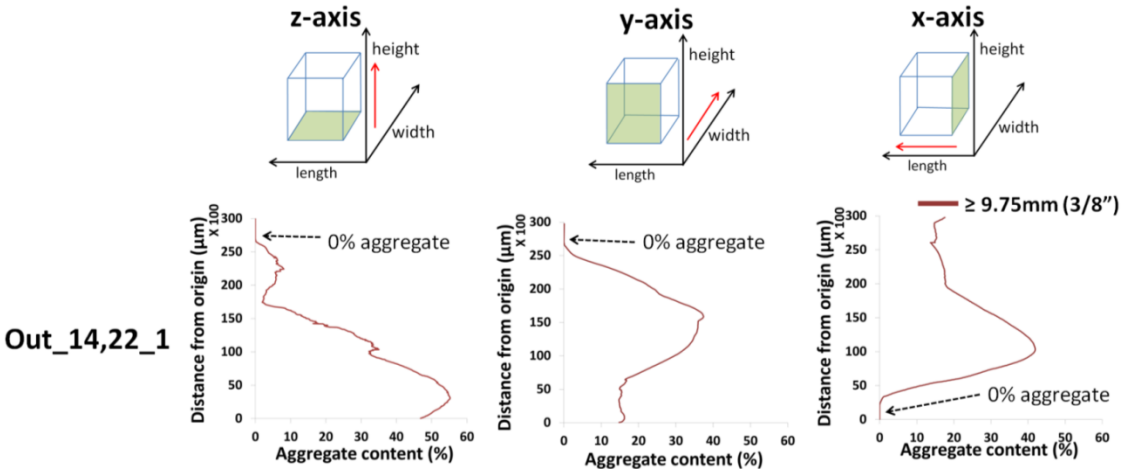

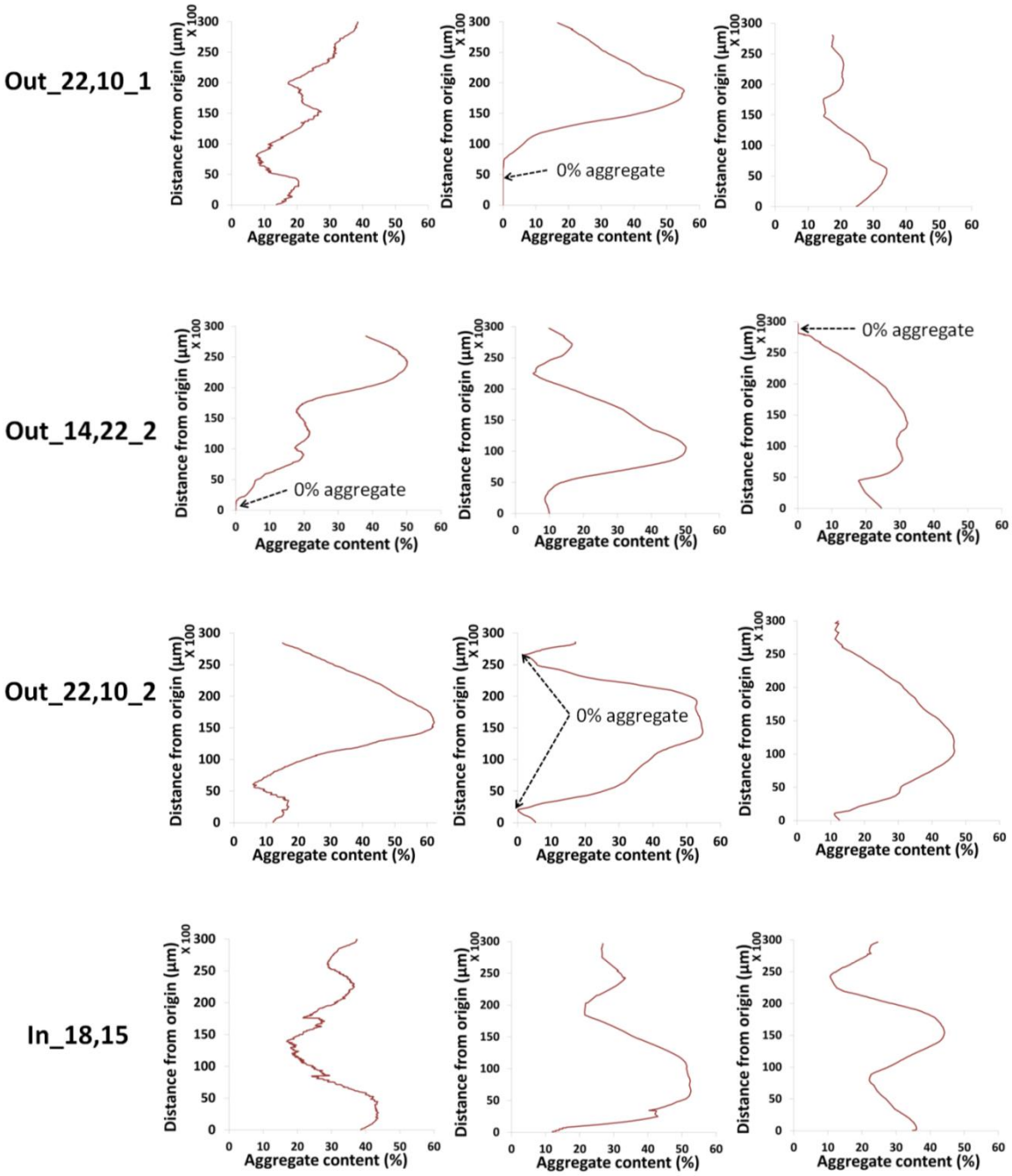

Fig. 3.13. Volume percentage of different aggregate sizes at different distances from the origin of VOI for samples Out_14,22_1, Out_22,10_1, Out,14_22_2, Out_22,10_2, and In_18_15.

3.4. Practical Significance

This study investigates the aggregate packing in hardened concrete for mixtures that are similar in volume, but with different aggregate gradations. The findings reinforce the importance of the aggregate gradation and the impact on the workability of the concrete. This work provides direct observation of low spacing between aggregates and non-uniform aggregate distribution that is occurring when the gradation is outside of the Tarantula Curve limits for the coarse aggregate. This means that when there is > 20% of a coarse aggregate retained then there will be segregation within the concrete and this will negatively impact the workability of the concrete. These findings also reinforce the previous work on the coarse aggregate limit of the Tarantula Curve and provide the mechanism for the loss in workability.

Furthermore, this work provides quantitative and qualitative data that can be used to better understand and model the packing of aggregate in hardened concrete and compare this information to the rheological parameters. This data could be an important step in developing computer models that provide more realistic prediction of performance within concrete. These results also provide important methods of comparisons for aggregate spacing and distribution that could be used in future work to investigate the mechanisms of aggregate size and spacing on the workability of concrete mixtures.

Understanding this information could allow concrete mixtures to be designed with an increased volume of aggregate and lower binder content. This would improve the cost, durability, and sustainability of these concrete mixtures while still creating a constructible concrete mixture. This would be a great benefit for the concrete industry.

3.5. Conclusions

XCT was used to study the packing of aggregates in the hardened concrete with a range of workability caused by different aggregate gradations. The following conclusions can be drawn from this work:

- When a mixture had < 20% retained on a given sieve size the mixture showed satisfactory workability, a uniform aggregate spacing, and all cross sections consisted of at least 10% aggregate.
- When a mixture had > 20% retained on a given sieve size the mixture showed poor workability, a spacing between aggregates of < 600 μm for more than 70% of the aggregates in the mixture, and cross sections were observed where no aggregate was present

These findings suggest that when > 20% is retained on a given sieve size then the coarse aggregate spacing is not uniform and there is observable segregation within the mixture. However, when the amount retained on a given sieve is < 20% then the aggregate distribution is more uniform.

These observations provide important insights into the cause of the decrease in workability with gradations outside of the coarse aggregate limits for the Tarantula Curve. This work also helps validate the Tarantula Curve. Furthermore, these observations highlight the importance of segregation on the workability of concrete and provide quantitative observations of this segregation within the hardened concrete.

These results show that XCT is a powerful non-destructive method that is useful for a better understanding and characterization of concrete mixtures. This work may be extended to a wider

range of problems where aggregate distribution or performance is important and this is an area of future research.

CHAPTER IV

USING X-RAY COMPUTED TOMOGRAPHY TO INVESTIGATE MORTAR SUBJECTED TO FREEZE-THAW CYCLES

Abstract

This work uses X-ray computed micro tomography (XCT) to investigate the role of critical degree of saturation (DOS) and air void system on the crack propagation of portland cement mortar subjected to freeze-thaw cycles. The method allows direct non-destructive 3D imaging at a spatial resolution of 4.85 μm/voxel before and after freezing. The results show that cracking occurred in non-air entrained mortar subjected to a single freeze-thaw cycle when the DOS was near 100%. These microcracks appear to initiate and primarily from the paste-aggregate interface or within aggregate. In addition, new products were observed to form within the pores after freezing. Most of the frost-induced microcracking and material-filled voids have been observed on the surface of the specimens. These observations provide insights into the freeze-thaw performance of mortar and are a step in understanding the damage in a concrete structure.

Keywords: Freeze-thaw cycle, Microcracking, X-ray Computed Tomography, Segmentation, Air void system.

4.1. Introduction

It has been suggested that frost-induced cracking can occur when concrete reached a critical level of saturation and then experiences freeze-thaw cycles [17, 124-129]. Samples with a saturation level greater than the critical degree of saturation (DOS) can result microcracking even with a single freeze-thaw cycle [125, 129]. This critical DOS is reported to be between 78% and 91% in different conditions [129, 130]. It has been widely shown in previous laboratory and field experiments that durability of concrete against frost-induced cracking can be improved by air entrainment [130-134]. The cracking has been proposed to initiate from weak parts of the microstructure like interfacial transition zone (ITZ) between the aggregates and the matrix but no direct observations have been made [135].

Although a great deal of efforts has been spent over the past decades toward understanding the freeze-thaw damage mechanisms, there are still several unanswered questions [17, 124, 126, 129-132, 136, 137]. Some of these include how ice forms in pores [126], how the air entrainments and air void size distribution affect the freeze-thaw damage [131, 132], how different parameters such as DOS, water absorption, and freezing rate affect freeze-thaw damage [124, 129, 130], and how microcracks initiate and propagate into the cementitious materials [19]. Because of this, direct observation of the microstructure before and after freeze-thaw cycles can give insights to address some of these questions.

Several techniques have been developed to investigate the microstructure damage caused by frost action. Recent publications have characterized microcracks in a cut mortar or concrete slices with optical microscopy or scanning electron microscopic (SEM) [138-141]. The major limitation of these techniques is that they can only make observations on the exposed surface. These observations may not necessarily be representative of the performance in the rest of the system.

In addition, they require preparation and testing condition that may disturb the sample and could affect the results.

X-ray computed tomography (XCT) is a powerful non-destructive tool that can be used to investigate the 3D microstructure of materials. It has been widely used in medical science to investigate biological organisms [9-11]. This method has also been used to study construction materials. Some examples include cement hydration [10, 12], aggregate spatial distribution [13-15], transport properties [16, 17], crack propagation [18-20], and air void distribution [21-23]. In this method, a series of 2D X-ray radiographs are captured from different viewing angles and the collected data sets are used to build a 3D measurement of the internal structure called a tomograph. The tomograph can be then used for qualitative and quantitative analyses [24-27]. Because of the non-destructive nature of XCT, multiple scans can be acquired from the same sample under different conditions. This allows samples to be investigated both before and after an event like freezing.

Some recent publications have used XCT to investigate microstructural changes in concrete or mortar exposed to freeze-thaw damage [142-144]. A previous work investigated the internal structure of fly ash and portland cement mortars with different air contents exposed to frost action by using XCT [142]. The work found that 50% of the air voids had sizes smaller than 50μm irrespective of the type of mortar. In addition, it was observed that significant cracking occurred in non-air-entrained samples with path tortuosity 1.5 smaller in z direction compared to the x and y direction, which indicates anisotropic microcracking in 3D. Another work studied the evaluation of porosity of mortar made with mixing proportions of 1:0:3, 1:1:6 and 1:2:9 (cement: lime: sand) by volume. The work found that mortar with a higher concentration of lime has a higher porosity which leads to more durability issue [145]. There are also some publications that measured entrained air-void parameters of concrete using XCT [105, 110, 146, 147]. Although these references suggest the importance of air void system on durability of cementitious materials

exposed to freeze-thaw action, they did not focus on crack initiation and critical degree of saturation as a key factor in the freeze-thaw durability of mortars. In another work, a combination of XCT and Acoustic emission (AE) experiments were used to investigate the volume and behavior of cracks in the mortars with different DOS subjected to the freeze-thaw cycles. It was found that the volume of microcracking decreases with decreased DOS up to the critical DOS, and there was no significant crack volume observed in the sample with DOS below the critical DOS. In addition, cracks were observed to form in both aggregates and ITZ in the samples with the DOS above the critical DOS. However, this work did not investigate the impact of the air void system in the frost damage of the mortar [148].

In this paper, XCT is used to investigate the 3D microstructure of mortar samples both before and after a single freeze-thaw cycle. The changes in microstructure, particularly air void system, and microcrack development are evaluated for samples with different DOS and air content.

4.2-Materials and Methods

4.2.1. Materials, sample preparation, and testing condition

One non-air-entrained (nAE) and one air-entrained (AE) mortar mixtures were prepared in accordance with ASTM C192/C192M-13 using the mixture proportions as reported in Table 4.1. In this table, the air content of the samples was determined in accordance with ASTM C185. All mixtures were made with ASTM C618 Type I ordinary portland cement (hereafter termed OPC) and constant water to cement ratio (w/c) of 0.42. The chemical composition and physical properties of OPC are shown in Table 4.2.

Table 4.1. Mixture proportion used in freeze-thaw experiments.

Mixture ID	air content (% by volume of mortar)	Type I cement, kg/m^3 (lb/yd^3)	Water, kg/m^3 (lb/yd^3)	Sand, kg/m^3 (lb/yd^3)
nAE	5	573.3 (966.3)	240.8 (405.9)	1333.3 (2247.4)
AE	9	548.9 (925.2)	230.6 (388.7)	1276.5 (2151.6)

Table 4.2. Chemical and physical properties of OPC.

Material	Blaine fineness (cm^2/g)	Density (gr/cm^3)	Chemical Composition (mass %)						Phase concentration (%)			
			SiO_2	CaO	Al_2O_3	MgO	Fe_2O_3	SO_3	C_3S	C_2S	C_3A	C_4AF
Type I ordinary portland cement	3680	3.15	19.3	64.0	5.2	2.6	2.9	3.3	63.4	8.4	9	8.7

The mortar samples were cast in prism molds with nominal dimensions of 25 × 25 × 125 mm (0.98 × 0.98 × 4.92 in.). A small core 1 cm (0.39 in.) in diameter and 1 cm (0.39 in.) in height was then drilled from the specimens and used for experiments.

The samples were scanned and then conditioned to different DOS before freeze-thaw cycles. For this purpose, all samples were oven dried in steps to 105°C for 2 days. The samples were placed in a desiccator and evacuated to a pressure of 30 mm Hg for 3 h. Following evacuation while still under vacuum, the samples were submerged by deionized water for 24 h. This condition was defined as 100% DOS. Some samples were also subjected to DOS between 85% and 95% by saturating specimens and allowing them drying in short periods of time at 23 °C ±1 °C and 50% relative humidity (RH). When each sample was conditioned to the desired moisture content (mass), they were re-weighed and wrapped with aluminum tape to ensure no moisture loss. The tape was left in place for the remainder of the testing. The DOS and the air content for each specimen are listed in Table 4.3. In Table 4.3, the first number and the second number in the specimen ID shows if it was air entrained (AE or nAE) and the DOS, respectively. As an

example, nAE_100 is an air-entrained mortar sample with 100% DOS. There were two repeats for nAE_93 and these samples are distinguished by adding a number to the end of their name.

The samples were first scanned with XCT and then subjected to a single freeze-thaw cycle that lasted 43.5 h. The temperature was reduced and then raised from 23 °C to −35 °C with a cooling rate of 2 °C/h and a heating rate of 4 °C/h. The samples were then scanned after the freeze-thaw cycle.

Table 4.3. The list of investigated samples.

Specimen ID	Degree of saturation (%)	Air content of mortar (%)
nAE_100	100	5
nAE_93_1	93	5
nAE_93_2	93	5
AE_95	95	9
AE_85	85	9

4.2.2. X-ray computed tomography

Each sample was scanned before and after exposure to a freeze-thaw cycle by a ZEISS XRADIA 410 with photon energy of 100 keV at a resolution of 4.85 μm/voxel. The captured volume of the interest was a cylinder 4.85 mm in diameter and 4.85 mm in height located near the surface of the sample as shown in Figure 4.1. The scan settings are summarized in Table 4.4.

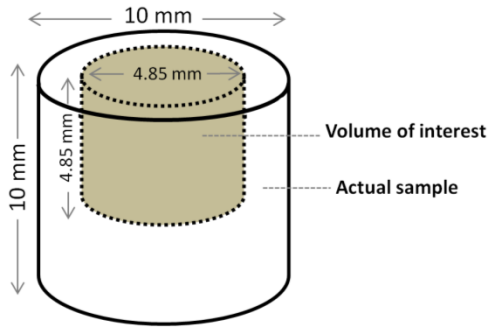

Fig. 4.1. Location and dimension of the investigated volume of interest (VOI).

Table 4.4. X-ray scan setting.

Resolution	4.85 μm/pixel
Source energy	100 keV
Optical magnification	4X
Total scan time	4 h
Number of projections	2800
Exposure time	3 s

The reconstruction was performed by XMReconstructor to create a stack of 2D slices. An example of the dataset is shown in Figure 4.2. Figure 4.2 shows the 3D representation of the sample, a typical cross section, and a histogram of the gray value in the 3D data set. Each 8-bit 2D image consists of pixels with gray values ranging from 0 to 255 corresponding to X-ray absorption which is a function of density and composition of the material [28, 29]. The gray value contrast can be used to separate the sample into different constituent phases by image segmentation process [15, 19, 21].

The major mortar constituents are air voids, aggregates, and OPC paste. Since the air voids have the lowest density, their X-ray absorption is the lowest among other constituents and so they are highlighted as dark voxels in the reconstructed images. Conversely, aggregates absorb more x-ray because of their higher density and appear as the brightest voxels in the reconstructed image. The paste has a gray value between these two constituents (Figure 4.2).

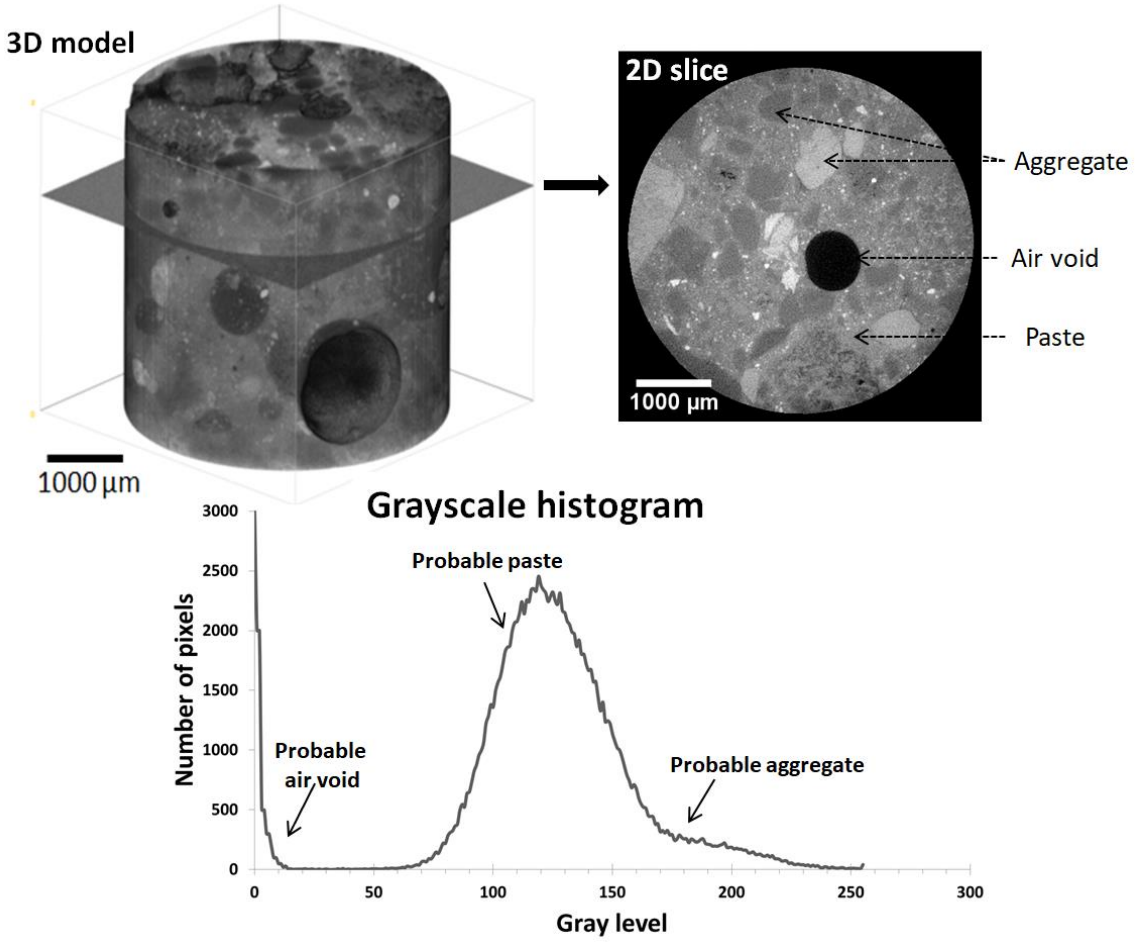

Fig. 4.2. A typical XCT dataset showing 3D tomography, 2D cross section of the reconstructed image, and corresponding grayscale histogram.

4.2.3. Image processing and analysis

In this study, different image processing techniques were used to provide quantitative and qualitative data sets for identification and comparison of the damage created by a single freeze-thaw cycle. Among various image processing, alignment, subtraction, and segmentation of the reconstructed images are the most important. The data sets before and after the freeze-thaw cycles were aligned. Image subtraction and segmentation were then performed to investigate the freeze-thaw damage and identify the mortar constituents or cracks before and after a freeze-thaw cycle.

4.2.3.1. Alignment of XCT datasets

All image processing, analysis, and 3D visualizations were performed by MATLAB codes, ImageJ, and Amira 4.1.1 software. There were two XCT datasets from the same specimen, one before and one after exposure to the freeze-thaw cycle. In order to reduce the computational time, all of the reconstructed datasets were first transformed from 16-bit image (65,536 gray levels) to 8 bit (256 gray levels) image. To make the datasets comparable, the histogram of the tomograph taken after the freeze-thaw cycle was shifted to match the histogram of the first tomograph. Subsequently, a self-authored computer code was used to align the XCT datasets before and after the freeze-thaw cycles. The program uses the first dataset as a reference to find the matching plane in the second 3D tomography dataset. Details of the technique can be found in other publications [19, 149, 150]. Figure 4.3 shows two matched slices before and after freeze-thaw cycles.

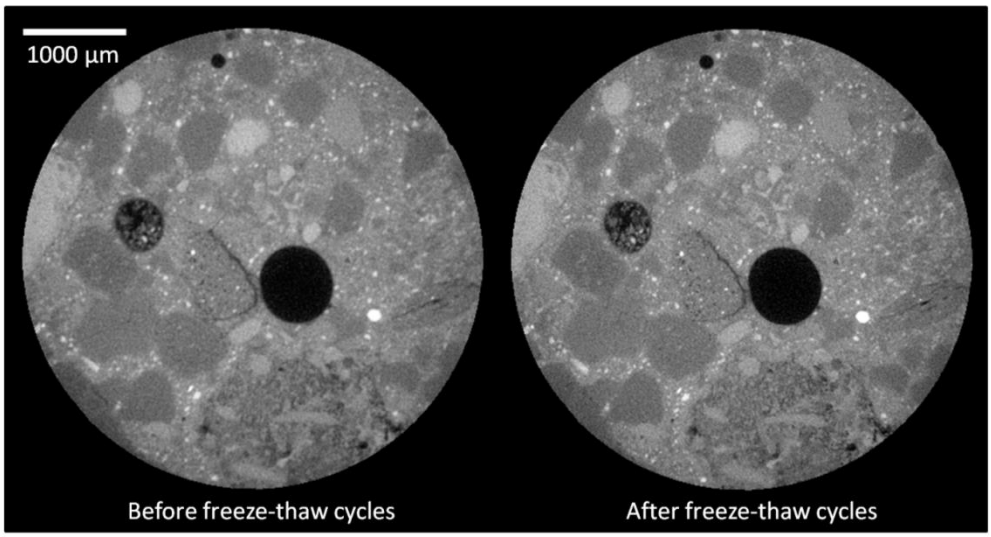

Fig. 4.3. An example of the results of matching algorithm for the reconstructed Images before and after freeze-thaw cycle.

4.2.3.2. Image subtraction

Image subtraction is a well-established image processing technique that has been previously used to study microcracks in mortar [20, 27]. This technique uses gray value differences to detect changes between two images. The image subtraction can be mathematically defined as the difference between the digital numerical value of the reference and second image [19]:

$$r(X) = f(X) - [a \cdot g(\varphi\ (X)) + b]$$

Where $r(X)$ is image subtraction, $g(\varphi\ (X))$ is gray level in the second image, a and b are coefficient of overall contrast and coefficient of brightness respectively. $f(X)$ is the gray level in the reference image which could be defined as either the image before or after the freeze-thaw cycle. A 3D median filter with a radius of 1 pixel was applied to remove noise from the subtracted image. In order to remove artifacts around the sample, image boundaries were established for both images. Figure 4.4 shows an example of image subtraction results for sample nAE_100. According to this figure, subtraction of the after datasets, which is used as the reference image, from the before datasets indicates cracks created by absence of materials in the image taken after freeze-thaw cycle; and the subtraction of the before datasets from the after datasets demonstrates probable new materials formed after freeze-thaw procedure which did not exist in the past.

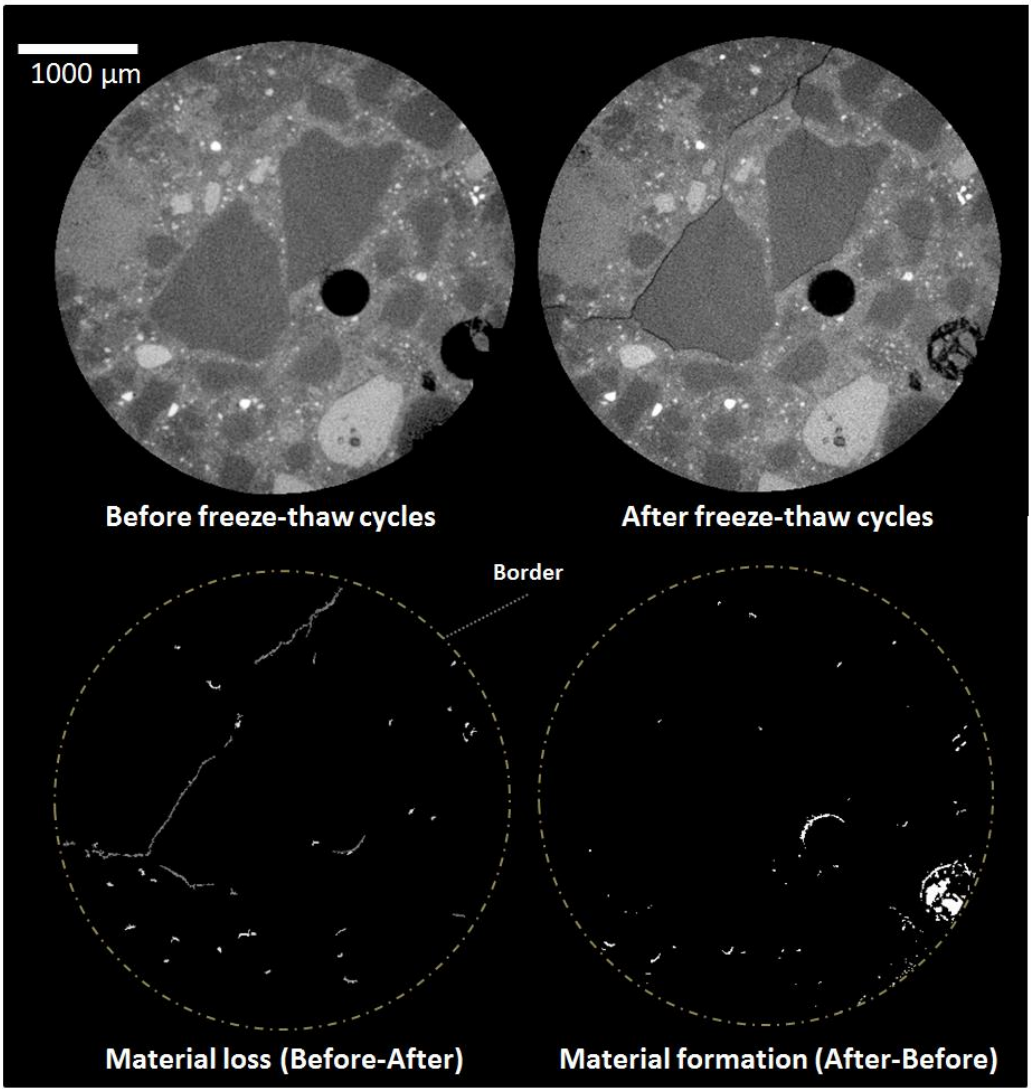

Fig. 4.4. 2D cross section of sample nAE_100 before and after freeze-thaw cycle, and subtracted images from each other.

4.2.3.3. Segmentation

Segmentation of XCT datasets is an important step in the quantitative analysis of the sample. In this study, two different methods of segmentation are used and then the results are combined. First, the cracks and air voids will be found and then the aggregate and paste will be identified.

4.2.3.3.1 Segmentation of cracks and air voids

In order to segment the cracks and air voids, an Otsu thresholding technique was used. Figure 4.5 shows an overview of the procedure for segmenting cracks and air voids. A median filter with a radius of 1 pixel was first used to reduce noise in the image yet preserve the edges of the constituent [144, 151, 152]. The Otsu method was then used to segment all air voids and cracks from the rest of the mortar constituents. This method is a common and well-established segmentation method that minimizes the mean square errors between the original and binarized images. More detail can be found in other publications [153-155].

Next, a morphological analysis was used to distinguish air voids and cracks in the segmented image. All spherical-shaped voids are identified as air voids. These regions were then compared before and after freeze-thaw cycle to highlight the material that had filled the air voids. The material was identified because the regions within the voids had changed in gray value. After identifying the air voids the remaining material was assumed to be crack. These regions are shown in Figure 4.5.

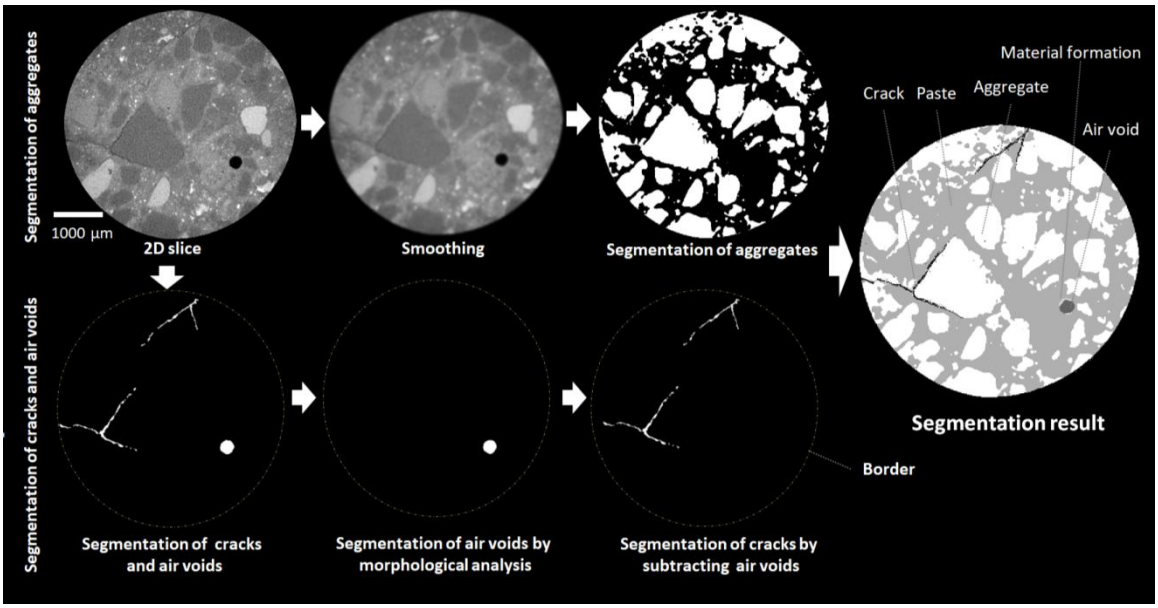

Fig. 4.5. Segmentation process of mortar constituent including air voids, cracks, materials formed within air voids, aggregates, and paste.

The segmented images were then used for further quantitative analyses such as material formation distribution and average air void distance.

To investigate material formation distribution at different distances from the bottom of VOI, the segmented air void images taken before freeze-thaw cycle were subtracted from the segmented air void images obtained after the free-thaw cycle. The result acquired from this subtraction indicates material formation which corresponds to those newly formation materials within the segmented air void images taken after a freeze-thaw cycle. The average distance between air voids was also determined by calculating the average nearest-neighbor distance between individual air voids. In this process, the average surface-to-surface nearest-neighbor distance between individual air voids was measured.

4.2.3.3.2 Segmentation of aggregate and paste

While the previous segmentation method is helpful to identify the cracks it is desirable to know whether these cracks form in the paste or within the aggregate. To learn more, the paste and aggregate had to be segmented.

Unfortunately, the Otsu method was not useful to segment aggregates since the gray values for the aggregate and paste overlap. This can be seen in Figure 4.2. In order to overcome this, a local sample inspection was used. Twenty different aggregate regions were identified by an operator. The average mean and standard deviation of the gray values were determined. Next, gray values that were two standard deviations away from the mean were used to find ranges of gray values that represent the particles. This region is shown in white in Figure 4.5. More information about gray value histogram and the normal distribution of aggregates can be found in the Appendix B. The remaining material was then assigned to be paste and is shown as gray in Figure 4.5.

Figure 4.6 shows the 3D rendering of the segmented XCT data of all samples before and after freeze-thaw cycles. The saturated sample (nAE_100) is shown in a larger size. The constituents are shown with different colors. The air voids are transparent. The paste is shown in gray. The aggregates are shown in brown. The cracks formed during the freeze-thaw cycle are shown in black and the materials formed within air voids after the freeze-thaw cycle are shown in orange.

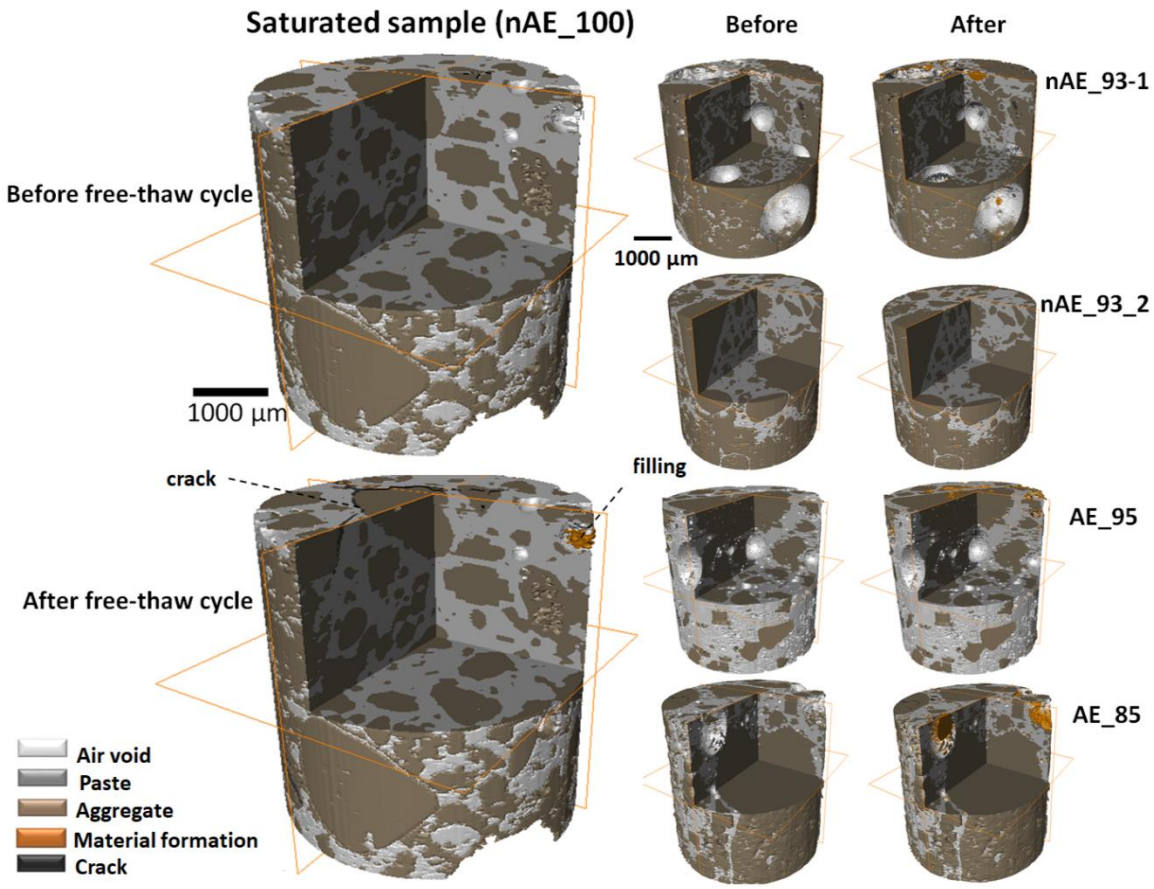

Fig. 4.6. 3D model of the segmented XCT data of all samples before and after the freeze-thaw cycle, an interior section is also shown for an easy 3D view.

These techniques were successful to segment the majority of aggregates and air voids. To investigate this, the measured aggregate volume is compared from the mixture design to the volume measured by XCT in Table 4.5. The XCT data estimates a fine aggregate volume of 53.1% and the mixture design suggests 55% by volume. This is less than a 4% difference. Differences could be caused by the limited sampling region analyzed by XCT (4.85 mm diameter × 4.85 mm in height). In addition, it is possible that there are aggregates smaller than the resolution of XCT that cannot be detected. There are also assumptions made in the image processing methods that may impact the results. It is also possible that the material varies within

the sample. Despite these differences, there was a small difference between the measured and expected values.

Table 4.5. Volume of aggregates calculated by XCT data and mixture design.

Sample No	Volume of aggregate (%) XCT data	Volume of aggregate (%) mixture design
nAE_100	56.8	55
nAE_93_1	52.0	
nAE_93_2	52.1	
AE_95	51.2	
AE_85	53.2	
Average	53.1	55

Figure 4.7 compares the air void content measured by XCT data and mixture design in the lab. According to the figure, except sample nAE_93_2, the air content calculated by XCT datasets for all samples was similar to the specified air content in mixture design. Air content measured by XCT data in sample nAE_93_2 was 1%, however, specified mixture design air content for this sample was 5% by volume of paste. It could be caused by the limited size of the volume of interest which is not necessarily represented of the entire sample. This difference will be discussed in more details later in the paper.

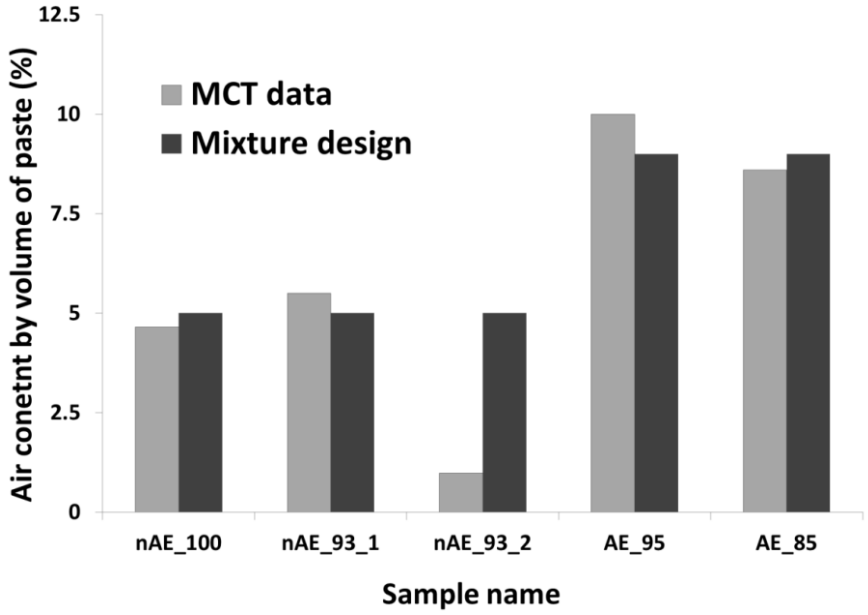

Fig. 4.7. Comparison of air content measured by XCT data and mixture design for all samples.

4.3. Results and Discussion

4.3.1. 3D analysis of initiation and propagation of cracks

While the investigation of the 3D structure provides important qualitative insights, it can also be used to produce quantitative insights such as the crack behavior by comparing the detailed 3D information both before and after the freeze-thaw cycle. Figure 4.8 shows the 3D rendering of the crack for sample nAE_100 both before and after a freeze-what cycle. The initial scans show that the sample had some cracks before it was exposed to the freeze-thaw cycles. The newly formed cracks are primarily observed near the top 20% surface of the sample (within ≈ 970 μm of the surface of the sample) after the freeze-thaw cycle. The presence of cracks at the interface of the paste matrix and aggregate may suggest that the interfacial transition zone (ITZ) may cause the development of cracks in sample nAE_100 as shown in Figure 4.6.

There was no crack propagation observed in the other samples. This could be caused by their lower DOS and the low number of freeze-thaw cycles. More information about crack propagation of other samples can be found in the Appendix B.

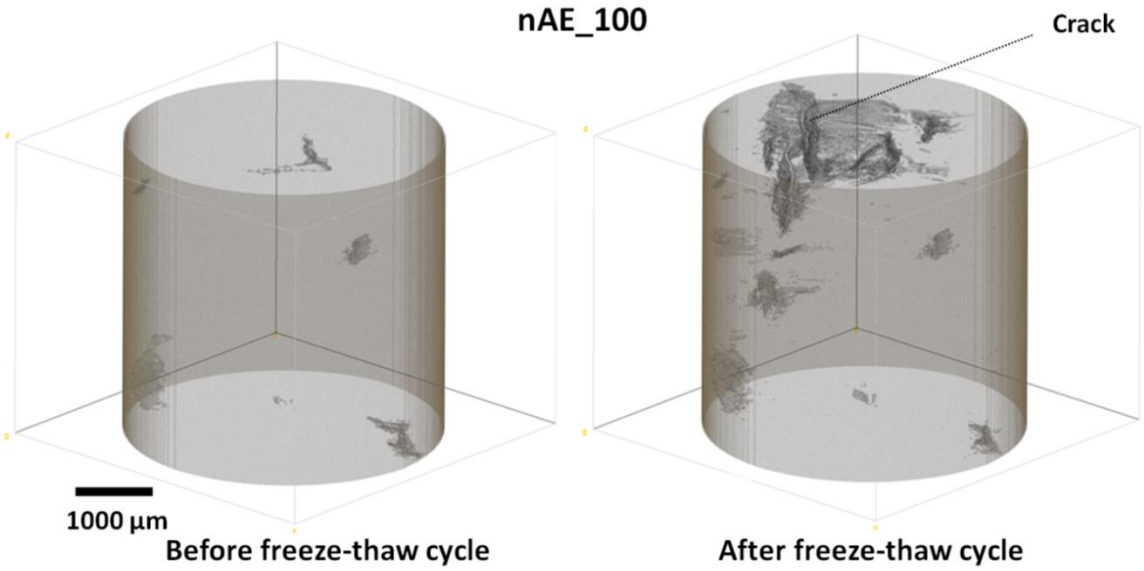

Fig. 4.8. An example of the 3D rendering of cracks for saturated sample both before and after freeze-thaw damage for nAE_100.

Figure 4.9 shows the volume of cracks that occurred in either paste or aggregate both before and after the freeze-thaw cycle. This bar chart shows that the crack volume within the aggregate increased by 4.5x and the cracks found within the paste increased by ≈ 13x. After the freeze-thaw cycle, the volume of cracks within the aggregates is ≈ 1.85x higher than the volume of cracks in the paste.

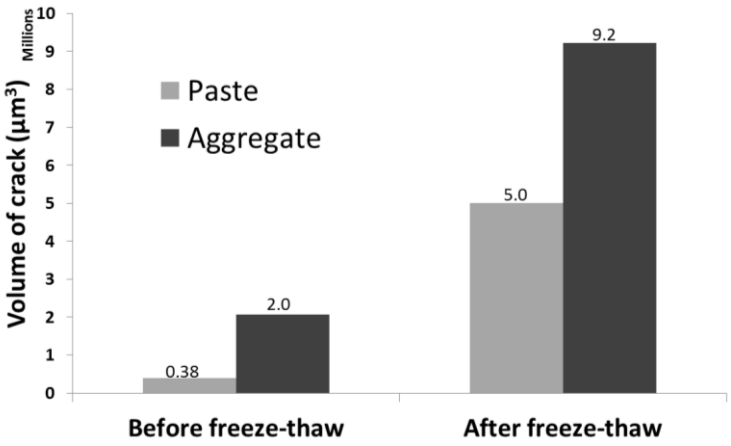

Fig. 4.9. Volume of cracks in the paste and aggregate before and after a single freeze-thaw cycle in nAE_100 sample.

Next, a detailed comparison is made in the cracking. The 3D rendering of cracks, 2D reconstructed images with highlighted cracks acquired from the top 20% of the saturated sample before and after are shown in Figure 4.10. This region was used because of the high density ofaa damage observed. According to the 2D reconstructed images shown in Figure 4.10. The images in the middle and right side of Figure 4.10 show a large volume of cracks forming within an aggregate.

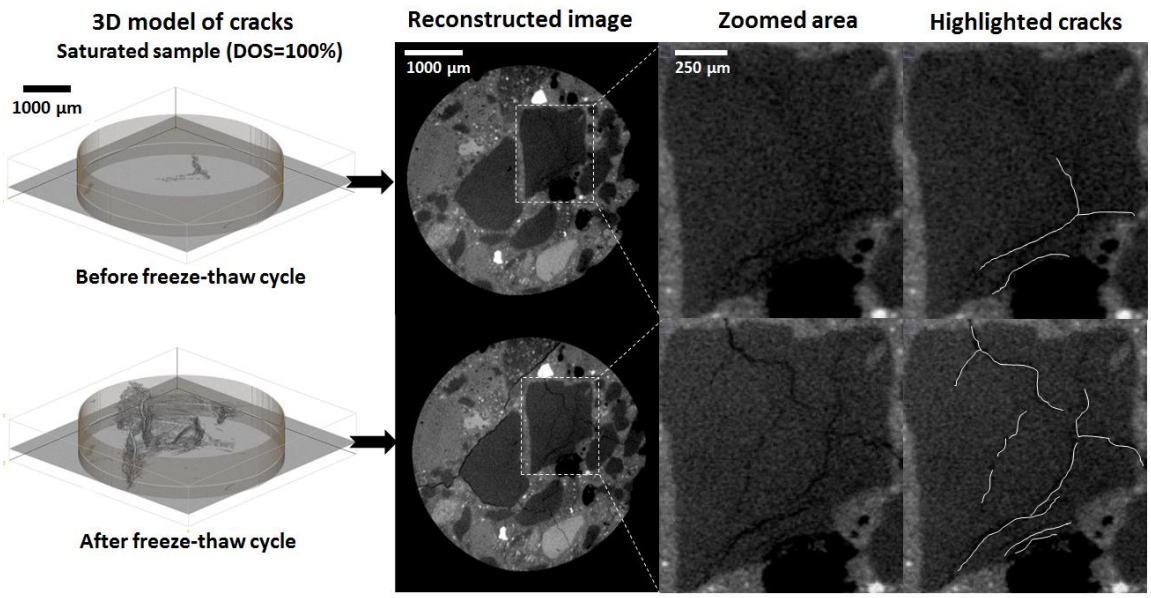

Fig. 4.10. An overview of initiation and propagation of cracks in the top 20% of the saturated sample (nAE_100) before and after the freeze-thaw cycle. Zoomed area is highlighted as white dash line in the reconstructed images.

Figure 4.11 shows the volume percentage of each component (air void, paste, and aggregate) at different distances from the measured cracks. The figure suggests that within the first 5 µm of a crack that 80% of the regions were aggregates, 20% paste, and 2% air voids. This suggests that the cracks are primarily formed close to aggregate surface. At ≈ 95 µm from the cracks, the aggregate volume is ≈ 50%. This closely matches the average volume for the entire sample as shown in Table 4.5. Another useful observation is that within 20 µm the volume of air voids observed is ≈ 1.3%. This is much lower than the average value of 5% that was observed in the sample in Figure 4.7. This again means that the cracks are not forming adjacent to air voids in samples with high levels of DOS and a single freeze-thaw cycle.

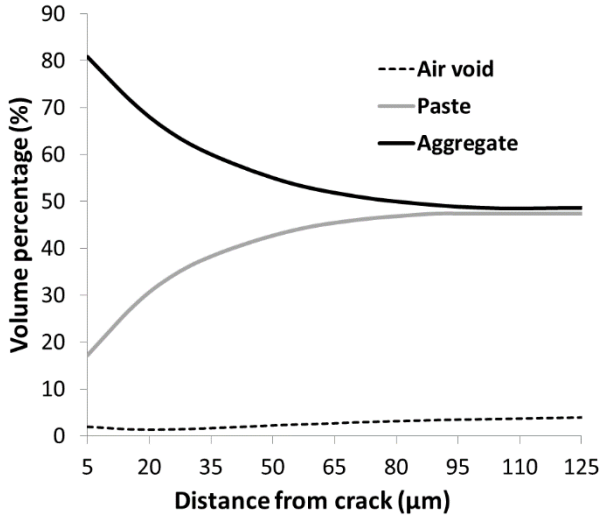

Fig. 4.11. Volume percentage of each mortar component (air void, paste, and aggregate) in different distances from cracks nAE_100.

4.3.2. 3D analysis of air voids after freeze-thaw damage

Figure 4.12 and Figure 4.13 show 3D renderings of the air voids, cracks, and infilled voids. The air voids are shown in white, cracks are highlighted in black, and infilled voids are shown in orange. Based on the 3D renderings, the infilled voids were observed in all samples. In addition, in all samples except nAE_93_2, between 65% and 80% of the infilled voids were located within ≈ 700 µm of the surface of the sample. When a void is observed to fill, this suggests that pore solution entered the void during the freezing cycle and that the concentration within the void was high enough to cause solids to precipitate. These solids are important as they can reduce the overall volume of the void and reduce the space available for future freeze-thaw cycles.

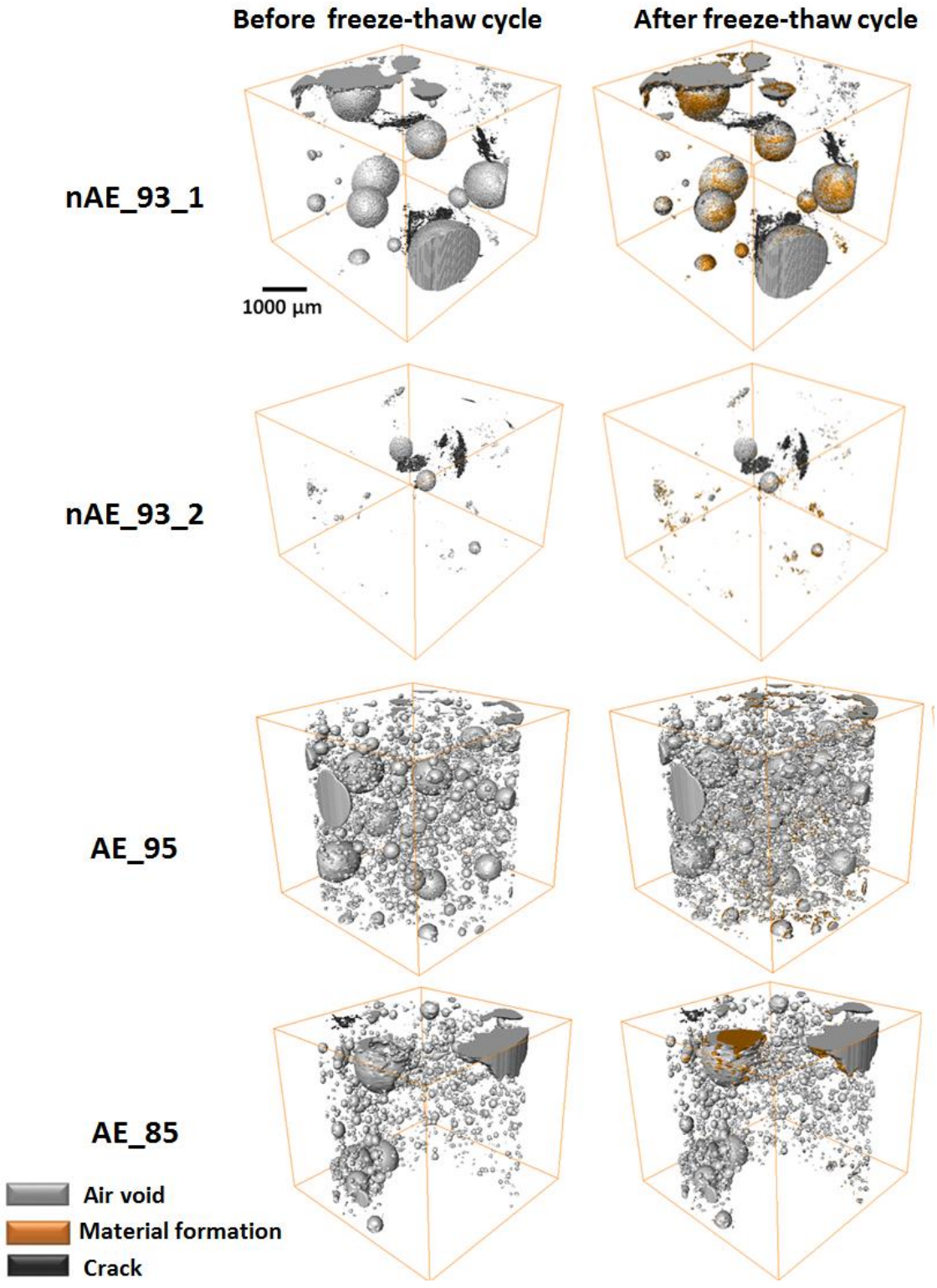

Fig. 4.12. 3D rendering of the air voids, cracks, and infilled voids for samples with DOS lower than 100% before and after freeze-thaw testing.

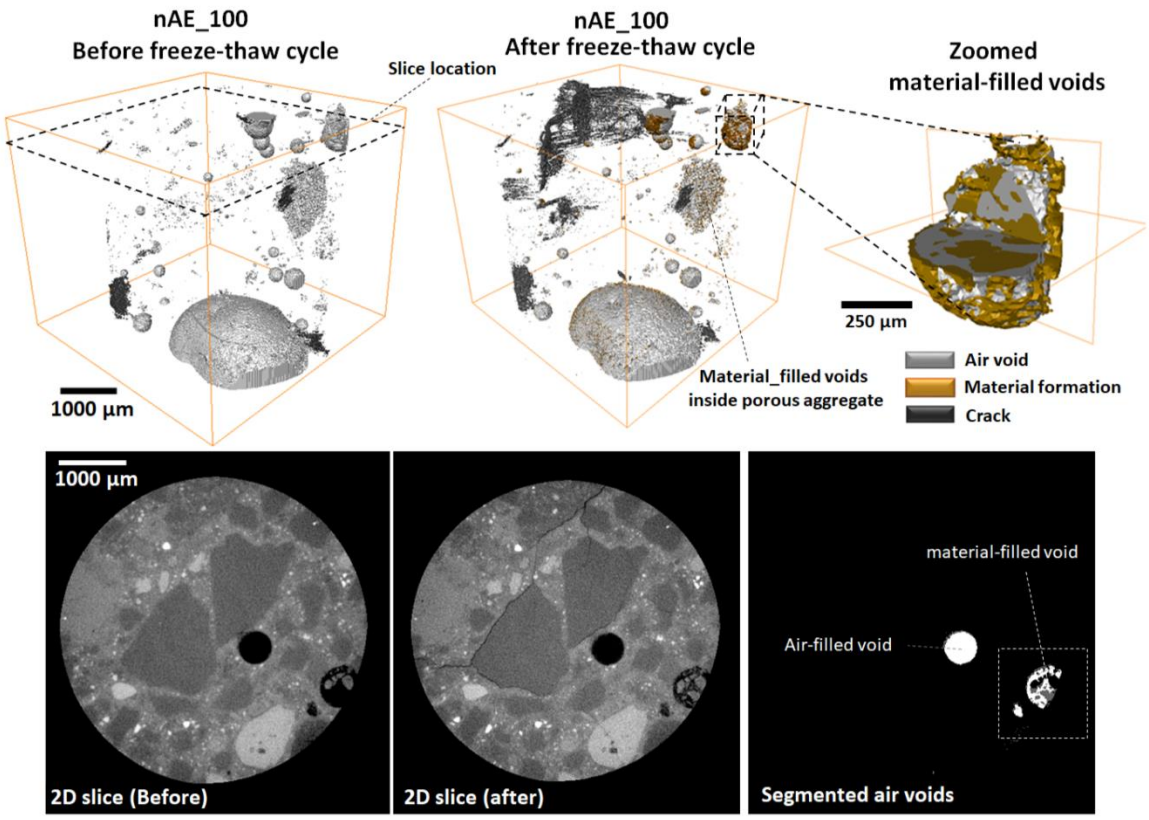

Fig. 4.13. An example of a 3D rendering of the air voids, cracks, and infilled voids for the saturated sample (DOS=100%) before and after freeze-thaw testing.

4.3.3. Quantitative evaluation of air void filling

In order to determine the distribution of the material-filled voids, the percentage of voids that at least 20% of their volume has been reduced from the material-filling is shown in Figure 4.14. This volume was chosen as it was large enough that the volume change was measurable and not a possible artifact. The number of individual air voids used in these calculations is about 500 and 30,000 for each non-air-entrained and air-entrained sample, respectively. The number of air voids in air-entrained samples was about 60x greater than the number of air voids in non-air-entrained samples. Figure 4.14 shows that partial infilling of at least 20% of an air void happened in the majority of voids smaller than 50 µm in diameter for both non-air-entrained and air-entrained samples. The saturated sample (nAE_100) had the lowest infilling percentage at different size

ranges compared to the rest of the samples. This could be because this sample and its pore system were damaged by the freezing-thaw cycle. This damage may not have let the pore solution to enter the voids.

Both samples nAE_93_1 and nAE_93_2 are thought to be similar in air volume, mixture proportions, and degree of saturation; however, nAE_93_2 shows a higher percentage of infilling for the voids larger than 50 µm. While the voids larger than 50 µm show differences, the voids smaller than 50 µm showed very similar behavior. It is not clear what causes these differences and this should be investigated further. Figure 4.15 shows the air void size distribution for samples nAE_93_1 and nAE_93_2 and both have very similar void distribution. However, the graph shows that nAE_93_2 has a higher number of finer air voids and ≈ 1.5x higher number of detectable voids compared to nAE_93_1. This difference between the void sizes might explain the difference between the void volume of samples nAE_93_1 and nAE_93_2.

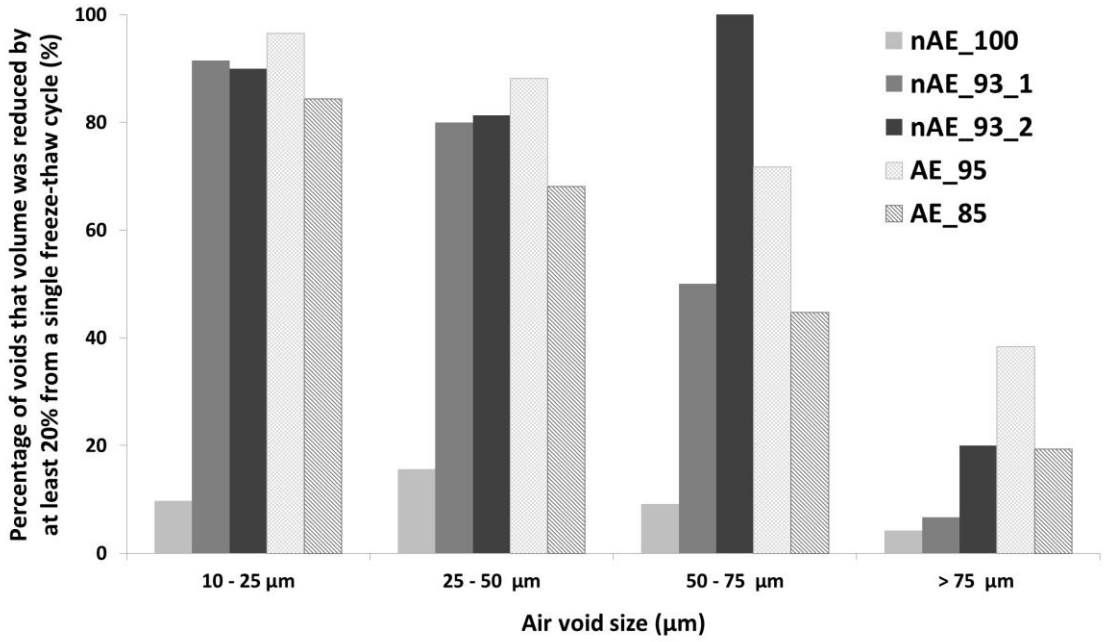

Fig. 4.14. Percentage of voids that volume was reduced by at least 20% from a single freeze-thaw cycle.

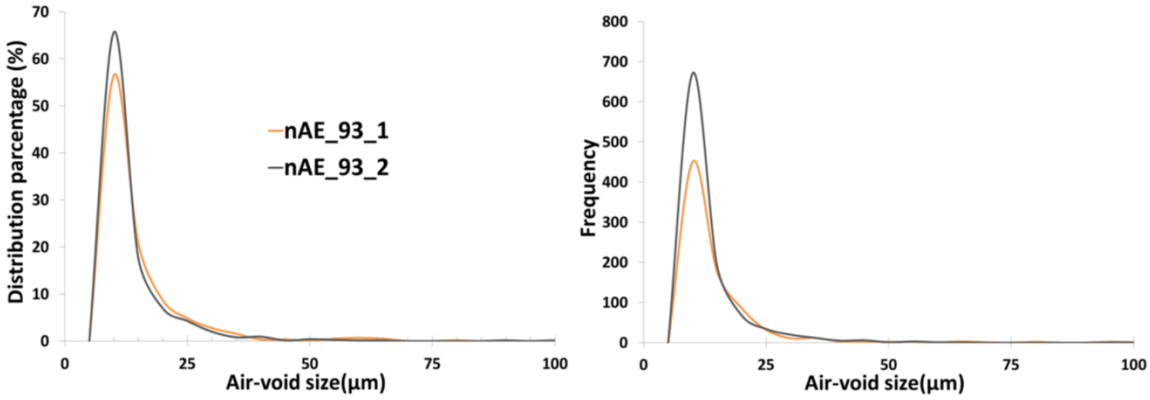

Fig. 4.15. Air void size distribution for sample nAE_93_1 and nAE_93_2.

The average infilled volume of partially filled voids is shown in Figure 4.16. Some examples of the calculation of this value for four individual voids with different sizes are also shown at the bottom of the graph with corresponding 3D renderings. As expected, the smallest group of air voids with a size between 10 and 25 µm has the highest average infilled volume compared to the larger voids. This higher value in the smaller voids can be attributed to the larger surface/volume of this group and that these voids probably contained more fluid during freezing than the larger voids. The sample nAE_100 again shows a lower amount of filled voids. This is probably due to the observed damage in this sample.

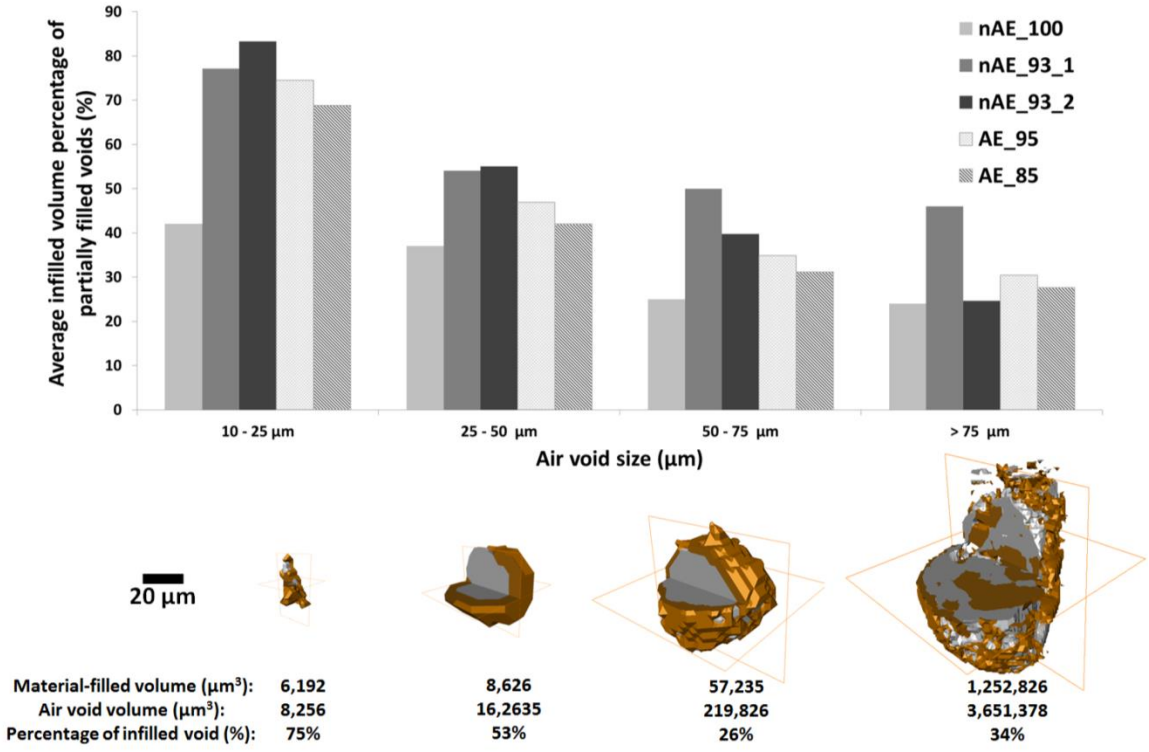

Fig. 4.16. The average infilled volume percentage in voids with at least 20% partial infilling. An example of a 3D rendering of individual partially material-filled voids for each size range with corresponded air void and material-filled volume, and infilled void percentage are also shown in the bottom of the graph.

Figure 4.17 shows the average nearest neighbor air void spacing calculated from XCT data. The average distance between air voids for air-entrained samples was about 17 µm; however, it varied from 25 µm to 44 µm for non-air-entrained samples. The variation of average air void distance for non-air-entrained samples can be observed in sample nAE_93_1 and nAE_93_2. These two samples have the same specified air content and degree of saturation, however, the average air void distance in sample nAE_93_1 is ≈ 1.7x higher than sample nAE_93_2. It suggests that the average spacing between air voids in air-entrained samples is lower and more consistent compared to non-air-entrained samples.

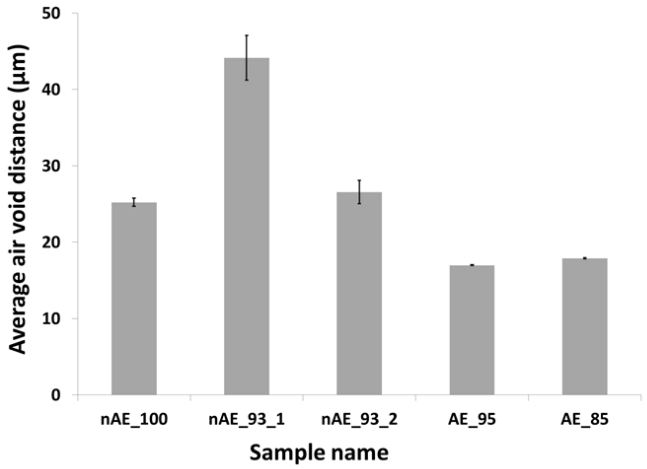

Fig. 4.17. The average air void distance calculated from XCT data for all samples.

Figure 4.18 shows the 3D rendering of material formation and the volume of material-filled voids at different cross sections. In all of the samples, except nAE_93_2, there is a higher volume of infilled material near the surface of the sample. For nAE_93_2 there was no significant change in the infilled air voids over the depth. This could be because of the low amount of air content (1%) detected by XCT in the investigated volume of interest compared to the expected mixture design air content (5%) which caused this sample did not have many air voids to fill.

When these samples were frozen the cold plate was at the bottom of the sample. Since the freezing plate is at the bottom this would mean that the top of the sample would be the last portion of the sample to freeze. The solution in the last region to freeze would be expected to have a higher concentration of dissolved ions and therefore would form a larger volume of precipitated solids within the air voids.

No analysis was done on the precipitated solids to investigate their chemical analysis. However, the material has a gray value that is similar to the hydrated cement paste. Based on previous publications this means this material is not likely to be pure calcium hydroxide; however, it could

be a mixture of calcium hydroxide and other precipitated salts such as Friedel's salt, Kuzel's salt, or salts originated from the aggregates [156-158].

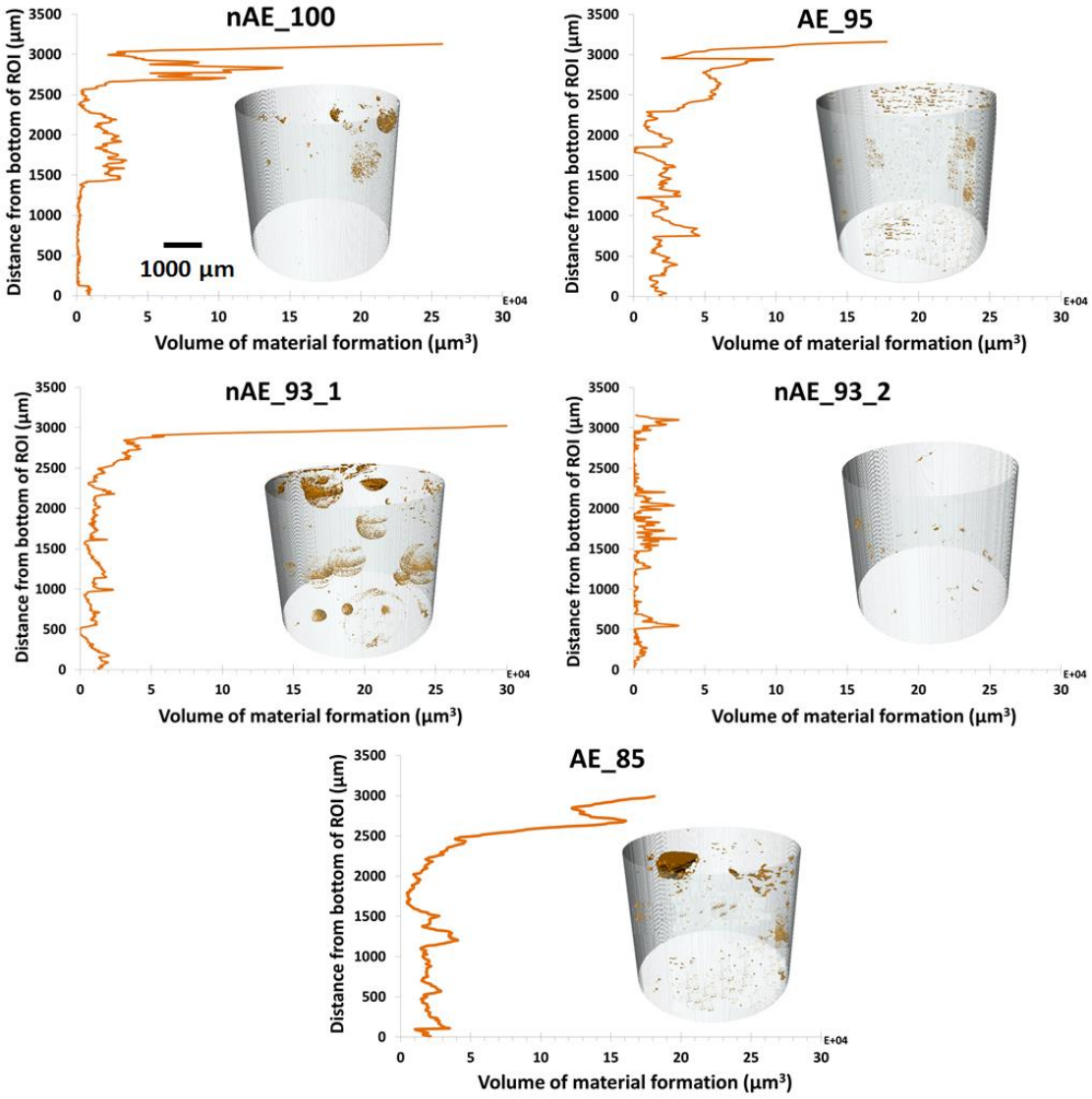

Fig. 4.18. Material formation at different image cross section and corresponding 3D rendering of material loss. The border of specimens in 3D rendering is shown as transparent gray.

4.4. Practical Significance

While much more work is needed to draw strong conclusions, this work has allowed some important insights into the mechanisms of freeze-thaw damage through direct observations by using XCT from before and after freezing events. Figure 4.6 shows that even with air entrained samples that at 100% DOS that damage can be observed in a single freeze-thaw cycle. Furthermore, Figure 4.11 shows that the cracks in this 100% DOS sample formed either in or near aggregates. However, Figure 4.6 shows that no damage was observed for the air entrained and non-air entrained samples, even with very DOS as high as 95%. It is expected that a higher number of freeze-thaw cycles are needed for observable damage in these samples.

Another significant observation is that the samples with DOS of 95% and lower all showed void filling after a single freeze-thaw cycle. The only sample that did not show void filling was the 100% DOS sample that was damaged. This difference in performance is attributed to this sample being damaged from the freezing events and so the fluid was not able to enter the voids. Figure 4.16 shows that the voids that were filled were primarily smaller than 20 μm and these voids were the furthest from the freezing surface. Furthermore, over 70% of the volumes of these voids are observed to fill from a single freeze-thaw cycle.

These small voids are arguably the most important for the freeze-thaw durability of the concrete as they provide a significant amount of protection for a given volume [125, 159]. If these voids are infilling with freeze-thaw cycles then that means they are not able to accommodate solution on freezing. While it is common for air void filling to be observed in freeze-thaw damaged concrete in the field, this work shows that samples with a DOS between 85% and 95% that this filling happens with very few cycles. This infilling of air voids could explain why rapid damage is observed in concretes when their DOS is high.

4.5. Conclusions

In this study mortar samples made with different air content and degree of saturation were examined with XCT to investigate microstructural changes caused by a single freeze-thaw cycle. The XCT method was a very powerful tool to observe the crack volume, void distribution, and void filling. Although all of the samples had DOS greater than 85%, the non-air entrained saturated sample with DOS ≈ 100% was the only sample where damage was observed. However, it is possible that cracks exist in the other samples that are below the resolution of the scans and so they would not be detected.

Findings for cracking:

- All samples had some initial cracks before the freeze-thaw cycle. Most of these cracks were observed within the aggregate.
- Crack initiation and propagation were primarily observed within ≈ 970 μm of the top surface of the sample with DOS ≈ 100% (nAE_100) after a single freeze-thaw cycle.
- A single freeze-thaw cycle caused an increase in the volume of crack within aggregate by 4.5x and an increase in the volume of crack within the paste by a factor of 13 compared to the volume of crack before freeze-thaw cycle.
- Most of the newly-formed cracks occur in aggregate after the freeze-thaw cycle.

Findings for void filling:

- All samples experienced air void filling mostly located within ≈ 700 μm of the top surface of the samples.
- The voids smaller than 20 μm in the samples with DOS between 85% and 95% showed more than 70% filling after a single freeze-thaw cycle.

- Sample nAE_100 showed the most damage and the lowest percentage of filled voids.
- The replicate samples with DOS of 93% showed very similar void filling for voids smaller than 75 μm.

Research is needed to investigate how the void size, volume, and spacing may impact the void filling observed in this work and how multiple freeze-thaw cycles will impact the results. Additional work to investigate the chemistry of the filling materials would also be useful. While limited cracking was observed in the samples, these results show that this procedure shows great promise to be used to investigate samples under higher numbers of freeze-thaw cycles.

CHAPTER V

INVESTIGATION OF CEMENT PASTE BEFORE AND AFTER FREEZE-THAW CYCLES WITH X-RAY IMAGING

Abstract

This work presents the usefulness of X-ray imaging techniques to investigate the role of air void system on the freeze-thaw damage of the cement paste. The method allows direct 2D and 3D non-destructive imaging at micron length scales. This work aims to present the method and show the usefulness in hopes of expanding this for future work. The 2D results show that severe frost damage occurred in the surface of the non-air entrained cement paste ponded with KI solution after 63 freeze-thaw cycles. It was observed from 3D analysis of the images that the average distance between air voids in the non-air-entrained was ≈ 1.8x higher than the average distance between air voids in the air-entrained samples. In addition, Most of the air voids (≈ 75%) in both non-air-entrained and air-entrained samples are distributed in size ranges between 15 to 60 μm. These observations show that X-ray imaging is a powerful method that provides new insights into the freeze-thaw performance of cement paste and is a step in understanding the damage in a concrete structure.

Keywords: Freeze-thaw cycle, Microcracking, X-ray Computed Tomography, Segmentation, Air void system.

5.1. Introduction

Frost damage of cementitious materials is one of the major concerns for field structures in cold climates. In many cold climates deicing salts are used to minimize the ice formation on concrete surfaces [160, 161]; however, these salts can react with cement hydration products and form new products such as brucite, complex salts, and oxychlorides [162]. These new products can penetrate and grow in the empty pores which reduce the volume of air voids and thereby, increase the degree of saturation and pressure of frozen water and accelerate concrete frost damage [162-164]. The frost damage of concrete in this condition is reported to be 4x to 5x higher in comparison to the concrete exposed to just water [160, 161].

It has been widely shown in previous laboratory and field experiments that durability of concrete against frost-induced microcracking can be improved by adding an air entrainment agent (AEA) during mixing [131-133]. Previous research has shown that uniform air void systems created by AEA with adequate spacing allows water movement during freezing from the capillary pores to the nearest air void where it can freeze and not cause damage [159]. According to the crystallization pressure theory, as the temperature decreases, it is easier for ice to form in the air-entrained void than it is in a capillary void [136]. It is suggested that the capillaries are like an interconnecting network of tubes with large and small capillaries distributed in concrete. When ice crystals form upon low enough temperatures, the large capillaries will fill with ice and try to enter the small capillaries. If the concrete mixture does not have AEA, the friction and tortuosity in the system will cause a back pressure and resulting in subsequent damage. If the sample is air entrained, then as ice forms within the air entrained voids then it will reduce the freezing water within the capillaries. This will reduce the stresses within the paste and reduce damage [136].

Although a great deal of efforts has been spent over the past decades toward understanding the freeze-thaw damage mechanisms, there are still several unanswered questions [17, 124, 126, 129-

132, 136, 137]. There are still debates among researchers on how ice forms in pores [126], how the air entrainments and air void size distribution affect the freeze-thaw damage [131, 132], how different parameters such as air content and temperature affect freeze-thaw damage [124, 129, 130], and how microcracks initiate and propagate into the cementitious materials [19]. Because of this, direct observation of the microstructure before and after freeze-thaw cycles can give insights to address some of these questions.

Several techniques have been developed to investigate the microstructure damage caused by frost actions. Recent publications have characterized microcracks in cut cementitious materials slices with optical microscopy or scanning electron microscopic (SEM) [138-141]. The major limitation of these techniques is that these techniques can only make observations on the exposed surface. These observations also may not necessarily be representative of the performance in the rest of the system. In addition, they require preparation and testing conditions that may disturb the sample and could affect the results.

X-ray computed tomography (XCT) is a powerful non-destructive tool that can be used to investigate the 3D microstructure of materials. It has been widely used in medical science to investigate biological organisms [9-11]. This method has also been used to study construction materials. Some examples include cement hydration [10, 12], aggregate spatial distribution [13-15], transport properties [16, 17], crack propagation [18-20], and air void distribution [21-23]. In this method, a series of 2D X-ray radiographs are captured from different viewing angles and the collected data sets are used to build a 3D measurement of the internal structure called a tomograph. The tomograph can be then used for qualitative and quantitative analyses [24-27]. Because of the non-destructive nature of XCT, multiple scans can be acquired from the same sample under different conditions. This allows samples to be investigated both before and after an event like freezing.

In this paper, X-ray imaging is used to investigate the 2D and 3D microstructure of paste samples with the different air contents before and after freeze-thaw cycles. The changes in microstructure, particularly air void system, and microcrack development are evaluated for samples with different air contents.

5.2. Materials and methods

5.2.1. Materials and sample preparation

One non-air-entrained (nAE) and two air-entrained (AE) paste mixtures with a constant water to cement ration (w/c) of 0.45 and different air contents (7.5 and 15% air by volume of paste) were prepared in accordance with ASTM C 305 using the mixture proportions reported in Table 5.1. The air content of the specimens was determined in accordance with ASTM C185. In this procedure, 121 g and 63 g of AEA were added during the mixing process to achieve the required unit weight for the mixtures with 7.5% and 15% of air, respectively. The cement is an ASTM C150, Type I. The chemical composition and physical properties of the cement are shown in Table 5.2.

Table 5.1. Mixture proportion used in the experiments.

Mixture ID	w/c ratio	Cement weight (g)	Water weight (g)	Air content (%)
nAE	0.45	1373.2	617	1.5
AE_7.5	0.45	1373.2	617	7.5
AE_15	0.45	1373.2	617	15

Table 5.2. Chemical composition and physical properties of cement.

Material	Chemical Composition (mass %)								Phase concentration (%)			
	SiO_2	CaO	Al_2O_3	MgO	Fe_2O_3	SO_3	K_2O	Na_2O	C_3S	C_2S	C_3A	C_4AF
Type I	21.1	62.1	4.7	2.4	2.6	3.2	0.3	0.2	56.7	17.8	8.16	7.8

Four specimens from each mixture were cast in cylindrical micro vials with interior dimensions of 9.5 × 46 mm (0.375 × 1.82 in.). The vials were partially filled with the mixture in order to provide 15 mm of free space for the solution above the paste samples. The specimens were then sealed with a lid and then taped and cured for 28 days at 23 °C.

Next, the samples were ponded by adding different solutions on top of the paste for 14 days at 23 °C inside the vials. Two specimens from each mixture were ponded with 0.6 mol/L potassium iodide (KI) solution and the rest of the specimens were ponded with water. KI is a salt with an electron dense cation which is a contrast agent or tracer for concrete fluid transport study [165-167]. It is also suggested that and iodide (I) in KI has a similar diffusion coefficient in cement paste as chloride (Cl) in sodium chloride (NaCl), which is a common salt used for deicing [168-170]. Therefore, as specimens are ponded with KI solution, the changes in the X-ray absorption or the gray value of materials in the cement paste can be monitored during X-ray imaging more conveniently compared to a cement paste ponded with water.

Radiographs were collected for each specimen before and after ponding to ensure the sample has not dried. The samples were then subjected to freeze-thaw cycles. The temperature was varied between 5°C to −39 °C with 3.5 h cooling at −39°C and 3.5 h heating at 5°C for three freeze-thaw cycles a day. Radiographs were then taken in thawing condition after 21, 42, and 63 freeze-thaw cycles (7, 14, and 21 days) to determine the level of freeze-thaw damage of the paste samples. The liquid solution was removed during the scanning; the vials were then filled with the solution after completion of the data collection and returned for additional freeze-thaw cycles. A

tomograph was also taken after 82 freeze-thaw cycles to better understand the 3D distribution of air voids and damages.

5.2.2. X-ray imaging

The radiographs were acquired by a Skyscan 1172 micro-CT scanner with a tube voltage and current of 100 keV and 100 µA at a spatial resolution of 8.76 µm/pixel. In addition, a 0.5 mm Al and 0.5 mm Cu filter was used to improve the quality of the scan. An example of the experimental setup is shown in Figure 5.1. In this figure, a special stage is used to minimize any probable shift during data collection over different time periods. In this figure, an Al wire of 0.6 mm thick was attached to the wall of each vial to aid in alignment and image processing.

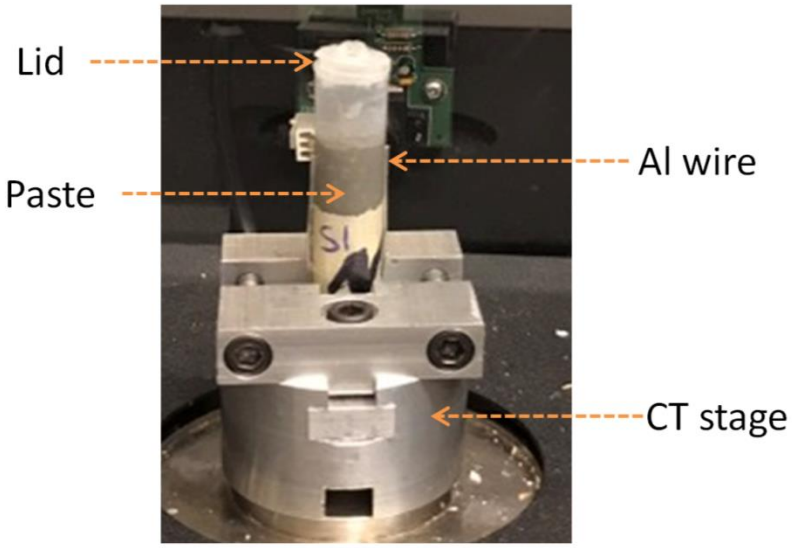

Fig. 5.1. An example of the experimental setup.

A tomograph of each sample after 82 freeze-thaw cycles (28 days) is collected by a ZEISS XRADIA 410 with photon energy of 100 keV at a resolution of 14.2 µm/voxel. The captured volume of interest (VOI) was a cylinder 9.5 mm in diameter and 12.8 mm in height located near the surface of the sample. The scan settings are summarized in Table 5.3.

Table 5.3. X-ray scan setting.

Resolution	14.2 μm/pixel
Source energy	100 keV
Optical magnification	0.4X
Total scan time	4 h
Number of projections	2800
Exposure time	3 s

The reconstruction was performed by XMReconstructor-10.7.3245 to create a stack of 2D slices. An example of the dataset is shown in Figure 5.2. This figure shows the 3D representation of the sample, a typical X-section, and a histogram of the gray value in the 3D data set. Each 8-bit 2D image consists of pixels with gray values ranging from 0 to 255 depending on X-ray absorption which is a function of density and composition of the material [71, 114]. The gray value contrast can be used to separate the sample into different constituent phases by image segmentation process [21, 108, 111].

The major detectable paste constituents are air voids and OPC paste. Since the air voids have the lowest density, their x-ray absorption and therefore gray value is the lowest in the reconstructed images. Conversely, the paste absorbs more X-ray because of its higher density and appears as the brightest voxels in the reconstructed image (Figure 5.2).

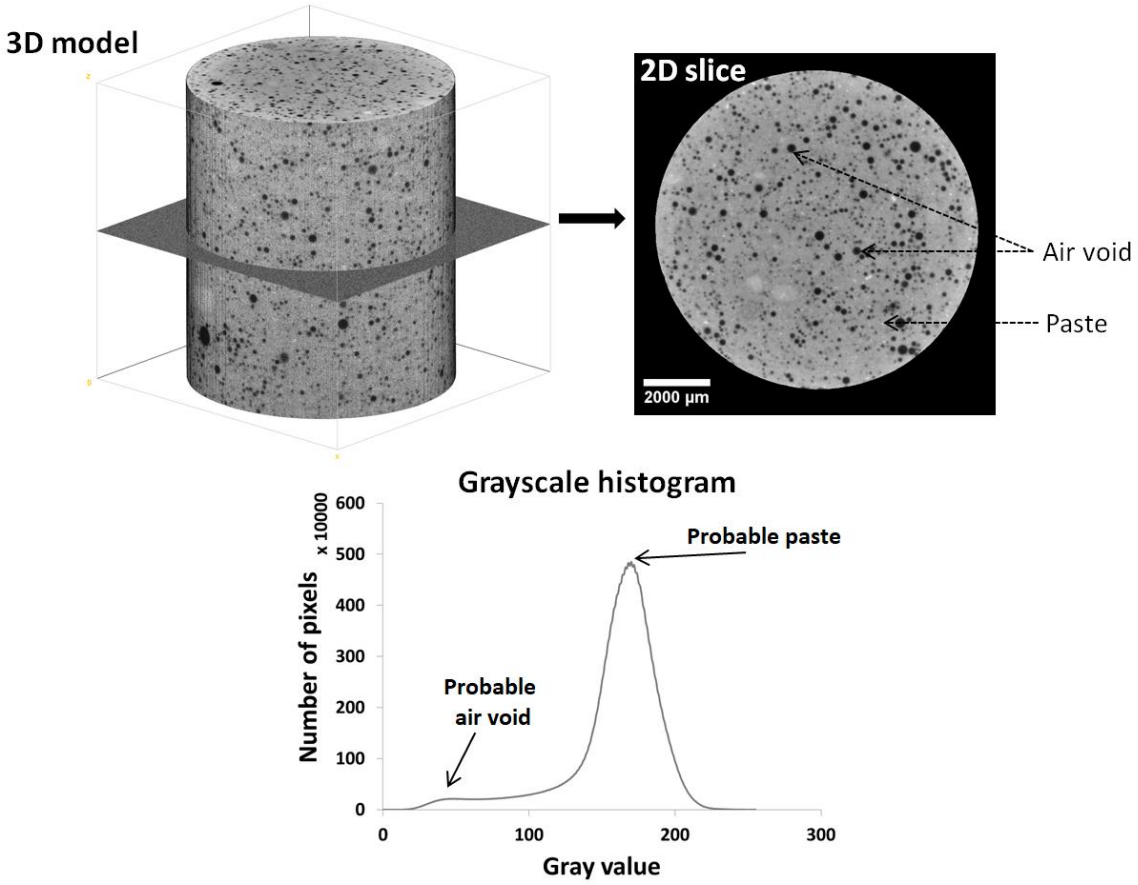

Fig. 5.2. A typical XCT dataset showing 3D tomography, 2D cross section of the reconstructed image, and corresponding grayscale histogram.

5.2.3. Image Processing

Different image processing techniques were used to provide quantitative and qualitative data sets for identification and comparison of the damage created by freeze-thaw cycles. The image processing and analyses applied on each radiograph and tomograph are discussed in the following sub-sections.

5.2.3.1. Alignment and image subtraction of radiographs

All image processing and analyses were performed by MATLAB codes and ImageJ software.

Radiographs were taken on the same specimen at different freeze-thaw cycles. A self-authored computer code was used to align the radiographs taken from each sample. The program uses the coordinates of Al wire in all radiographs to align the images. In this method, the first initial radiograph before freeze-thaw cycles is used as a reference and the rest of the radiographs are aligned so that the location of the Al wire matches. The backgrounds of the scans were compared and found to be statistically similar. This allowed each sample to be compared directly. Next, the radiographs from the subsequent samples are subtracted from the first radiograph to investigate any changes in the sample such as damage caused by the freeze-thaw cycles. The subtracted images were then used to determine the percentage of damaged paste. This was found by dividing the total number of pixels that changed in comparison to the initial radiograph before applying freeze-thaw cycles.

5.2.3.2. Segmentation of XCT datasets

Figure 5.3 shows an overview of the procedure for segmenting cracks and air voids. A median filter with a radius of 1 pixel was first used to reduce noise in the image yet preserve the edges [144, 151, 152]. The Otsu method was then used to segment all air voids and cracks from the rest of the mortar constituents. This method is a common and well-established segmentation method that minimizes the mean square errors between the original and binarized images. More detail can be found in other publications [115, 154, 155]. Next, a morphological analysis was used to distinguish air voids and cracks in the segmented image. All spherical-shaped voids are identified as air voids. After identifying the air voids, cracks were segmented by subtracting the air voids from the initial segmented image. The remaining material was then assigned to be paste and is shown as white in Figure 5.3.

It should be noted that in the samples ponded with KI solution, some cracks are filled with KI solutions and so the gray values contrast of the cracks and paste varies in different images. Therefore, cracking could only be investigated in the samples ponded in water.

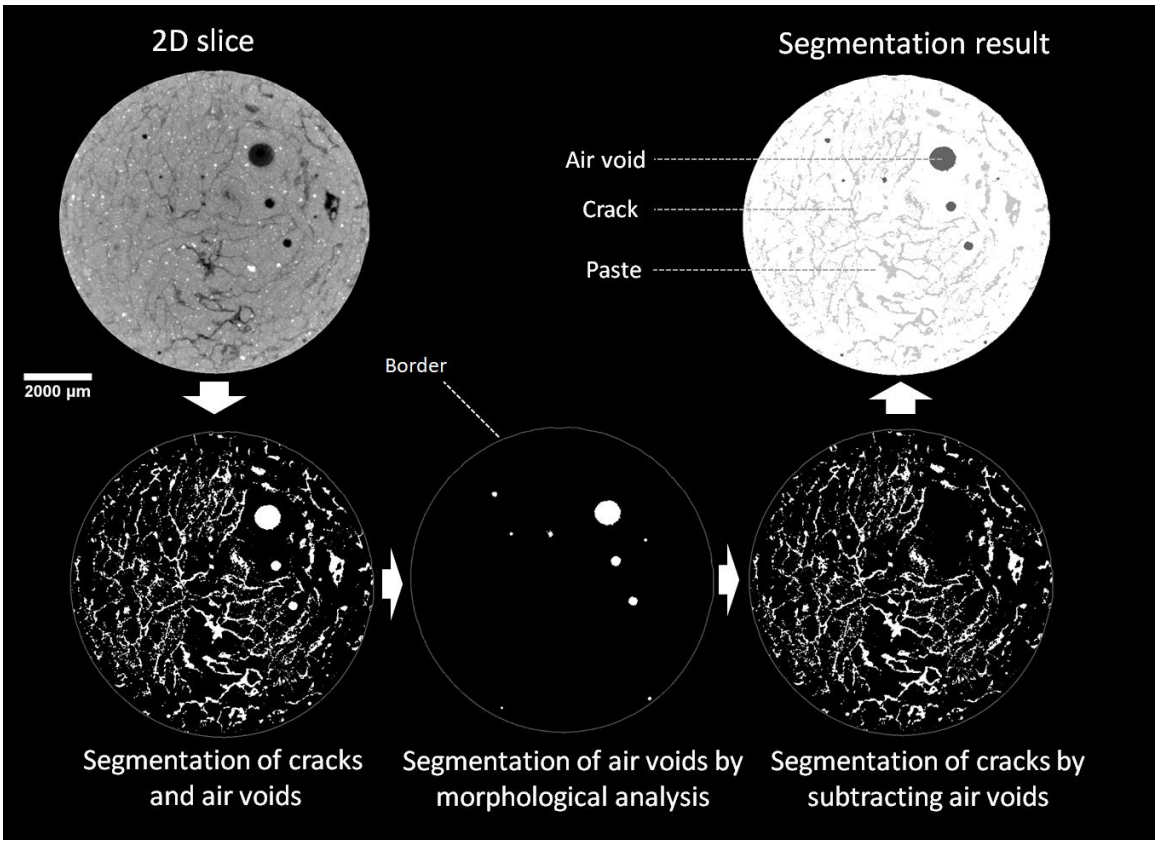

Fig. 5.3. Segmentation process of paste constituents including air voids, cracks, and paste.

To investigate crack and air void distribution at different distances from the bottom of the VOI, the percentage of each constituent is calculated at different locations. The average distance between air voids was also determined by calculating the average nearest-neighbor distance between individual air voids. In this process, the nearest neighbor air void for each individual air void is detected and their distance is recorded. The average of the recorded distances for the all individual air voids was then calculated as the average distance between air voids.

5.3. Results and Discussion

5.3.1. Percentage of damaged paste

Figures 5.4 and 5.5 show the radiographs and the subtracted images taken from the paste samples ponded with KI or water at different time periods of the curing and freeze-thaw cycles. The first radiograph before ponding in each sample is used as a reference for the subtracted images. The black regions in the subtracted images at different freeze-thaw cycles imply damage from freezing and thawing. According to the figure, the non-air-entrained sample (nAE) has experienced a severe freeze-thaw damage compared to the air-entrained samples ponded with KI solution. The same observation was made for the paste samples ponded with water shown in Figure 5.5. However, no significant damage was observed in the air-entrained samples ponded with water.

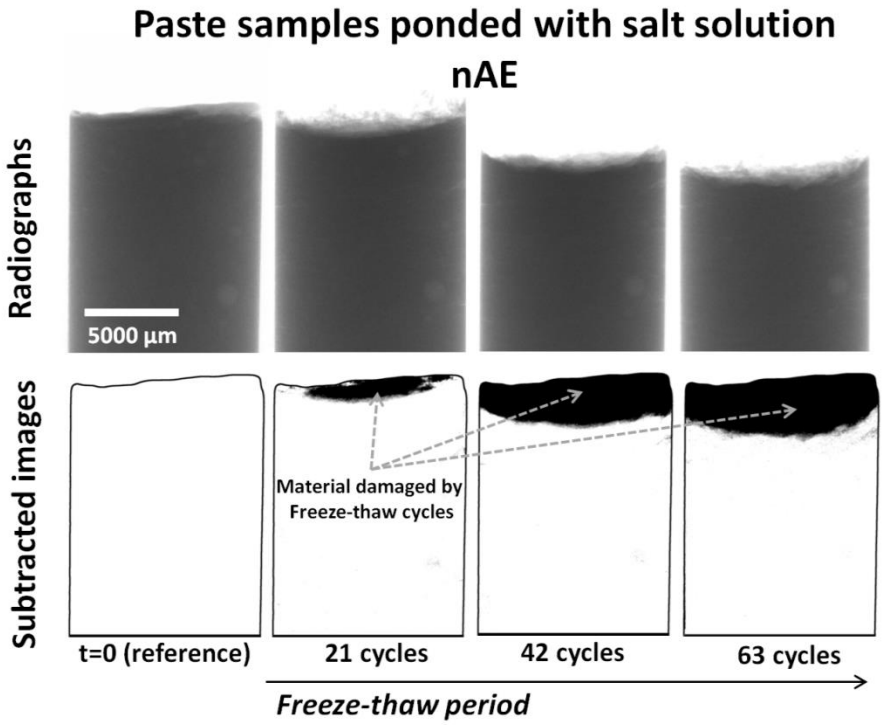

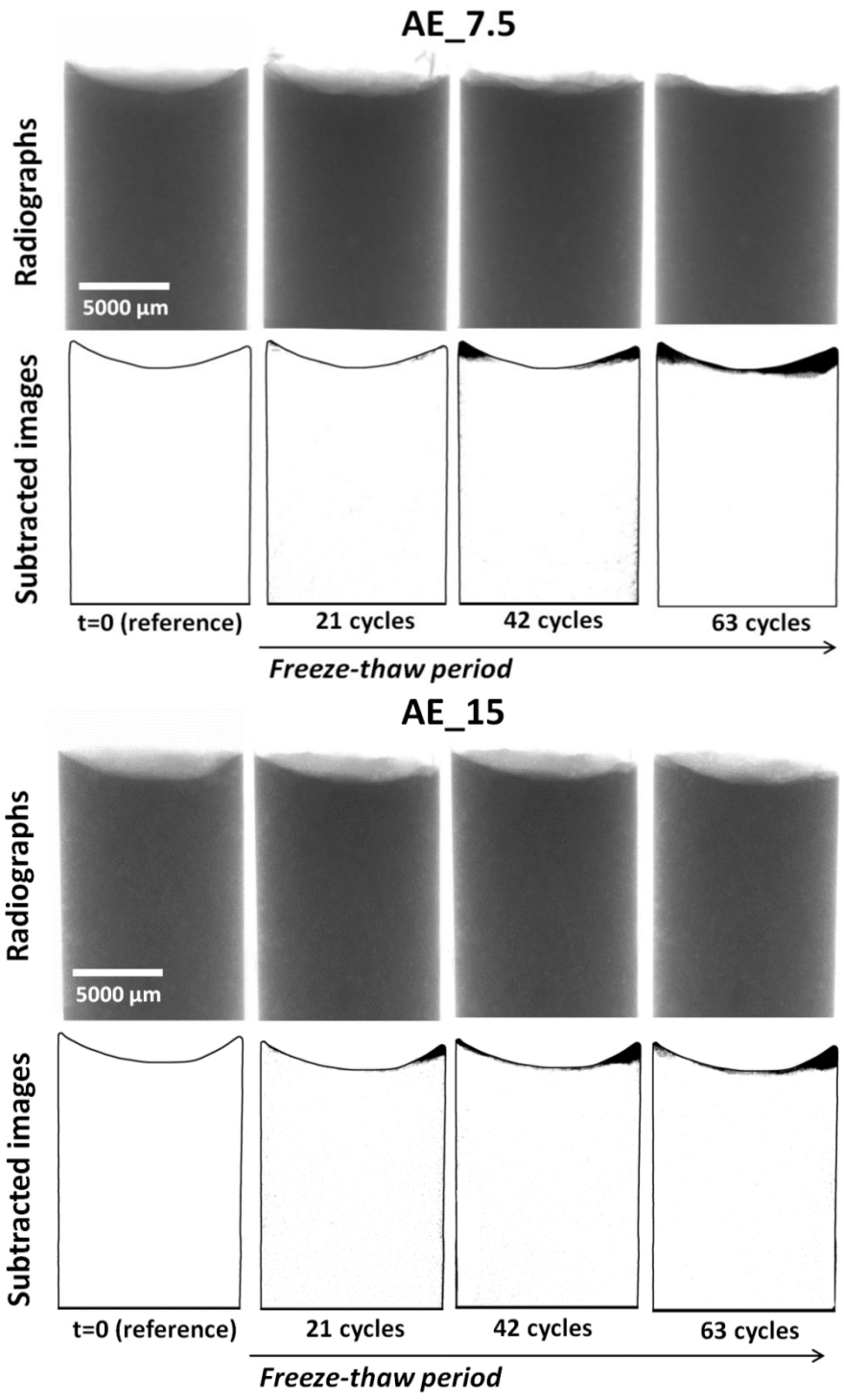

Fig. 5.4. The radiographs and the subtracted images collected from the paste samples ponded with KI solution at different time series during the ponding and freeze-thaw cycles.

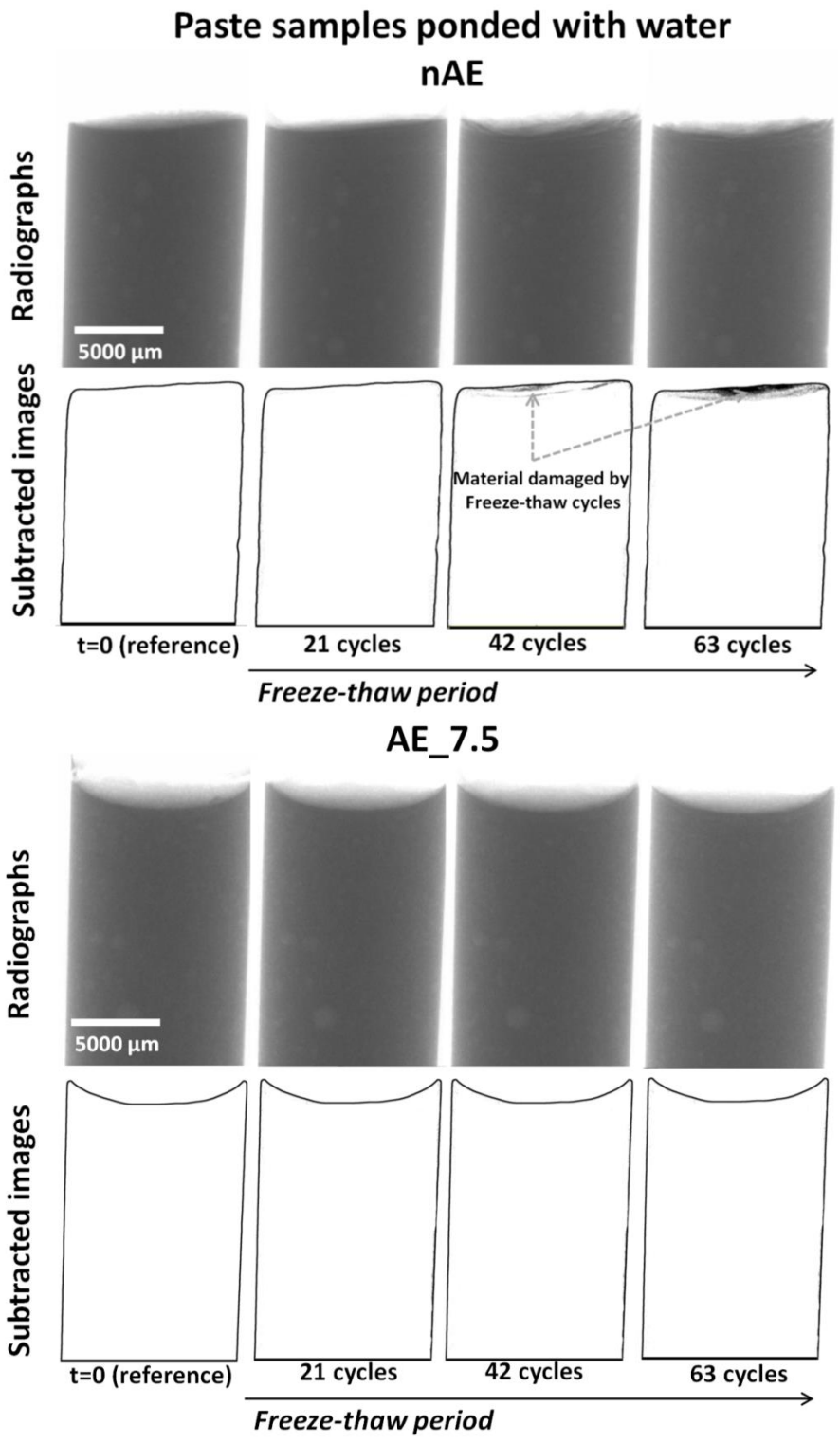
Paste samples ponded with water
nAE
Radiographs
5000 µm
Subtracted images
Material damaged by
Freeze-thaw cycles
t=0 (reference)
21 cycles
42 cycles
63 cycles
Freeze-thaw period
AE_7.5
Radiographs
5000 µm
Subtracted images
t=0 (reference)
21 cycles
42 cycles
63 cycles
Freeze-thaw period

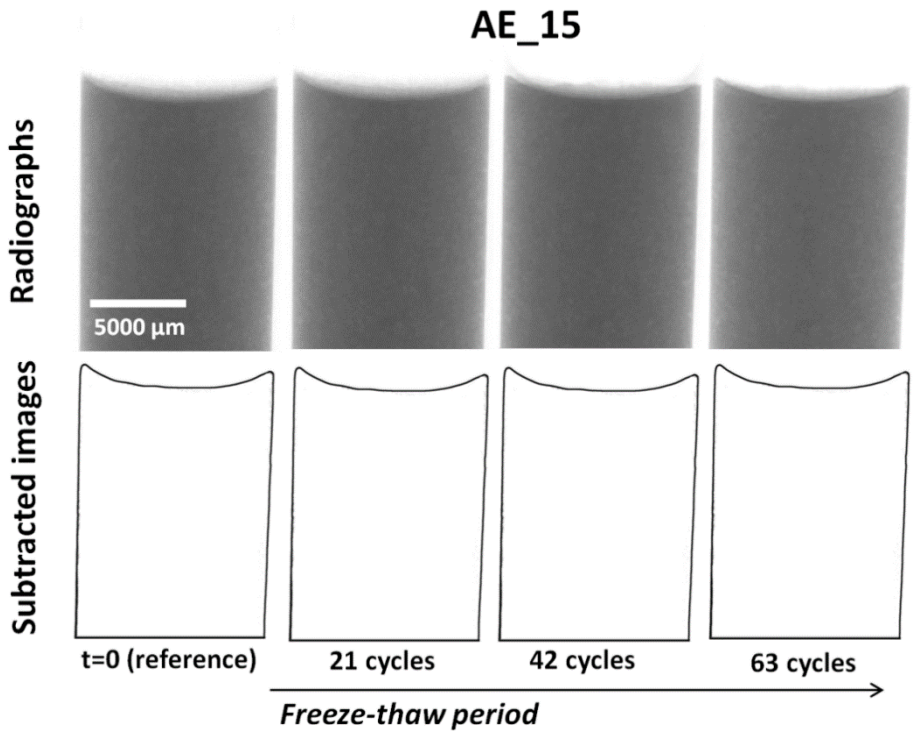

Fig. 5.5. The radiographs and the subtracted images collected from the paste samples ponded with water at different time series during the ponding and freeze-thaw cycles.

While the investigation of the radiographs and subtracted images provide important qualitative insights, it can also be used to perform quantitative analyses such as finding the percentage of damaged paste. Figure 5.6 shows the percentages of damaged paste in different samples for different freeze-thaw cycles. According to this figure, samples without air-entraining agent showed the highest level of damage compared to the air-entrained samples after 63 freeze-thaw cycles. The damage percentage in the sample Salt_nAE is ≈ 6.5x higher than the percentage of damaged paste in the Salt_AE_7.5 and Salt_AE_15 after 63 freeze-thaw cycles. The sample Water_nAE experienced 2% damage while there was no detectable damage observed in the samples Water_AE_7.5 and Water_nAE_15. These differences in the freeze-thaw damage could be caused by the presence of well-distributed air voids in the air-entrained samples. It is widely known that the use of air-entrainment can improve resistance to freeze-thaw damage [136, 159].

As expected, samples ponded with the salt solution had a higher rate of the freeze-thaw damage (≈ 3x) compared to the samples ponded with water since the salt solution accelerate the freeze-thaw damage. It is reported that salt chemically reacts with some of the cement hydrates and new materials form in the pores also the salt solution causes an increase in the vapor pressure or moisture content which inturn increases the degree of saturation. All of these will increase the level of freeze-thaw damage over just using water [162-164, 171].

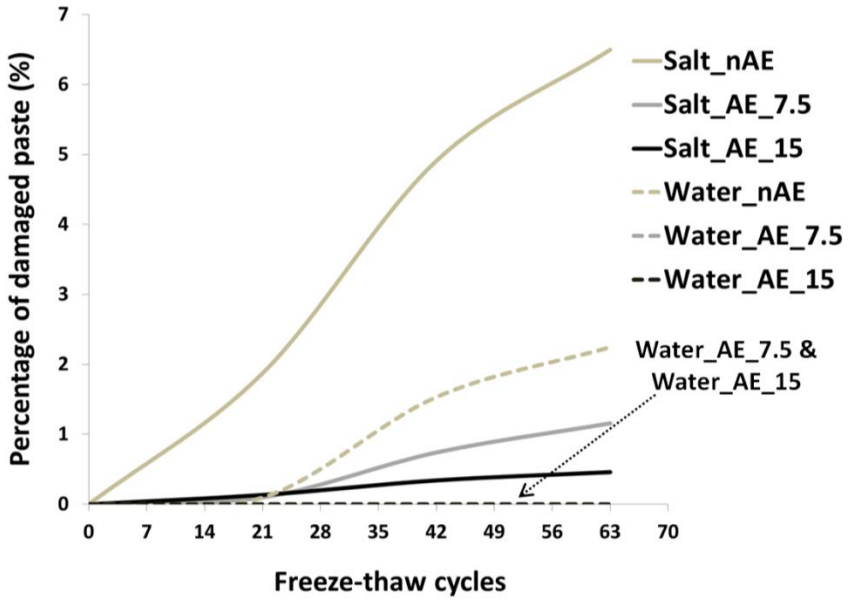

Fig. 5.6. Percentage of damaged paste.

5.3.2. Analysis of XCT datasets

5.3.2.1. Crack propagation after 84 freeze-thaw cycles

Figure 5.7 shows the 3D rendering, 2D slice, and distribution of crack at different distances from the bottom of VOI for the non-air-entrained sample ponded with water. As previously mentioned, the cracks were not analyzed in the paste samples ponded with salt solution (KI) because of the poor gray value contrast between the KI filled cracks and the paste. According to the 3D rendering, the cracks are distributed throughout the sample. The total measured volume of crack

is 14.85%. No crack was observed in the air-entrained samples ponded with water with the current resolution of the scans. Figure 5.7 shows the crack distribution at different distances within the sample. The cracks seem to be primarily forming within ≈ 620 μm of the surface of the sample after 84 freeze-thaw cycles. This higher level of damage is likely caused because of the higher degree of saturation at the surface exposed to the ponded water. Except the surface of the sample, the cracks are uniformly distributed at different distances with average volume of 14% for this sample. It was also observed in the 2D slice shown in Figure 5.7 that the cracks within ≈ 2000 μm of the surface of the sample are wider and have a circular pattern compared to the rest of the cracks farther from the top of the sample which are thinner and have random patterns.

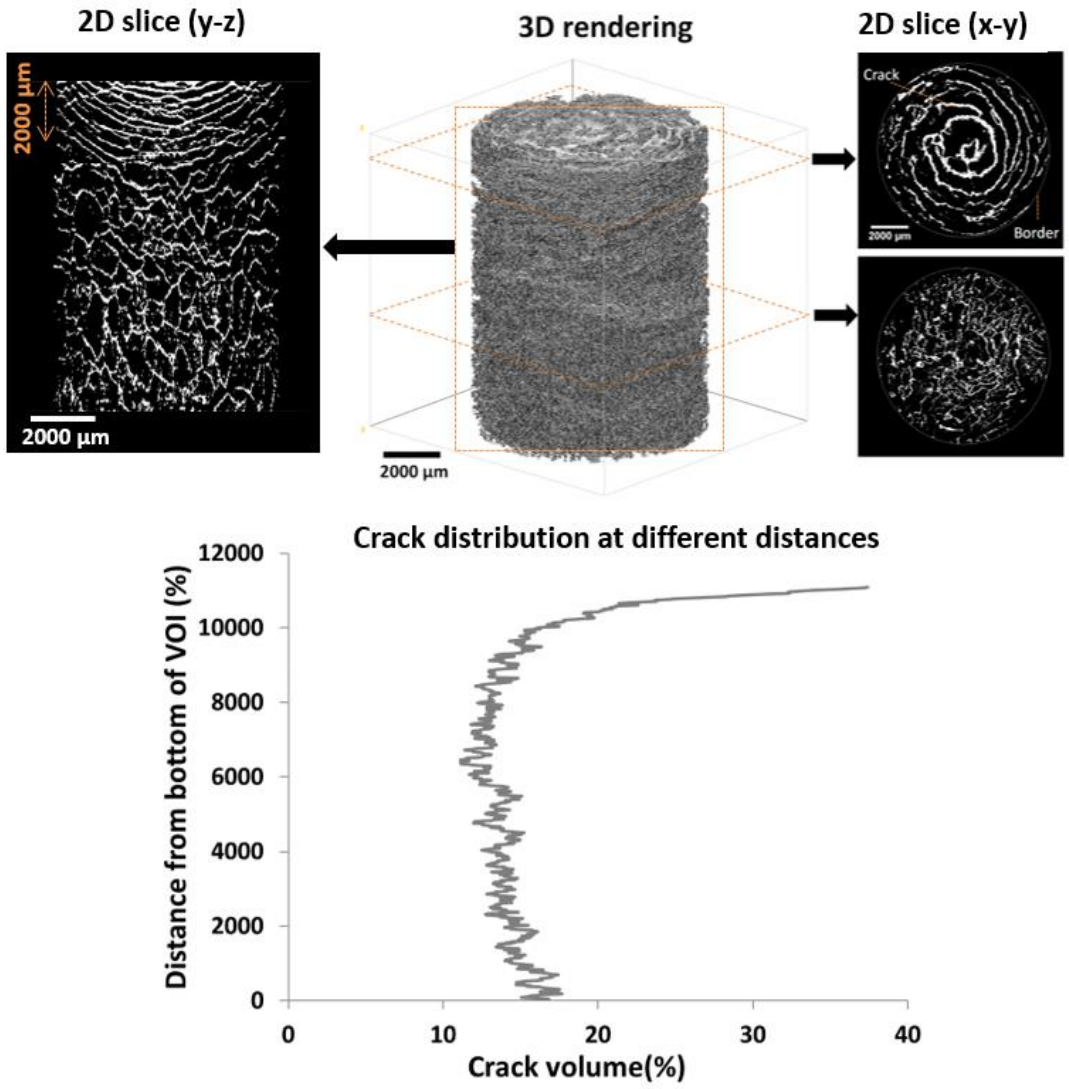

Fig. 5.7. 3D rendering, 2D slice, and distribution of crack at different distances from the bottom of VOI for the sample Water_nAE.

5.3.2.2. 3D analysis of air void system

Figure 5.8 shows the 3D rendering and spatial distribution of the air voids in the non-air-entrained and air-entrained samples ponded with salt. According to this figure, the amount of air voids in the air-entrained sample is significantly higher compared to the non-air-entrained sample. The voids are also more uniformly distributed in AE_7.5 and AE_15 samples. This uniform air void

distribution with adequate air void spacing is important to resist damage during freezing events [159, 172-175].

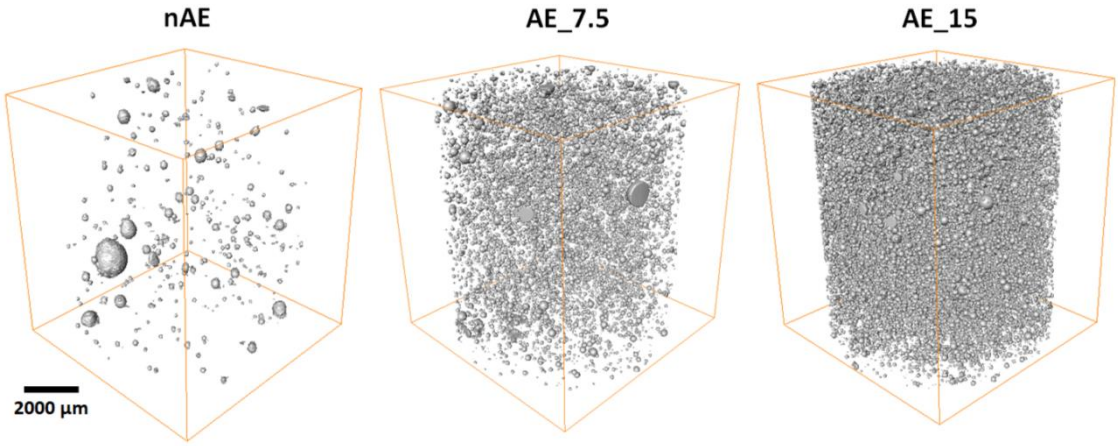

Fig. 5.8. 3D rendering of the air void distribution in the non-air-entrained and air-entrained samples ponded with salt.

Table 5.4 compares the air void volume calculated from XCT datasets, and the mixture design for the samples ponded with salt. In addition, air content measured by XCT data in air-entrained samples AE_7.5 and AE_15 was 2.5% and 9.5%, respectively. However, the air contents measured in the mortar for samples AE_7.5 and AE_15 was 7.5% and 15% by volume of paste, respectively. There is roughly a 5% difference for both of these samples and a 1% difference in the measurements for the sample without AEA.

Table 5.4. Air void content calculated by XCT data and mixture design for the specimens ponded with salt.

Sample	Average distance between air voids (µm)	Air void content (%) XCT analysis	Air void content in fresh mortar (%)
nAE	82	0.48	1.5
7.5% AE	45	2.5	7.5
15% AE	43	9.5	15

To further evaluate the differences between volumes of air voids calculated by XCT and mixture design, the air void distribution at different distances from the bottom of the VOI for the non-air-entrained and air-entrained samples is shown in Figure 5.9. In this figure, the air voids are randomly distributed in the sample "nAE", while the volume of air voids decreases from ≈ 4% to ≈ 2% and from ≈12% to ≈ 6% in the samples AE_7.5 and AE_15, respectively from the bottom to the surface of the samples. This decrease in the volume of air voids near the surface of the air-entrained samples could be caused by air void filling with the solution during the freeze-thaw cycles resulted in an underestimation of air content calculated by XCT datasets. In addition, the air voids smaller than the resolution of XCT cannot be detected.

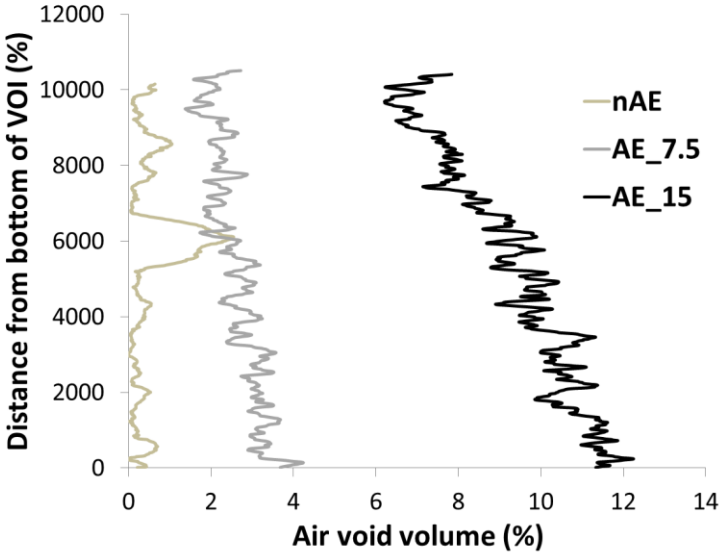

Fig. 5.9. Air void distribution at different distances from the bottom of the VOI for the non-air-entrained and air-entrained samples.

Figure 5.10 shows the air void size distribution of non-air-entrained and air-entrained samples. According to this figure, the majority of the air voids (≈ 75%) are distributed in size ranges between 15 to 60 μm, irrespective of the type of sample (nAE or AE).However, the air void size distribution in the non-air-entrained sample is ≈ 3x and ≈ 8x lower in numbers compared to the

sample AE_7.5 and AE_15, respectively. This suggests that the amount of the small air voids is another factor that affects the freeze-thaw damage of the paste samples.

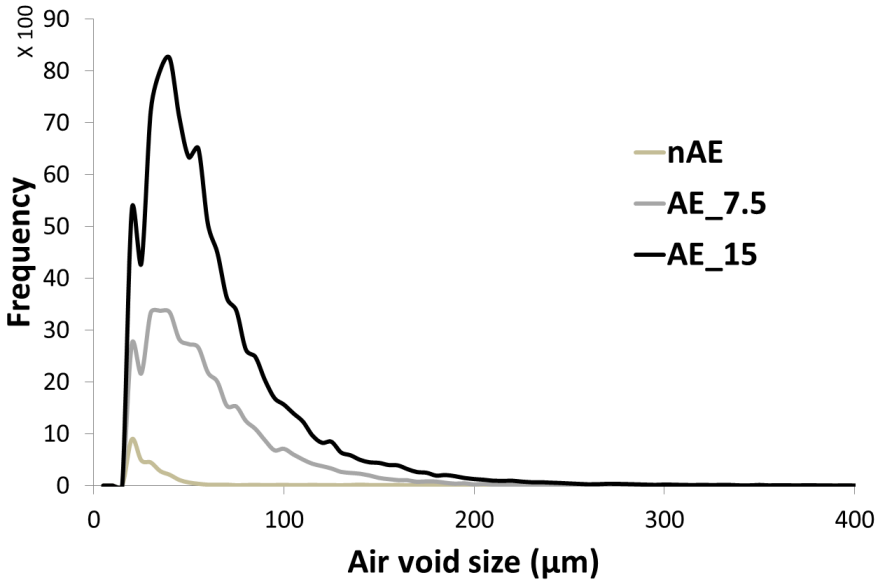

Fig. 5.10. Air void size distributions of non-air-entrained and air-entrained samples.

5.3.2.3 Evaluation of air void spacing and air void filling

In order to provide an insight into the distance between air voids, which is an important factor that affects the freeze-thaw durability of the cement paste, the spatial distribution of the air void for the samples ponded with salt is shown in Figure 5.11. The number of individual air voids found with the current resolution of scans were ≈ 3000, 36,000, and 78,000 for the non-air-entrained, 7.5% and 15% air-entrained samples, respectively. Figure 5.11 shows that the majority of voids are at distance smaller than 100 µm from each other for both non-air-entrained and air-entrained samples. It also seems that the distance between the voids in the sample with a higher air percentage (AE_15) is smaller than the sample with moderate air content (AE_7.5). This was expected as the total volume and number of voids are higher in AE_15. Because of the significantly lower number of voids in nAE sample, the graph cannot be used to compare this

sample with the air entrained samples. Therefore, the average void distances in different samples are quantified.

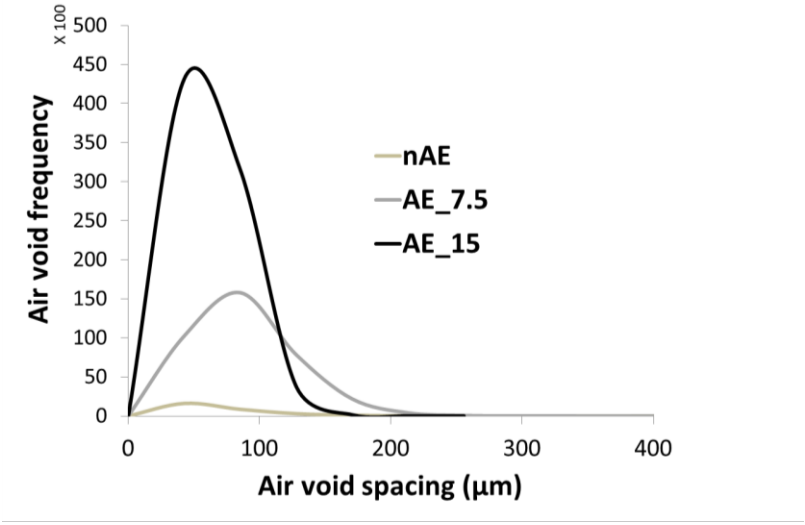

Fig. 5.11. Air void spacing distribution for non-air-entrained and air-entrained samples.

For further investigation of air void spacing and provide an insight into how the air void spacing changes over the depth of the samples, the air void spacing in top 1420 µm, bottom 1420 µm, and the entire sample was determined for the samples and shown in Table 5.5. According to this table, the average distance between air voids for the entire sample in the non-air-entrained is ≈ 1.8x higher than the average distance between air voids in the air-entrained samples. This high air void spacing in the non-air-entrained sample is important because this sample showed poor freeze-thaw performance. This means that in the non-air-entrained sample, freezing water would need to travel larger distance to reach the nearest escape boundary during the freeze-thaw cycles which would cause increased pressures and damage in the sample [172].

In addition, Table 5.5 shows an increase in air void spacing at the top 1420 µm compared to the rest of the VOI for all non-air-entrained and air-entrained samples. This suggests higher air void filling with the solution in the top of the samples compared to the bottom which is similar to the observations obtained from the air void distribution at different distances from the bottom of the

VOI of the specimens. These differences are also evaluated by the student's T-Test to investigate if the obtained results are statistically significantly different. For the non-air-entrained sample, a p value of < 0.1 was obtained for the air void spacing at the top and bottom 1450 µm which showing that these differences in the non-air-entrained sample are not statistically significant. However, for air-entraiend samples the p value was < 2.5E-12. This shows that for non-air-entrained samples, the results are statistically significantly different with a 95% confidence interval. In other words, there is a statistically significant difference between the air void spacing at top 1450 µm of the samples to the air void spacing at bottom 1450 µm of the samples.

In order to visualize the air void filling, examples of the 2D cross-section of the samples nAE and AE_15 ponded in salt are shown in Figure 5.12. Therefore, it is likely that the decrease in volume of air voids from air void filling causes a higher degree of saturation and freeze-thaw pressure which leads to freeze-thaw damage of the samples.

Table 5.5. Average air void spacing in the top 1420 µm, bottom 1420 µm, and entire sample for the specimens ponded with salt.

Average distance between air voids (µm)						
Sample	Entire sample (µm)	SE	Top 1420 µm	SE	Bottom 1420 µm	SE
nAE	82	0.93	82	0.93	78	1.15
7.5% AE	45	0.19	47	0.19	43	0.33
15% AE	43	0.07	44	0.07	41	0.12

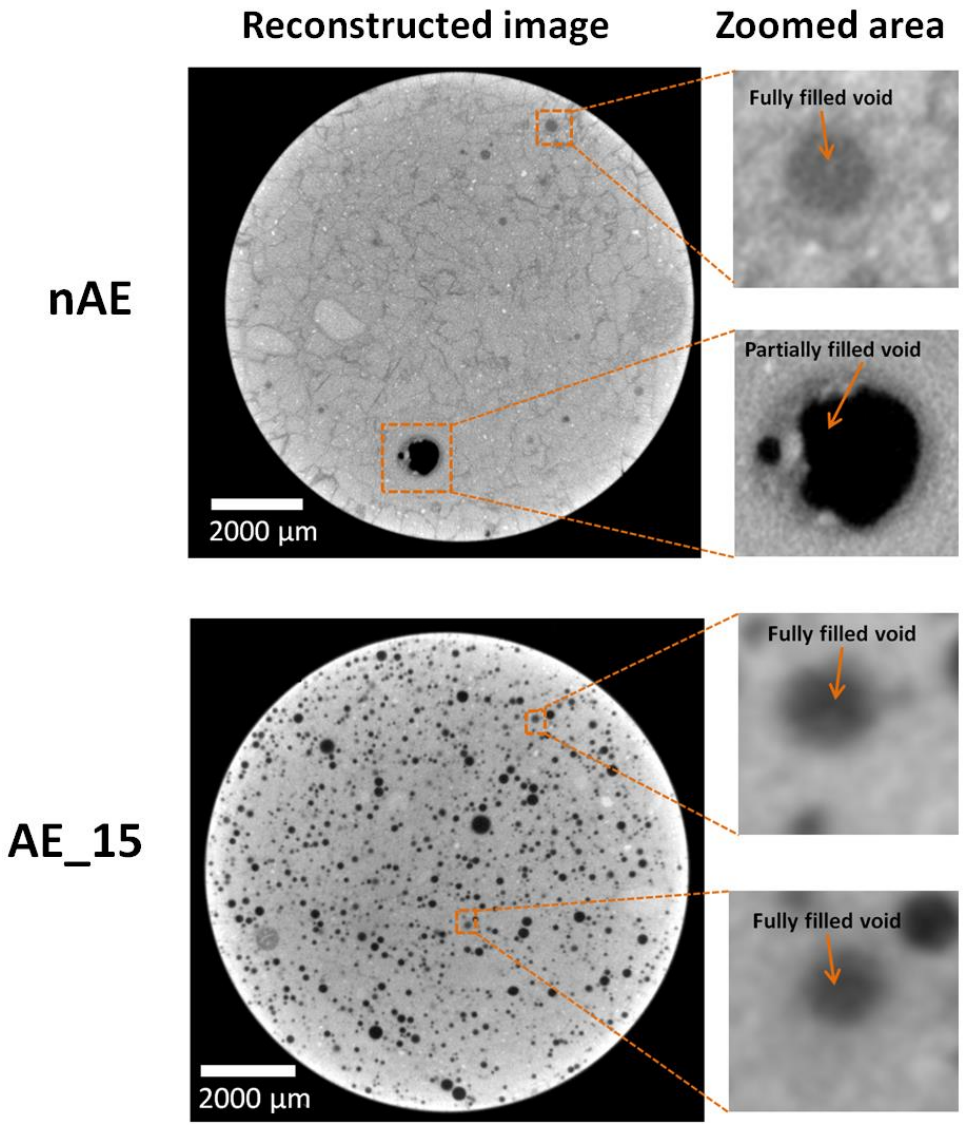

Fig. 5.12. Examples of air void filling in sample nAE and AE_15 ponded with salt.

5.4. Conclusion

In this study, cement paste samples with different air contents were examined with two methods of X-ray imaging to investigate the influence of AEA on the frost durability of cement paste exposed to moisture and subsequent freeze-thaw cycles. The first method used time series radiographs taken at different freeze-thaw cycles to provide useful information about the freeze-

thaw damage of cement paste. In addition, XCT was used to provide direct observations of the amount of cracking, crack volume, void distribution, and void spacing. The following conclusions could be drawn from this work:

- The radiographs showed that the volume of damaged paste in the non-air-entrained samples ponded with salt solution was 6.5x higher than the air entrained samples.
- More than 20% of the sample volume was cracked within 620 μm of the surface of the non-air-entrained sample ponded with salt solution.
- Approximately 75% of the air voids within both the non-air-entrained and air-entrained samples are distributed in size ranges between 15 to 60 μm.
- The average distance between air voids in the non-air-entrained sample was 1.8x higher than the average distance between the air voids in the air-entrained samples.
- The differences in average air void spacing at the top 1420 □m compared to the rest of the VOI different distances could suggest that the surface of the non-air-entrained and air-entrained samples experienced more air void infilling compared to the rest of the samples.

These results show that X-ray imaging is a powerful technique that can be used to better understand both the air void system and provide new insights into the nature and extent of damage in cementitious materials from frost durability.

Work is needed to investigate how the void size, volume, and spacing may impact the void filling observed in this work and to investigate the chemistry of the void filling materials would also be useful.

CHAPTER VI

CONCLUSION

In this dissertation, XCT is used to study different features within materials at multiple length scales. After acquisition of the XCT data, the images were analyzed to obtain useful information from the datasets. For this purpose, based on the quality of the collected images and the goal of the study, appropriate image processing techniques were developed to investigate the microstructure of materials examined.

6.1. 3D Microstructure Biomass Particles before and after Fast Pyrolysis

First, XCTis used to investigate the 3D microstructure of switchgrass, crystalline cellulose, and tall fescue biomass particles in raw and charred condition. In this process, “local mean and standard deviation” segmentation method was found to be accurate to separate biomass constituents. The segmented datasets were then used for further quantitative analyses and the following conclusions were drawn from the results:

- The raw switchgrass particles have a lower density than other raw biomass samples since they had the highest air content and the lowest high absorption materials compared to the other raw particles.

- In contrast, raw crystalline cellulose was denser than raw tall fescue since it had higher high absorption materials compared to the tall fescue particles while the air content was similar in both particles.

- Switchgrass had a char with a porosity that was 1.4x higher compared to the crystalline cellulose char and 8.6x higher porosity compared to the tall fescue char.

- High absorption materials in crystalline cellulose in both raw and charred states are at least 2x smaller than the size of high absorption materials in other biomass particles.

- Except the charred tall fescue, air voids in all specimens are connected.

- The volume distribution of matter and voids was constant over the depth for the charred and raw materials.

6.2. Characterization of Aggregate Gradation in Hardened Concrete

Next, the packing of aggregates in the hardened concrete with a range of workability caused by different aggregate gradations was investigated. The Otsu method which is an automated segmentation algorithm was used to separate the air voids in the concrete samples. While the Otsu thresholding method was useful to segment the air voids, it was not helpful to separate the aggregates from the paste as the peaks in the gray level histogram overlap. In order to resolve this issue, Otsu method was utilized after an initial image pre-processing and then some post-processing was used to modify the images. The 3D segmented XCT datasets were used to classify the aggregates based on their size. The following conclusions were drawn from this chapter:

- When a mixture had < 20% retained on a given sieve size the mixture showed satisfactory workability, a uniform aggregate spacing, and all cross sections consisted of at least 10% aggregate.

- When a mixture had > 20% retained on a given sieve size the mixture showed poor workability, a spacing between aggregates of < 600 μm for more than 70% of the aggregates in the mixture, and cross sections were observed where no aggregate was present.

- These findings suggest that when > 20% is retained on a given sieve size then the coarse aggregate spacing is not uniform and there is observable segregation within the mixture. However, when the amount retained on a given sieve is < 20% then the aggregate distribution is more uniform.

6.3. Mortar with Different DOS and AEA Subjected to Single Freeze-thaw Cycle

In addition, mortar samples made with different air content and degree of saturation were examined with XCT to investigate microstructural changes caused by a single freeze-thaw cycle. In this process, Otsu thresholding technique was used first to segment the cracks and air voids in the mortar samples as the gray value contrasts of these phases were high enough to use the automated method. The Otsu method was not useful to segment aggregates because of the low contrast between the gray values for the aggregate and paste. In order to overcome this, "local mean and standard deviation" segmentation method was used to separate aggregates from paste. Based on the results obtained from this dataset:

- Crack initiation and propagation were primarily observed within ≈ 970 μm of the top surface of the sample with DOS ≈ 100% (nAE_100) after a single freeze-thaw cycle.
- A single freeze-thaw cycle caused an increase in the volume of crack within aggregate by 4.5x and an increase in the volume of crack within the paste by a factor of 13 compared to the volume of crack before freeze-thaw cycle.
- Most of the newly-formed cracks occur in aggregate after the freeze-thaw cycle.
- All samples experienced air void filling mostly located within ≈ 700 μm of the top surface of the samples.
- The voids smaller than 20 μm in the samples with DOS between 85% and 95% showed more than 70% filling after a single freeze-thaw cycle.

- Sample nAE_100 showed the most damage and the lowest percentage of filled voids.
- The replicate samples with DOS of 93% showed very similar void filling for voids smaller than 75 μm.

6.4. Cement Paste with Different AEA Subjected to Freeze-thaw Cycles

Finally, cement paste samples with different air contents were examined with two methods of X-ray imaging to investigate the influence of AEA on the frost durability of cement paste exposed to moisture and subsequent freeze-thaw cycles. The image processing and data interpretation in this study was similar to the investigated mortar. The following conclusions were drawn in this chapter:

- The radiographs showed that the volume of damaged paste in the non-air-entrained samples ponded with the salt solution was 6.5x higher than the air entrained samples.
- More than 20% of the sample volume was cracked within 620 μm of the surface of the non-air-entrained sample ponded with the salt solution.
- Approximately 75% of the air voids within both the non-air-entrained and air-entrained samples are distributed in size ranges between 15 to 60 μm.
- The average distance between air voids in the non-air-entrained sample was 1.8x higher than the average distance between the air voids in the air-entrained samples.
- The differences in average air void spacing at the top 1420 μm compared to the rest of the VOI different distances could suggest that the surface of the non-air-entrained and air-entrained samples experienced more air void infilling compared to the rest of the samples.

6.5. Future works

These results show that XCT is a powerful non-destructive method that is useful for a better understanding and characterization of different features within materials. However, this work may be extended to a wider range of problems where XCT can be used to understand the other feature of materials. The list of future works is as follows:

- Work is ongoing to investigate 3D microstructure for more kinds of biomass particles before and after charring for different pyrolysis conditions.
- More works are needed to understand a wider range of problems where aggregate distribution or performance is important.
- Research is needed to investigate how the void size, volume, and spacing may impact the void filling observed in the mortar subjected to the single freeze-thaw cycle and how multiple freeze-thaw cycles will impact the results.
- Additional experiments are needed to investigate the chemistry of the filling materials in the mortar and paste samples subjected to freeze-thaw cycles.

REFERENCES

[1] J.C.-M. Li, Microstructure and Properties of Materials:(Volume 2), World Scientific Publishing Company2000.
[2] K.G.F. Janssens, D. Raabe, E. Kozeschnik, M.A. Miodownik, B. Nestler, Computational materials engineering: an introduction to microstructure evolution, Academic Press2010.
[3] Wonderopolis, What Is the Smallest Thing You Can See, 2018.
[4] R.D. Allen, L.R. Zacharski, S.T. Widirstky, R. Rosenstein, L.M. Zaitlin, D.R. Burgess, Transformation and motility of human platelets: details of the shape change and release reaction observed by optical and electron microscopy, The Journal of cell biology, 83 (1979) 126-142.
[5] A.M. Glauert, P.J. Goodhew, Practical methods in electron microscopy, North-Holland Amsterdam1972.
[6] M.A. Hayat, Principles and techniques of electron microscopy. Biological applications, Edward Arnold.1981.
[7] L. Wang, B. Yang, A. Abraham, L. Qi, X.Y. Zhao, Z.X. Chen, Construction of dynamic three-dimensional microstructure for the hydration of cement using 3D image registration, Pattern Anal Appl, 17 (2014) 655-665.
[8] R. Henderson, The potential and limitations of neutrons, electrons and X-rays for atomic resolution microscopy of unstained biological molecules, Quarterly reviews of biophysics, 28 (1995) 171-193.
[9] B.A. Christiansen, Effect of micro-computed tomography voxel size and segmentation method on trabecular bone microstructure measures in mice, Bone Rep, 5 (2016) 136-140.
[10] Q. Hu, M. Aboustait, T. Kim, M.T. Ley, J.C. Hanan, J. Bullard, R. Winarski, V. Rose, Direct three-dimensional observation of the microstructure and chemistry of C3S hydration, Cement and Concrete Research, 88 (2016) 157-169.
[11] M.M.A. Romao, M.M. Marques, A.R.G. Cortes, A.C.R.T. Horliana, M.S. Moreira, C.A. Lascala, Micro-computed tomography and histomorphometric analysis of human alveolar bone repair induced by laser phototherapy: a pilot study, Int J Oral Max Surg, 44 (2015) 1521-1528.
[12] Q. Hu, M. Aboustait, T. Kim, M.T. Ley, J.W. Bullard, J.C. Hanan, G. Scherer, V. Rose, R. Winarski, J. Gelb, Direct measurements of 3d structure, chemistry and mass density during the induction period of C3s hydration, Cement and Concrete Research, 89 (2016).

[13] S.T. Erdogan, E.J. Garboczi, D.W. Fowler, Shape and size of microfine aggregates: X-ray microcomputed tomography vs. laser diffraction, Powder Technol, 177 (2007) 53-63.
[14] E.J. Garboczi, Three-dimensional mathematical analysis of particle shape using X-ray tomography and spherical harmonics: Application to aggregates used in concrete, Cement and Concrete Research, 32 (2002) 1621-1638.
[15] R.C.K. Wong, K.T. Chau, Estimation of air void and aggregate spatial distributions in concrete under uniaxial compression using computer tomography scanning, Cement and Concrete Research, 35 (2005) 1566-1576.
[16] D.P. Bentz, S. Mizell, S. Satterfield, J. Devaney, W. George, P. Ketcham, J. Graham, J. Porterfield, D. Quenard, F. Vallee, H. Sallee, E. Boller, J. Baruchel, The Visible Cement Data Set, J Res Natl Inst Stan, 107 (2002) 137-148.
[17] D.P. Bentz, D.A. Quenard, H.M. Kunzel, J. Baruchel, F. Peyrin, N.S. Martys, E.J. Garboczi, Microstructure and transport properties of porous building materials. II: Three-dimensional X-ray tomographic studies, Mater Struct, 33 (2000) 147-153.
[18] K.Y. Kim, T.S. Yun, K.P. Park, Evaluation of pore structures and cracking in cement paste exposed to elevated temperatures by X-ray computed tomography, Cement and Concrete Research, 50 (2013) 34-40.
[19] T.T. Nguyen, Modeling of complex microcracking in cement based materials by combining numerical simulations based on a phase-field method and experimental 3D imaging, Université Paris-Est, 2015.
[20] S.K. Sinha, P.W. Fieguth, Automated detection of cracks in buried concrete pipe images, Automat Constr, 15 (2006) 58-72.
[21] Q. Hu, M. Aboustait, M.T. Ley, J.C. Hanan, V. Rose, R. Winarski, Combined three-dimensional structure and chemistry imaging with nanoscale resolution, Acta Materialia, 77 (2014) 173-182.
[22] Q.N. Hu, M.T. Ley, J. Davis, J.C. Hanan, R. Frazier, Y.L. Zhang, 3D chemical segmentation of fly ash particles with X-ray computed tomography and electron probe microanalysis, Fuel, 116 (2014) 229-236.
[23] M.T. Ley, Q. Hu, M. Aboustait, T. Kim, M. Moradian, J. Hanan, V. Rose, R. Winarski, J. Gelb, Combining Nano X-ray Tomography and Nano X-ray Fluorescence to Create Time-dependent Three Dimensional Constitutive Maps, 2nd International Conference on Tomography of Materials and StructuresQuebec City, Canada, 2015.
[24] E. Gallucci, K. Scrivener, A. Groso, M. Stampanoni, G. Margaritondo, 3D experimental investigation of the microstructure of cement pastes using synchrotron X-ray microtomography (mu CT), Cement and Concrete Research, 37 (2007) 360-368.
[25] Q. Hu, M. Aboustait, T. Kim, M.T. Ley, J. Bullard, G. Scherer, J.C. Hanan, V. Rose, R. Winarski, J. Gelb, Direct measurements of 3d structure, chemistry and mass density during the induction period of C3s hydration, cement and Concrete Research, 89 (2016) 14-26.
[26] P. Trtik, A. Diaz, M. Guizar-Sicairos, A. Menzel, O. Bunk, Density mapping of hardened cement paste using ptychographic X-ray computed tomography, Cement Concrete Comp, 36 (2013) 71-77.
[27] D. Fukuda, Y. Nara, Y. Kobayashi, M. Maruyama, M. Koketsu, D. Hayashi, H. Ogawa, K. Kaneko, Investigation of self-sealing in high-strength and ultra-low-

permeability concrete in water using micro-focus X-ray CT, Cement and Concrete Research, 42 (2012) 1494-1500.
[28] N. Otsu, A threshold selection method from gray-level histograms, Automatica, 11 (1975) 23-27.
[29] A. Markoe, Analytic tomography, Cambridge University Press, Cambridge ; New York, 2006.
[30] D. Pimentel, T.W. Patzek, Ethanol production using corn, switchgrass, and wood; biodiesel production using soybean and sunflower, Natural resources research, 14 (2005) 65-76.
[31] P.R. Adler, M.A. Sanderson, A.A. Boateng, P.J. Weimer, H.-J.G. Jung, Biomass yield and biofuel quality of switchgrass harvested in fall or spring, Agronomy Journal, 98 (2006) 1518-1525.
[32] C. Fu, J.R. Mielenz, X. Xiao, Y. Ge, C.Y. Hamilton, M. Rodriguez, F. Chen, M. Foston, A. Ragauskas, J. Bouton, Genetic manipulation of lignin reduces recalcitrance and improves ethanol production from switchgrass, Proceedings of the National Academy of Sciences, 108 (2011) 3803-3808.
[33] M.A. Sanderson, P.R. Adler, A.A. Boateng, M.D. Casler, G. Sarath, Switchgrass as a biofuels feedstock in the USA, Canadian journal of plant science, 86 (2006) 1315-1325.
[34] P. Burli, E. Forgoston, P. Lal, L. Billings, B. Wolde, Adoption of switchgrass cultivation for biofuel under uncertainty: A discrete-time modeling approach, Biomass and Bioenergy, 105 (2017) 107-115.
[35] C. Abendroth, C. Simeonov, J. Peretó, O. Antúnez, R. Gavidia, O. Luschnig, M. Porcar, From grass to gas: microbiome dynamics of grass biomass acidification under mesophilic and thermophilic temperatures, Biotechnology for biofuels, 10 (2017) 171.
[36] R. Azargohar, K.L. Jacobson, E.E. Powell, A.K. Dalai, Evaluation of properties of fast pyrolysis products obtained, from Canadian waste biomass, J Anal Appl Pyrol, 104 (2013) 330-340.
[37] W. Torres, S.S. Pansare, J.G. Goodwin Jr, Hot gas removal of tars, ammonia, and hydrogen sulfide from biomass gasification gas, Catalysis Reviews, 49 (2007) 407-456.
[38] Union of concerned scintist (UCS), 2012.
[39] M.S. Mettler, D.G. Vlachos, P.J. Dauenhauer, Top ten fundamental challenges of biomass pyrolysis for biofuels, Energy & Environmental Science, 5 (2012) 7797-7809.
[40] R.D. Perlack, L.L. Wright, A.F. Turhollow, R.L. Graham, B.J. Stokes, D.C. Erbach, Biomass as feedstock for a bioenergy and bioproducts industry: the technical feasibility of a billion-ton annual supply, Oak Ridge National Lab TN, 2005.
[41] E. Biagini, F. Barontini, L. Tognotti, Devolatilization of biomass fuels and biomass components studied by TG/FTIR technique, Industrial & Engineering Chemistry Research, 45 (2006) 4486-4493.
[42] M.J. Antal Jr, Biomass pyrolysis: A review of the literature Part 2—lignocellulose pyrolysis, Advances in solar energy, Springer1985, pp. 175-255.
[43] W.C. Khor, S. Andersen, H. Vervaeren, K. Rabaey, Electricity-assisted production of caproic acid from grass, Biotechnology for biofuels, 10 (2017) 180.
[44] K. Kasthuraiah, N.S. Kishore, Lignocellulosic Biofuels–Challenges And Potentials, Int J Pharma Bio Sci, 8 (2017) 376-381.

[45] W.F. Anderson, D.E. Akin, Structural and chemical properties of grass lignocelluloses related to conversion for biofuels, Journal of industrial microbiology & biotechnology, 35 (2008) 355-366.
[46] T. Thamsiriroj, J.D. Murphy, A critical review of the applicability of biodiesel and grass biomethane as biofuels to satisfy both biofuel targets and sustainability criteria, Applied energy, 88 (2011) 1008-1019.
[47] A. Bridgwater, Principles and practice of biomass fast pyrolysis processes for liquids, J Anal Appl Pyrol, 51 (1999) 3-22.
[48] A. Bridgwater, G. Peacocke, Fast pyrolysis processes for biomass, Renewable and sustainable energy reviews, 4 (2000) 1-73.
[49] F.-X. Collard, J. Blin, A review on pyrolysis of biomass constituents: Mechanisms and composition of the products obtained from the conversion of cellulose, hemicelluloses and lignin, Renewable and Sustainable Energy Reviews, 38 (2014) 594-608.
[50] A. Oasmaa, D. Meier, Norms and standards for fast pyrolysis liquids: 1. Round robin test, J Anal Appl Pyrol, 73 (2005) 323-334.
[51] H. Yang, R. Yan, H. Chen, D.H. Lee, C. Zheng, Characteristics of hemicellulose, cellulose and lignin pyrolysis, Fuel, 86 (2007) 1781-1788.
[52] H. Yang, R. Yan, H. Chen, C. Zheng, D.H. Lee, D.T. Liang, In-depth investigation of biomass pyrolysis based on three major components: hemicellulose, cellulose and lignin, Energy & Fuels, 20 (2006) 388-393.
[53] S.D. Stefanidis, K.G. Kalogiannis, E.F. Iliopoulou, C.M. Michailof, P.A. Pilavachi, A.A. Lappas, A study of lignocellulosic biomass pyrolysis via the pyrolysis of cellulose, hemicellulose and lignin, J Anal Appl Pyrol, 105 (2014) 143-150.
[54] T. Hosoya, H. Kawamoto, S. Saka, Cellulose–hemicellulose and cellulose–lignin interactions in wood pyrolysis at gasification temperature, J Anal Appl Pyrol, 80 (2007) 118-125.
[55] M. Carrier, M. Windt, B. Ziegler, J. Appelt, B. Saake, D. Meier, A. Bridgwater, Quantitative insights into the Fast Pyrolysis of Extracted Cellulose, Hemicelluloses and Lignin, ChemSusChem, (2017).
[56] S. Wu, D. Shen, J. Hu, H. Zhang, R. Xiao, Cellulose-hemicellulose interactions during fast pyrolysis with different temperatures and mixing methods, Biomass and Bioenergy, 95 (2016) 55-63.
[57] T. Chen, L. Li, R. Zhao, J. Wu, Pyrolysis kinetic analysis of the three pseudocomponents of biomass–cellulose, hemicellulose and lignin, Journal of Thermal Analysis and Calorimetry, 128 (2017) 1825-1832.
[58] K. Sakimoto, M. Kanna, Y. Matsumura, Kinetic model of cellulose degradation using simultaneous saccharification and fermentation, Biomass and Bioenergy, 99 (2017) 116-121.
[59] K. Dussan, S. Dooley, R. Monaghan, Integrating compositional features in model compounds for a kinetic mechanism of hemicellulose pyrolysis, Chemical Engineering Journal, (2017).
[60] J.J. Manya, E. Velo, L. Puigjaner, Kinetics of biomass pyrolysis: a reformulated three-parallel-reactions model, Industrial & engineering chemistry research, 42 (2003) 434-441.

[61] J. Orfao, F. Antunes, J.L. Figueiredo, Pyrolysis kinetics of lignocellulosic materials—three independent reactions model, Fuel, 78 (1999) 349-358.
[62] M.J. Paulus, S.S. Gleason, S.J. Kennel, P.R. Hunsicker, D.K. Johnson, High resolution X-ray computed tomography: an emerging tool for small animal cancer research, Neoplasia, 2 (2000) 62-70.
[63] D. Wildenschild, C. Vaz, M. Rivers, D. Rikard, B. Christensen, Using X-ray computed tomography in hydrology: systems, resolutions, and limitations, Journal of Hydrology, 267 (2002) 285-297.
[64] Q. Hu, M.T. Ley, J. Davis, J.C. Hanan, R. Frazier, Y. Zhang, 3D chemical segmentation of fly ash particles with X-ray computed tomography and electron probe microanalysis, Fuel, 116 (2014) 229-236.
[65] P. Tiwari, M. Deo, C. Lin, J. Miller, Characterization of oil shale pore structure before and after pyrolysis by using X-ray micro CT, Fuel, 107 (2013) 547-554.
[66] J. Zhou, H. Zhang, J.-f. Lu, G.-x. Yue, Effect of pyrolysis temperature on porous structure of anthracite chars produced at high temperatures, Journal of Fuel Chemistry and Technology, 35 (2007) 155.
[67] T. Saif, Q. Lin, A.R. Butcher, B. Bijeljic, M.J. Blunt, Multi-scale multi-dimensional microstructure imaging of oil shale pyrolysis using X-ray micro-tomography, automated ultra-high resolution SEM, MAPS Mineralogy and FIB-SEM, Applied Energy, 202 (2017) 628-647.
[68] L. Coshell, R.G. Mclver, R. Chang, X-ray computed tomography of Australian oil shales: non-destructive visualization and density determination, Fuel, 73 (1994) 1317-1321.
[69] T. Saif, Q. Lin, K. Singh, B. Bijeljic, M.J. Blunt, Dynamic imaging of oil shale pyrolysis using synchrotron X-ray microtomography, Geophysical Research Letters, 43 (2016) 6799-6807.
[70] G. Naude, J. Hoffman, S.J. Theron, G. Coetzer, The use of X-ray computed tomography in the characterisation of coal and associated char reductants, Minerals Engineering, 52 (2013) 143-154.
[71] A. Markoe, Analytic tomography, Cambridge University Press2006.
[72] J.D. Murillo, E.A. Ware, J.J. Biernacki, Characterization of milling effects on the physical and chemical nature of herbaceous biomass with comparison of fast pyrolysis product distributions using Py-GC/MS, J Anal Appl Pyrol, 108 (2014) 234-247.
[73] M.O. Adenson, C. Templeton, J.J. Biernacki, Modeling pyrolysis-induced microstructural changes in biomass: A cellular automata approach, Fuel, 210 (2017) 198-206.
[74] B. De Man, J. Nuyts, P. Dupont, G. Marchal, P. Suetens, Reduction of metal streak artifacts in x-ray computed tomography using a transmission maximum a posteriori algorithm, IEEE transactions on nuclear science, 47 (2000) 977-981.
[75] L. Babout, E. Maire, J.-Y. Buffière, R. Fougeres, Characterization by X-ray computed tomography of decohesion, porosity growth and coalescence in model metal matrix composites, Acta Materialia, 49 (2001) 2055-2063.
[76] B. De Man, J. Nuyts, P. Dupont, G. Marchal, P. Suetens, Metal streak artifacts in X-ray computed tomography: a simulation study, IEEE Transactions on Nuclear Science, 46 (1999) 691-696.

[77] S. Charpenay, M.A. Serio, P.R. Solomon, The prediction of coal char reactivity under combustion conditions, Symposium (International) on Combustion, Elsevier, 1992, pp. 1189-1197.
[78] R.H. Hurt, K.A. Davis, N.Y. Yang, T.J. Headley, G.D. Mitchell, Residual carbon from pulverized-coal-fired boilers. 2. Morphology and physicochemical properties, Fuel, 74 (1995) 1297-1306.
[79] K. Miura, K. Hashimoto, P.L. Silveston, Factors affecting the reactivity of coal chars during gasification, and indices representing reactivity, Fuel, 68 (1989) 1461-1475.
[80] M.-L. Chan, J. Jones, M. Pourkashanian, A. Williams, The oxidative reactivity of coal chars in relation to their structure, Fuel, 78 (1999) 1539-1552.
[81] M. Alexander, T. Milne, Influence of cement blend and aggregate type on the stress-strain behavior and elastic modulus of concrete, Materials Journal, 92 (1995) 227-235.
[82] F. de Larrard, A. Belloc, The influence of aggregate on the compressive strength of normal and high-strength concrete, ACI materials journal, 94 (1997) 417-426.
[83] M.S. Meddah, S. Zitouni, S. Belâabes, Effect of content and particle size distribution of coarse aggregate on the compressive strength of concrete, Construction and Building Materials, 24 (2010) 505-512.
[84] K. Wu, B. Chen, W. Yao, Study of the influence of aggregate size distribution on mechanical properties of concrete by acoustic emission technique, Cement and Concrete Research, 31 (2001) 919-923.
[85] S.M. Cramer, M. Hall, J. Parry, Effect of optimized total aggregate gradation on Portland cement concrete for Wisconsin pavements, Transportation research record, (1995) 100-106.
[86] M. Glavind, G.S. Olsen, C. MUNCH-PETERSEN, Packing calculations and concrete mix design, Nordic Concrete Research, 13 (1993).
[87] P. Goltermann, V. Johansen, L. Palbøl, Packing of aggregates: an alternative tool to determine the optimal aggregate mix, ACI Materials Journal, 94 (1997) 435-443.
[88] W. Lindquist, D. Darwin, J. Browning, H.A. McLeod, J. Yuan, D. Reynolds, Implementation of concrete aggregate optimization, Construction and Building Materials, 74 (2015) 49-56.
[89] M. Moini, I. Flores-Vivian, A. Amirjanov, K. Sobolev, The optimization of aggregate blends for sustainable low cement concrete, Construction and Building Materials, 93 (2015) 627-634.
[90] T.C. Powers, The properties of fresh concrete, (1969).
[91] W.B. Fuller, The law of proportioning concrete, Transactions, American Society of Civil Engineers, 59 (1907) 67-143.
[92] A.N. Talbot, F.E. Richart, The strength of concrete, its relation to the cement aggregates and water, University of Illinois at Urbana Champaign, College of Engineering. Engineering Experiment Station., 1923.
[93] M. Anson-Cartwright, Optimization of aggregate gradation combinations to improve concrete sustainability, 2011.
[94] J. Holland, Mixture optimization, Concrete International, 12 (1990) 10.
[95] J.M. Shilstone, J. Shilstone, Performance-based concrete mixtures and specifications for today, Concrete international, 24 (2002) 80-83.
[96] J.M. Shilstone, Performance specifications for concrete pavements, Concrete International, 13 (1991) 28-34.

[97] D.N. Richardson, Aggregate Gradation Optimization--Literature Search, (2005).
[98] D. Cook, A. Ghaeezadeh, T. Ley, Investigation of optimized graded concrete for Oklahoma, OTCREOS11, (2013) 1-39.
[99] M.D. Cook, A. Ghaeezadah, M.T. Ley, Impacts of Coarse-Aggregate Gradation on the Workability of Slip-Formed Concrete, Journal of Materials in Civil Engineering, 30 (2017) 04017265.
[100] G.H. Tattersall, Workability and quality control of concrete, CRC Press2003.
[101] C.F. Ferraris, N.S. Martys, Relating fresh concrete viscosity measurements from different rheometers, Journal of research of the National Institute of Standards and Technology, 108 (2003) 229.
[102] E.P. Koehler, D.W. Fowler, C.F. Ferraris, S. Amziane, A new, portable rheometer for fresh self-consolidating concrete, ACI SPECIAL PUBLICATIONS, 233 (2005) 97.
[103] Q. Hu, M. Aboustait, T. Kim, M.T. Ley, J.C. Hanan, J. Bullard, R. Winarski, V. Rose, Direct three-dimensional observation of the microstructure and chemistry of C 3 S hydration, Cement and Concrete Research, 88 (2016) 157-169.
[104] Q. Hu, M. Aboustait, T. Kim, M.T. Ley, J.W. Bullard, G. Scherer, J.C. Hanan, V. Rose, R. Winarski, J. Gelb, Direct measurements of 3d structure, chemistry and mass density during the induction period of C 3 s hydration, Cement and Concrete Research, 89 (2016) 14-26.
[105] T. Suzuki, H. Ogata, R. Takada, M. Aoki, M. Ohtsu, Use of acoustic emission and X-ray computed tomography for damage evaluation of freeze-thawed concrete, Construction and Building Materials, 24 (2010) 2347-2352.
[106] P.J. Monteiro, A. Kirchheim, S. Chae, P. Fischer, A.A. MacDowell, E. Schaible, H. Wenk, Characterizing the nano and micro structure of concrete to improve its durability, Cement and Concrete Composites, 31 (2009) 577-584.
[107] S. Erdoğan, E.J. Garboczi, D. Fowler, Shape and size of microfine aggregates: X-ray microcomputed tomography vs. laser diffraction, Powder Technology, 177 (2007) 53-63.
[108] R. Wong, K. Chau, Estimation of air void and aggregate spatial distributions in concrete under uniaxial compression using computer tomography scanning, Cement and Concrete Research, 35 (2005) 1566-1576.
[109] E. Masad, V. Jandhyala, N. Dasgupta, N. Somadevan, N. Shashidhar, Characterization of air void distribution in asphalt mixes using X-ray computed tomography, Journal of materials in civil engineering, 14 (2002) 122-129.
[110] K.Y. Kim, T.S. Yun, J. Choo, D.H. Kang, H.S. Shin, Determination of air-void parameters of hardened cement-based materials using X-ray computed tomography, Construction and Building Materials, 37 (2012) 93-101.
[111] T.T. Nguyen, Modeling of complex microcracking in cement based materials by combining numerical simulations based on a phase-field method and experimental 3D imaging, Université Paris-Est, 2015.
[112] P. Trtik, A. Diaz, M. Guizar-Sicairos, A. Menzel, O. Bunk, Density mapping of hardened cement paste using ptychographic X-ray computed tomography, Cement and Concrete Composites, 36 (2013) 71-77.
[113] E. Gallucci, K. Scrivener, A. Groso, M. Stampanoni, G. Margaritondo, 3D experimental investigation of the microstructure of cement pastes using synchrotron X-ray microtomography (μCT), Cement and Concrete Research, 37 (2007) 360-368.

[114] N. Otsu, A threshold selection method from gray-level histograms, IEEE transactions on systems, man, and cybernetics, 9 (1979) 62-66.
[115] P. Makkar, A. Pundir, Image analysis using improved Otsu's thresholding method, International Journal on Recent and Innovation Trends in Computing and Communication, 2 (2014) 2122-2126.
[116] T. Kurita, N. Otsu, N. Abdelmalek, Maximum likelihood thresholding based on population mixture models, Pattern recognition, 25 (1992) 1231-1240.
[117] L. Jianzhuang, L. Wenqing, T. Yupeng, Automatic thresholding of gray-level pictures using two-dimension Otsu method, Circuits and Systems, 1991. Conference Proceedings, China., 1991 International Conference on, IEEE, 1991, pp. 325-327.
[118] R.A. Ketcham, Computational methods for quantitative analysis of three-dimensional features in geological specimens, Geosphere, 1 (2005) 32-41.
[119] M. Coster, J.-L. Chermant, Image analysis and mathematical morphology for civil engineering materials, Cement and Concrete Composites, 23 (2001) 133-151.
[120] J. Serra, Image analysis and mathematical morphology, v. 1, Academic press1982.
[121] K. Pulli, M. Pietikäinen, Range image segmentation based on decomposition of surface normals, Proceedings of the Scandinavian conference on image analysis, PROCEEDINGS PUBLISHED BY VARIOUS PUBLISHERS, 1993, pp. 893-893.
[122] F.A. Jassim, F.H. Altaani, Hybridization of Otsu method and median filter for color image segmentation, arXiv preprint arXiv:1305.1052, (2013).
[123] M.D. Cook, Aggregate proportioning for slip formed pavements and flowable concrete, Oklahoma State University, 2015.
[124] G. Fagerlund, Critical degrees of saturation at freezing of porous and brittle materials, Division of Building technology, Lund Institute of Technology, 1972.
[125] G.G. Litvan, Frost action in cement paste, Mater Struct, 6 (1973) 293-298.
[126] G.W. Scherer, Crystallization in pores, Cement Concrete Res, 29 (1999) 1347-1358.
[127] G.W. Scherer, J.J. Valenza, Mechanisms of frost damage, Materials science of concrete, 7 (2005) 209-246.
[128] W.T. Li, M. Pour-Ghaz, J. Castro, J. Weiss, Water Absorption and Critical Degree of Saturation Relating to Freeze-Thaw Damage in Concrete Pavement Joints, J Mater Civil Eng, 24 (2012) 299-307.
[129] G. Fagerlund, The critical degree of saturation method of assessing the freeze/thaw resistance of concrete, Mater Struct, 10 (1977) 217-229.
[130] W. Li, M. Pour-Ghaz, J. Castro, J. Weiss, Water absorption and critical degree of saturation relating to freeze-thaw damage in concrete pavement joints, J Mater Civil Eng, 24 (2011) 299-307.
[131] T.C. Powers, T.F. Willis, The air requirement of frost resistant concrete, Highway Research Board Proceedings, 1950.
[132] H.S. Shang, Y.P. Song, J.P. Ou, Behavior of Air-Entrained Concrete after Freeze-Thaw Cycles, Acta Mech Solida Sin, 22 (2009) 261-266.
[133] Z.H. Sun, G.W. Scherer, Effect of air voids on salt scaling and internal freezing, Cement Concrete Res, 40 (2010) 260-270.
[134] Z. Yang, W.J. Weiss, J. Olek, Water transport in concrete damaged by tensile loading and freeze–thaw cycling, J Mater Civil Eng, 18 (2006) 424-434.

[135] T. Akçaoğlu, M. Tokyay, T. Çelik, Assessing the ITZ microcracking via scanning electron microscope and its effect on the failure behavior of concrete, Cement Concrete Res, 35 (2005) 358-363.
[136] G.W. Scherer, J. Valenza, Mechanisms of frost damage, Materials science of concrete, 7 (2005) 209-246.
[137] T.C. Powers, R.A. Helmuth, Theory of volume changes in hardened portland-cement paste during freezing, In Highway research board proceedings, 1953.
[138] A. Ammouche, J. Riss, D. Breysse, J. Marchand, Image analysis for the automated study of microcracks in concrete, Cement Concrete Comp, 23 (2001) 267-278.
[139] M. Elzafraney, P. Soroushian, Assessment of microcrack development in concrete materials of different strengths, Mater Struct, 37 (2004) 724-731.
[140] S. Jacobsen, J. Marchand, H. Hornain, Sem Observations of the Microstructure of Frost Deteriorated and Self-Healed Concretes, Cement Concrete Res, 25 (1995) 1781-1790.
[141] A. Litorowicz, Identification and quantification of cracks in concrete by optical fluorescent microscopy, Cement Concrete Res, 36 (2006) 1508-1515.
[142] M.A.B. Promentilla, T. Sugiyama, X-Ray Microtomography of Mortars Exposed to Freezing-Thawing Action, J Adv Concr Technol, 8 (2010) 97-111.
[143] T. Sugiyama, M.A.B. Promentilla, T. Hitomi, N. Takeda, Application of synchrotron microtomography for pore structure characterization of deteriorated cementitious materials due to leaching, Cement Concrete Res, 40 (2010) 1265-1270.
[144] I. Tekin, R. Birgul, H.Y. Aruntas, Determination of the effect of volcanic pumice replacement on macro void development for blended cement mortars by computerized tomography, Constr Build Mater, 35 (2012) 15-22.
[145] A.J. Mattana, E. Pereira, M.M. Costa, EVALUATION OF POROSITY IN MORTAR BY X-RAY MICROTOMOGRAPHY (MICRO-CT) AS AN ADDITIONAL TOOL FOR MERCURY INTRUSION POROSIMETRY, Iberoamerican Journal of Applied Computing, 4 (2014).
[146] H. Lu, K. Peterson, O. Chernoloz, Measurement of entrained air-void parameters in Portland cement concrete using micro X-ray computed tomography, International Journal of Pavement Engineering, (2016) 1-13.
[147] S. Lu, E.N. Landis, D.T. Keane, X-ray microtomographic studies of pore structure and permeability in Portland cement concrete, Mater Struct, 39 (2006) 611-620.
[148] Y. Shields, E.J. Edward J. Garboczi, J. Weiss, Y. Farnam, Freeze-Thaw Crack Determination in Cementitious Materials Using 3D X-ray Computed Tomography and Acoustic Emission, Cement Concrete Comp, (Submitted).
[149] R. De Borst, L.J. Sluys, H.B. Muhlhaus, J. Pamin, Fundamental issues in finite element analyses of localization of deformation, Engineering computations, 10 (1993) 99-121.
[150] N. Lenoir, M. Bornert, J. Desrues, P. Besuelle, G. Viggiani, Volumetric digital image correlation applied to X-ray microtomography images from triaxial compression tests on argillaceous rock, Strain, 43 (2007) 193-205.
[151] S. Diamond, Mercury porosimetry - An inappropriate method for the measurement of pore size distributions in cement-based materials, Cement and Concrete Research, 30 (2000) 1517-1525.

[152] M. Wyrzykowski, P. Trtik, B. Munch, J. Weiss, P. Vontobel, P. Lura, Plastic shrinkage of mortars with shrinkage reducing admixture and lightweight aggregates studied by neutron tomography, Cement Concrete Res, 73 (2015) 238-245.
[153] P. Makkar, A. Pundir, Image analysis using improved Otsu's thresholding method, International Journal on Recent andInnovation Trends in Computing and Communication, 2 (2014) 2122-2126.
[154] N. Otsu, A threshold selection method from gray-level histograms, Automatica, 11 (1975) 23-27.
[155] T. Kurita, N. Otsu, N. Abdelmalek, Maximum-Likelihood Thresholding Based on Population Mixture-Models, Pattern Recogn, 25 (1992) 1231-1240.
[156] A. Suryavanshi, J. Scantlebury, S. Lyon, Mechanism of Friedel's salt formation in cements rich in tri-calcium aluminate, Cement Concrete Res, 26 (1996) 717-727.
[157] Y. Farnam, D. Bentz, A. Hampton, W. Weiss, Acoustic emission and low-temperature calorimetry study of freeze and thaw behavior in cementitious materials exposed to sodium chloride salt, Transportation Research Record: Journal of the Transportation Research Board, (2014) 81-90.
[158] T.R. Jensen, A.N. Christensen, J.C. Hanson, Hydrothermal transformation of the calcium aluminum oxide hydrates CaAl2O4· 10H2O and Ca2Al2O5· 8H2O to Ca3Al2 (OH) 12 investigated by in situ synchrotron X-ray powder diffraction, Cement Concrete Res, 35 (2005) 2300-2309.
[159] T.C. Powers, T. Willis, The air requirement of frost resistant concrete, Highway Research Board Proceedings, 1950.
[160] G. Skripkiūnas, D. Nagrockienė, G. Girskas, M. Vaičienė, E. Baranauskaitė, The cement type effect on freeze–thaw and deicing salt resistance of concrete, Procedia Engineering, 57 (2013) 1045-1051.
[161] J. Kaufmann, W. Studer, Comparison of Frost deicing Salt Damage Mechanisms in Field and Laboratory Conditions, Proc. Consec, 98 (1998) 262.
[162] C.L. Lucero, R.P. Spragg, D.P. Bentz, D.S. Hussey, D.L. Jacobson, W.J. Weiss, Neutron Radiography Measurement of Salt Solution Absorption in Mortar, ACI materials journal, 114 (2017) 149.
[163] E.S. Sumsion, W.S. Guthrie, Physical and Chemical Effects of Deicers on Concrete Pavement: Literature Review, 2013.
[164] S. Mindess, J.F. Young, D. Darwin, Concrete, Prentice Hall2003.
[165] V.C. Tidwell, L.C. Meigs, T. Christian-Frear, C.M. Boney, Effects of spatially heterogeneous porosity on matrix diffusion as investigated by X-ray absorption imaging, Journal of Contaminant Hydrology, 42 (2000) 285-302.
[166] S.J. Altman, M. Uchida, V.C. Tidwell, C.M. Boney, B.P. Chambers, Use of X-ray absorption imaging to examine heterogeneous diffusion in fractured crystalline rocks, Journal of contaminant hydrology, 69 (2004) 1-26.
[167] L. Cavé, T. Al, Y. Xiang, P. Vilks, A technique for estimating one-dimensional diffusion coefficients in low-permeability sedimentary rock using X-ray radiography: comparison with through-diffusion measurements, Journal of contaminant hydrology, 103 (2009) 1-12.
[168] A. Atkinson, A. Nickerson, The diffusion of ions through water-saturated cement, Journal of materials science, 19 (1984) 3068-3078.

[169] A. Atkinson, A.K. Nickerson, Diffusion and sorption of cesium, strontium, and iodine in water-saturated cement, Nuclear Technology, 81 (1988) 100-113.
[170] M.K. Moradllo, Q. Hu, M.T. Ley, Using X-ray imaging to investigate in-situ ion diffusion in cementitious materials, Construction and Building Materials, 136 (2017) 88-98.
[171] X. Shi, L. Fay, M.M. Peterson, Z. Yang, Freeze–thaw damage and chemical change of a portland cement concrete in the presence of diluted deicers, Materials and Structures, 43 (2010) 933-946.
[172] R. Pleau, M. Pigeon, J.-L. Laurencot, Some findings on the usefulness of image analysis for determining the characteristics of the air-void system on hardened concrete, Cement and Concrete Composites, 23 (2001) 237-246.
[173] E.K. Nambiar, K. Ramamurthy, Air-void characterisation of foam concrete, Cement and concrete research, 37 (2007) 221-230.
[174] M. Pigeon, R. Gagne, C. Foy, Critical air-void spacing factors for low water-cement ratio concretes with and without condensed silica fume, Cement and Concrete Research, 17 (1987) 896-906.
[175] H. Lu, K. Peterson, O. Chernoloz, Measurement of entrained air-void parameters in Portland cement concrete using micro X-ray computed tomography, International Journal of Pavement Engineering, 19 (2018) 109-121.

APPENDICES

Appendix-A

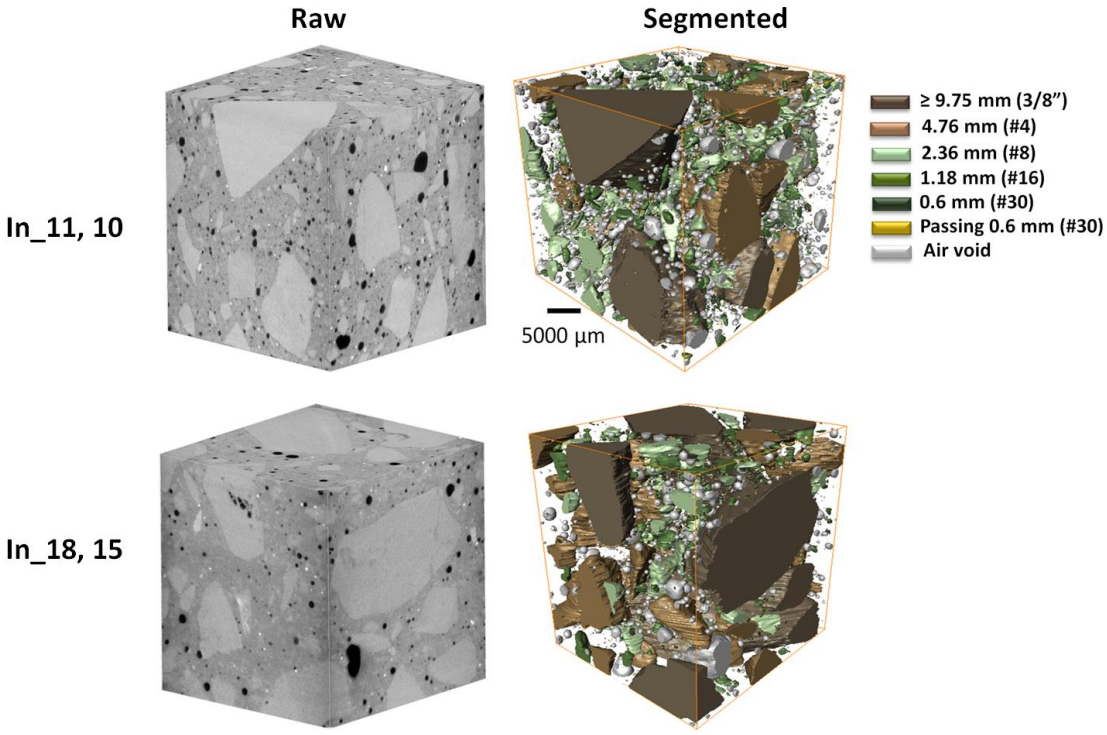

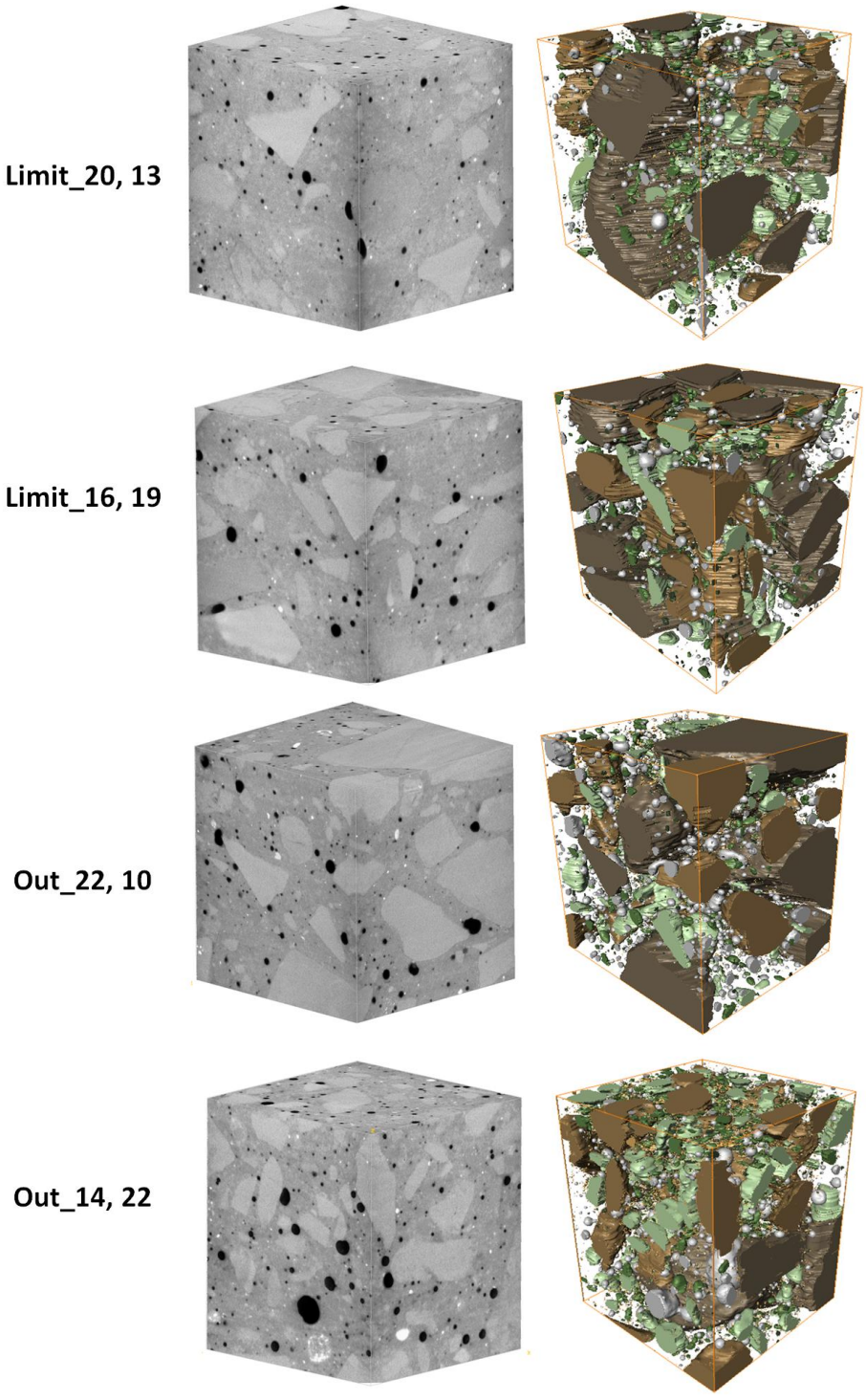

Fig. A1. 3D rendering of the raw and segmented XCT data for different samples.

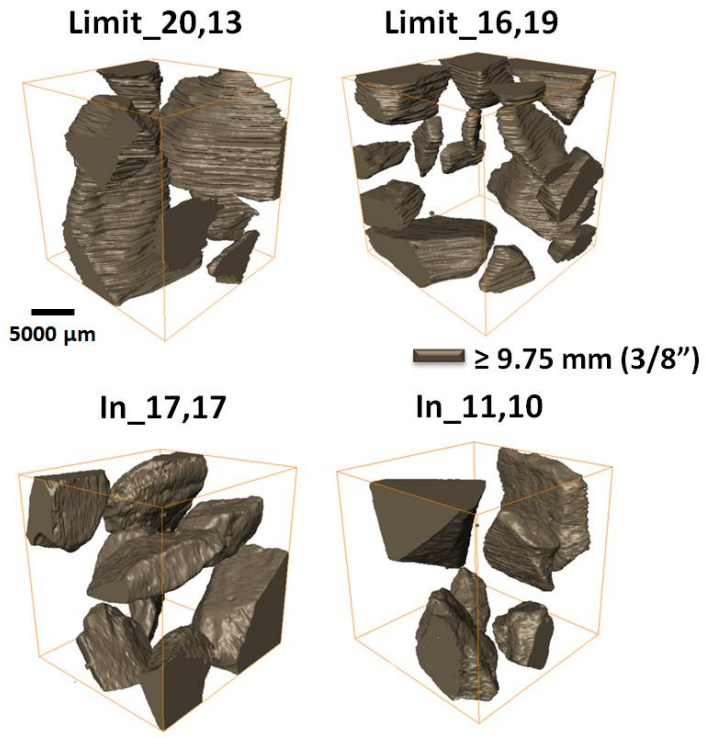

Fig. A2. 3D renderings aggregate retained on sieves ≥ 9.75 mm for different samples.

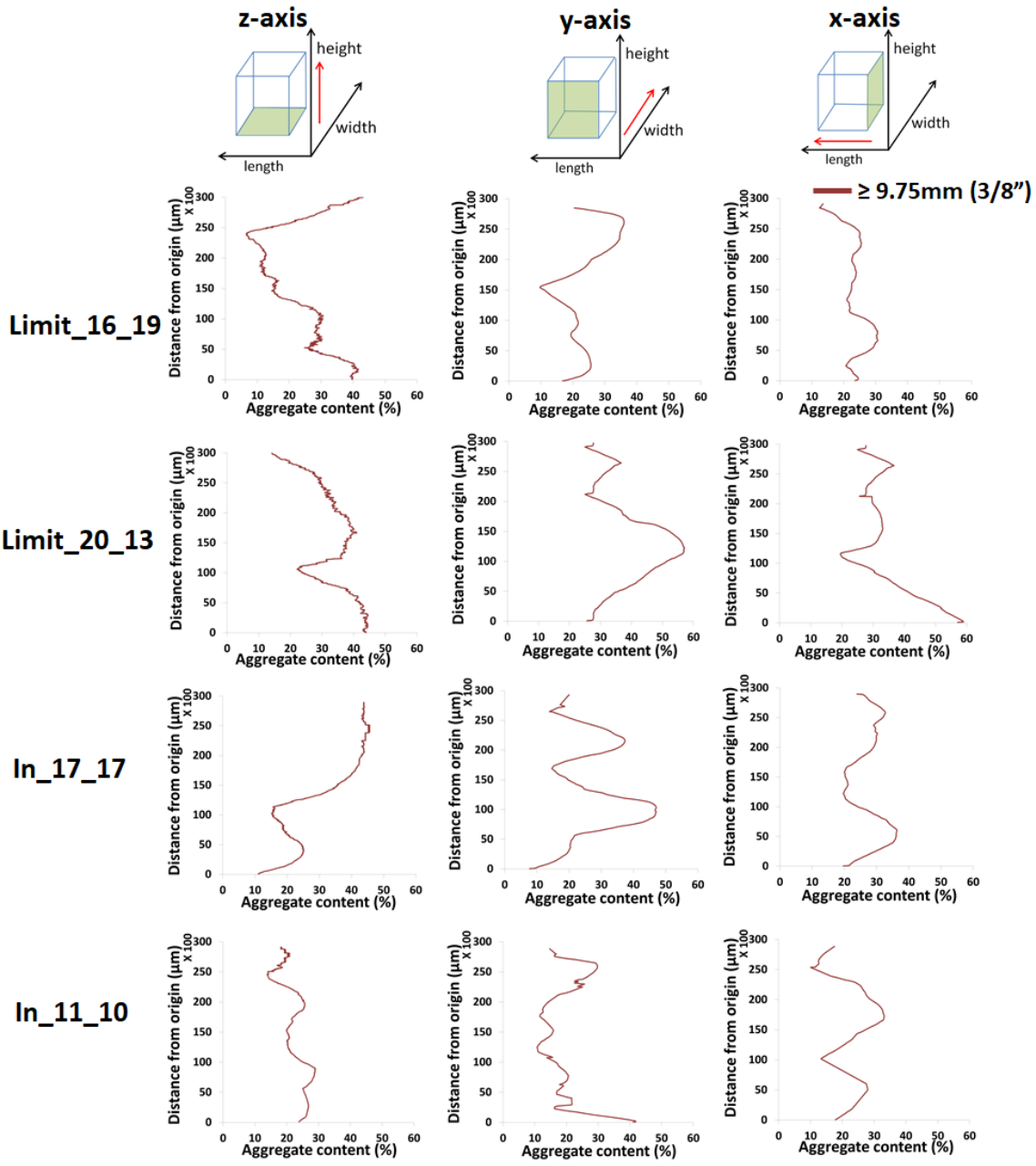

Fig. A3. Volume percentage of different aggregate sizes at different distances from the origin of VOI.

Appendix-B

Gray value histogram and the normal distribution of aggregates

The histogram of the measured mean gray values of aggregates in nAE_100 is plotted in Figure B1 and a normal distribution curve is fitted to the histogram suggesting the distribution of gray values of aggregates. As shown in the figure, the probabilities of existence of data within one, two, and three standard deviations away from the average in a normal distribution are 65%, 95%, and 99.7%, respectively. In this study, two standard deviations away from mean of aggregates' gray value is used as a threshold value for segmenting aggregates. Therefore, it is estimated that 95% of aggregate have been determined in the selected range.

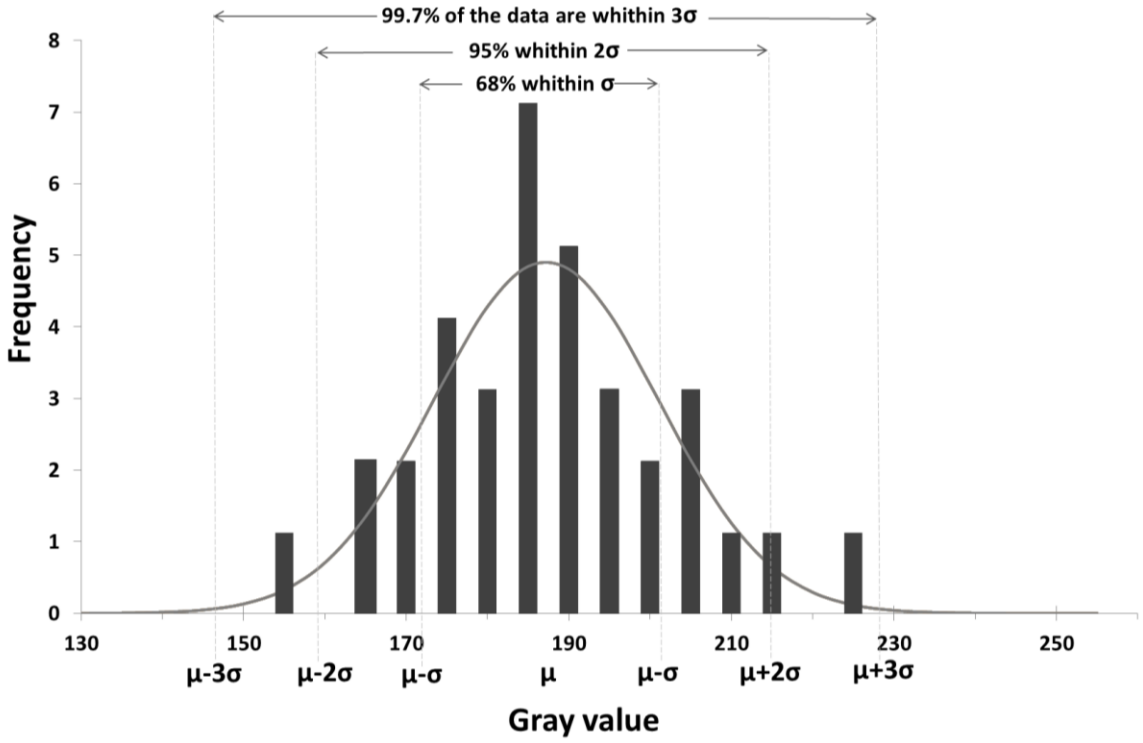

Fig. B.1. A normal distribution curve fitted to the gray values of aggregates in mortar sample nAE_100.

Initiation and propagation of cracks

Figure B.2 shows the 3D rendering of the crack both before and after a freeze-what cycle for all samples expect sample nAE_100. The initial scans show that all samples had some cracks before it was exposed to the freeze-thaw cycles. However, no new crack initiation or propagation was observed after freeze-thaw cycles.

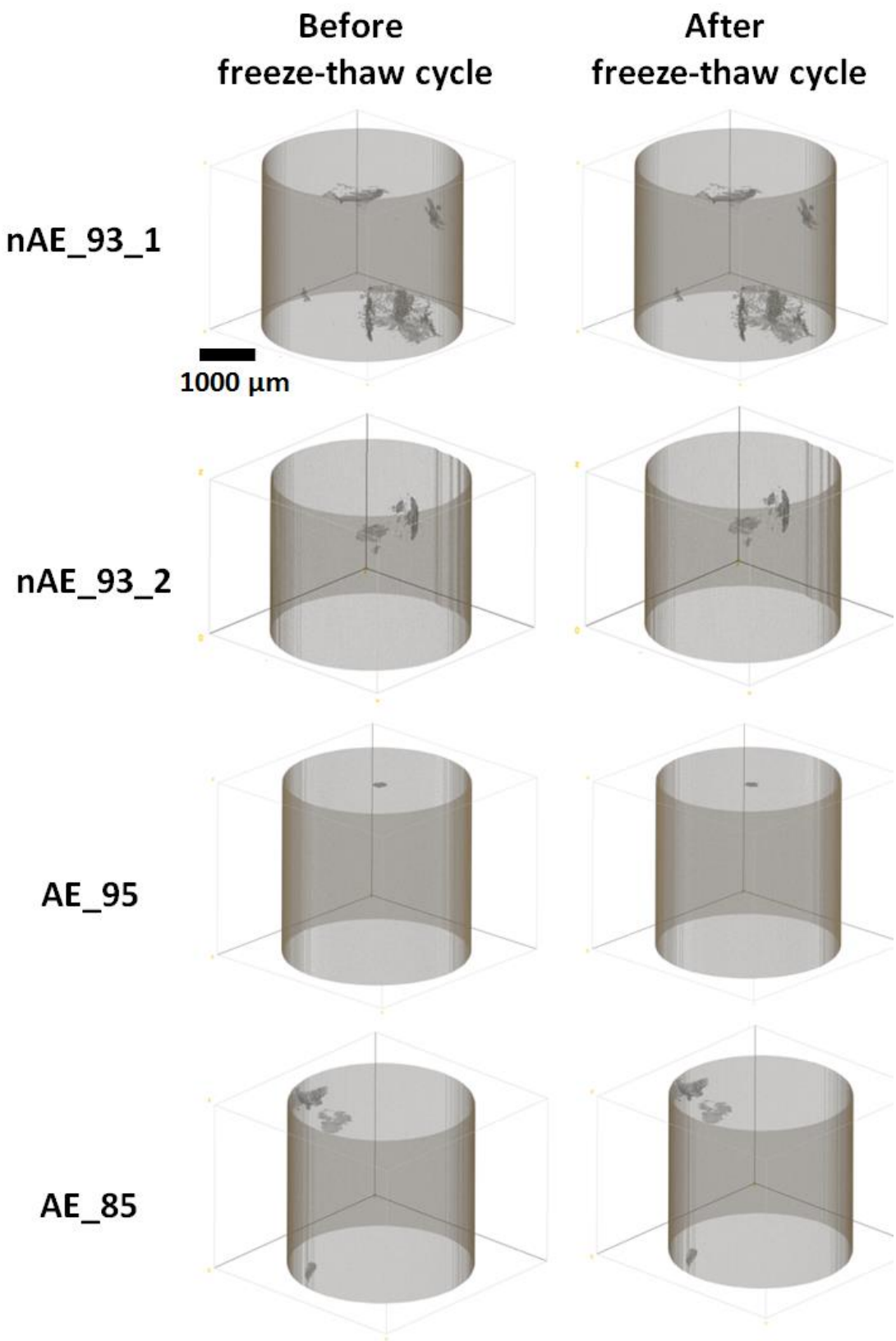

Fig. B.2. The 3D rendering of cracks before and after freeze-thaw cycle.

Appendix-C

Imaging techniques

Properties of a material are related to its structure [1, 2]. Therefore, better understanding of the microstructure of a material will allow insights into improving their characteristics and producing materials that are high quality, sustainable and cost-efficient.

The smallest particle size that can be seen with the unaided human eye is 0.1 mm (100 Micron) [3]. This is roughly equal to the width of 2 human hairs. However, a range of microscopy techniques have been developed to investigate the microstructure of materials. Optical or light microscope was the first generation of microscope to uses visible light and a system of lenses to observe small objects [4]. Further developments came with electron microscopy such as scanning electron microscopy (SEM) or transmission electron microscopy (TEM) [5, 6]. Although these techniques provide images with high resolutions, the observations can be only made on the exposed surface and often in high vacuum and with special sample preparation. These observations may not necessarily be representative of the material being investigated [7, 8]. What is needed is a technique that investigates the 3D microstructure of materials with minimal sample preparation.

XCT

X-ray computed tomography (XCT) is a powerful non-destructive tool that can be used to investigate the 3D microstructure of materials. It has been widely used in medical science to investigate biological organisms [9-11]. This method has also been used to study construction materials. Some examples include cement hydration [10, 12], aggregate spatial distribution [13-15], transport properties [16, 17], crack propagation [18-20], and air void distribution [21-23]. In this method, a series of 2D X-ray radiographs are captured from different viewing angles and the collected data sets are used to build a 3D measurement of the internal structure called a tomograph. The tomograph can be then used for qualitative and quantitative analyses [24-27]. The gray values in the produced images corresponds to X-ray absorption which is a function of density and composition of the material [28, 29]. The gray value contrast can be used to separate the materials into different constituent phases [15, 19, 21]. This process is called segmentation.

Image processing

After collecting the XCT dataset, the reconstructed images are analyzed to extract useful information. This process is called image processing. Pre-processing, segmentation, and data interpretation are the main steps of a typical image processing for analyzing XCT datasets.

Pre-processing

Image pre-processing aims to enhance and modify some image features which are important for further processing. Noise reduction by smoothing filters is very typical in image pre-processing. There are various smoothing filters that can be used in image pre-processing such as median filter, Gaussian smoothing, and morphological operators

(erode, dilate, open, and close). As an example, median filter is one of the most common filters that removes noise in the reconstructed image without blurring the edge when the radius is small [121, 122]. Figure C.1 shows the procedure of median filter with radius of 3 pixels. As shown in the figure, the filter replaces each pixel value with the median of the gray values in the neighborhood of the pixel.

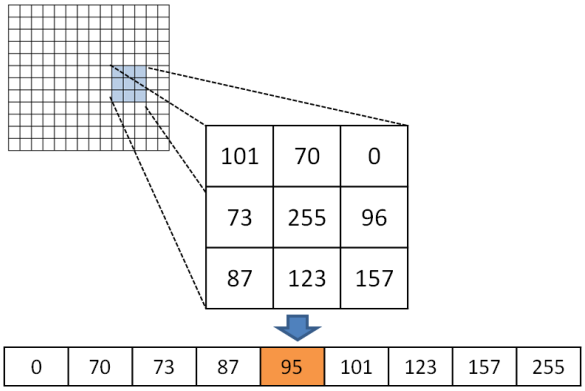

Fig. C.1. Procedure of median filter

Figure C.2 shows an example of the median filter result with different radiuses applied on the XCT reconstructed concrete image. The size of the filter controls degree of smoothing. Larger filter radius leads to larger neighborhood and results in intensive smoothing. According to this figure, the image with 5 pixels median filter experiences intensive smoothing compared to the image with applied median filter of 2 pixels.

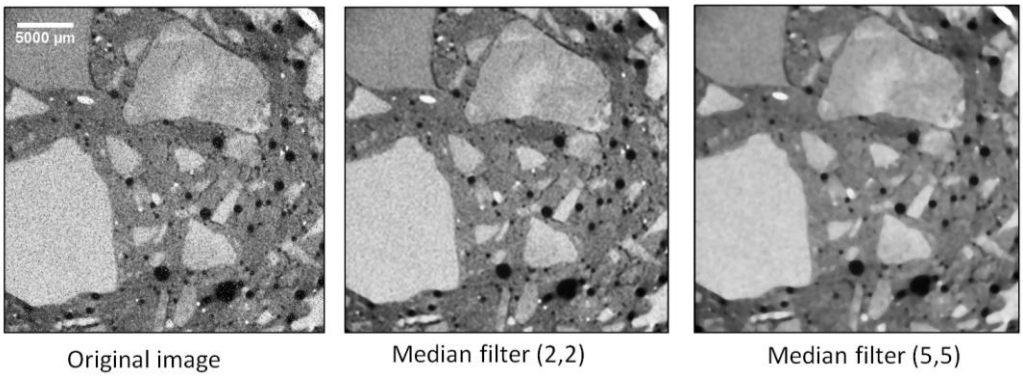

Fig. C.2. An example of the median filter result with different radiuses applied on the XCT reconstructed concrete image

Segmentation

After image pre-processing, the difference in the gray value or the contrast of the images can be evaluated to separate the images into regions of different constituents. This process is called segmentation [21]. The segmentation is the most challenging part of the

image processing. A segmentation method that is useful for one XCT datasets may not be helpful to the segment material constituents in another XCT datasets. Typically, the segmentation methods are separated into automated and manual methods.

Automated segmentation method

The automated methods are based on the mathematical algorithms. The Otsu method is the most commonly used automated technique. In this popular method, a single threshold value is selected by minimizing the mean square errors between the original and binarized images. More information about this method can be found in other publications [114-117]. Figure C.3 and C.4 show examples of the Otsu segmentation method performance used to segment air voids in a 2D reconstructed concrete image. Figure C.3 shows an example of a 2D reconstructed concrete image with corresponding histogram of the gray value and Figure C.4 shows the Otsu segmentation procedure. In Figure C.3, the major concrete constituents are air voids, aggregates, and OPC paste. The air voids have the lowest X-ray absorption while the aggregates have the highest X-ray absorption in XCT dataset. According to the XCT histogram shown in this figure, the Otsu method works well for air void segmentation because the gray value contrast of voids are high. Figure C.4 gives an overview of how this method is completed.

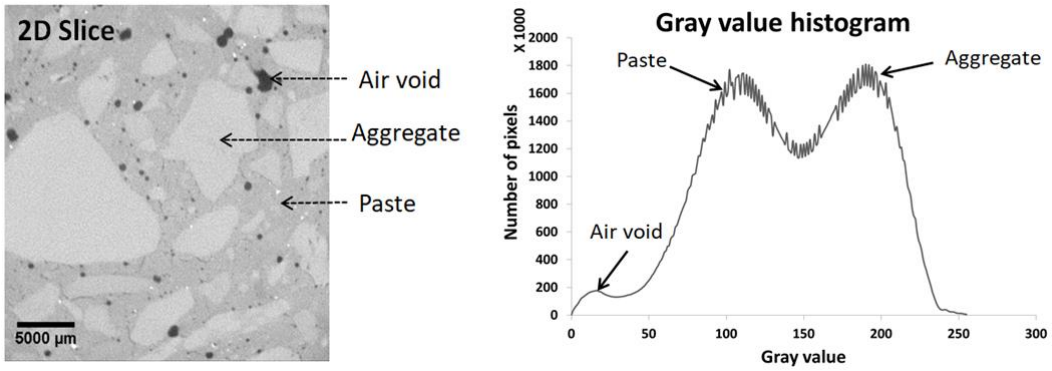

Fig. C.3. A typical XCT dataset showing 2D cross section of the reconstructed concrete image and corresponding gray scale histogram.

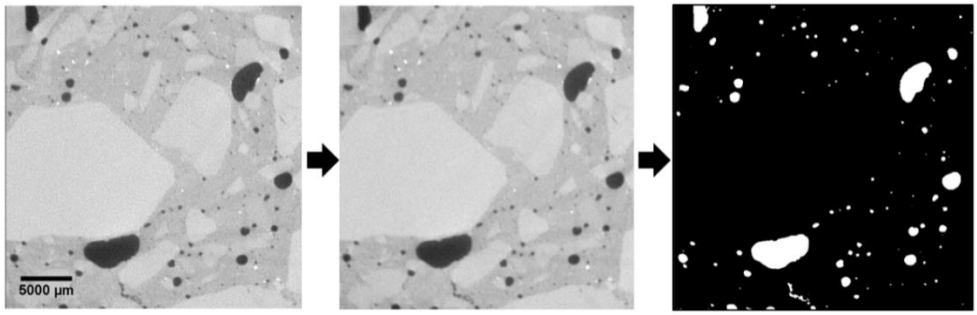

Fig. C.4. Procedure for segmentation of air voids.

While the Otsu thresholding method was useful to segment the air voids, it was not helpful to separate the aggregates from the paste since the peaks in the gray level histogram overlap. In order to resolve this issue, image pre-processing and post-processing was used first and then the Otsu method was used. This procedure for fine and coarse aggregates is shown in Figure C.5. To segment the coarse aggregates, a median filter with a radius of 5 pixels was applied on the reconstructed image. A larger radius filter creates intensive smoothing and eliminates some details; however, it is useful to identify the larger objects in the image. The Otsu thresholding was then applied to the filtered image. However, the resulting image contained some kind of distortion as shown in Figure C.5. Therefore, two morphological analyses "erosion" and "fill holes" were used to distinguish aggregates and fill probable spots inside of the segmented aggregate created by noise. In this process, erosion removes voxels from the outer surface of the objects in a binary image to separate the connected aggregates, while the filling operator fills holes in a binary image [118-120].

In order to segment the fine aggregates, a 3-pixel radius median filter with was used in the reconstructed image. The median filter removes noise in the reconstructed image without blurring the edge when the radius is small [121, 122]. The Otsu thresholding method was then applied to the filtered image. Next, the previously segmented coarse aggregates were subtracted and a morphological operator (erosion) was applied to the result to remove the connection between the fine aggregates. Finally, the results obtained from the fine and coarse aggregate segmentation were combined to generate the segmented aggregate image.

After identifying the air voids and the aggregates, the remaining materials were assumed to be the cement paste.

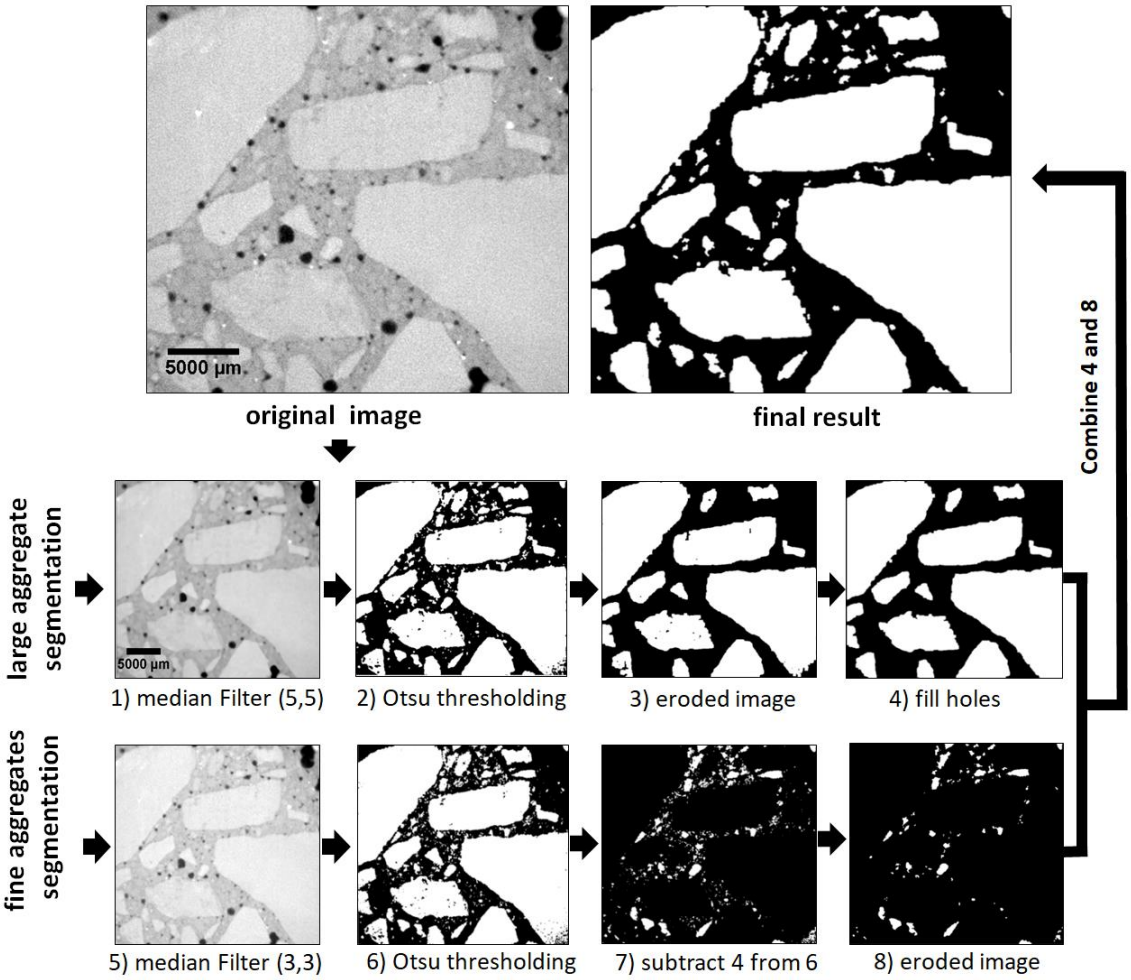

Fig. C.5. segmentation procedure of aggregates

Manual segmentation method

As mentioned earlier, automated segmentation algorithms are not useful to calculate the optimal threshold in materials with no distinct peaks or valleys in their gray value histogram. Therefore, manual segmentation methods can be used to segment these types of XCT datasets. In this segmentation method, the threshold (a single gray value) is chosen manually. "Local mean and standard deviation" method is a well stablished manual segmentation method. Figure C.6, C.7 and C.8 show an example of this segmentation procedures applied to segment biomass constituents in Chapter 2.

Figure C.6 shows an example of a 2D cross-section of the reconstructed tomograph and corresponding grayscale histogram for a raw switchgrass particle. Based on inspection of the cross-sections and the histogram, there are materials with three different and distinct gray values. These different gray values represent materials with different densities: very low, intermediate and very high – these constituents have been labeled air, biomass, and high density materials respectively. These materials are noted in Figure C.6.

According to Figure C.6 there is some overlap in the gray values for the constituents mostly due to resolution effects at particle edges which makes quantitative segmentation more challenging. To decide on a useful segmentation range for each constituent, local regions of the cross-section were investigated that were clearly one of the three constituents. An example of such a "typical" region is shown as the dashed polygon in Figure 2.3. For each constituent, 20 different typical regions were selected and the average and standard deviation (STD) of the gray value for each constituent were recorded.

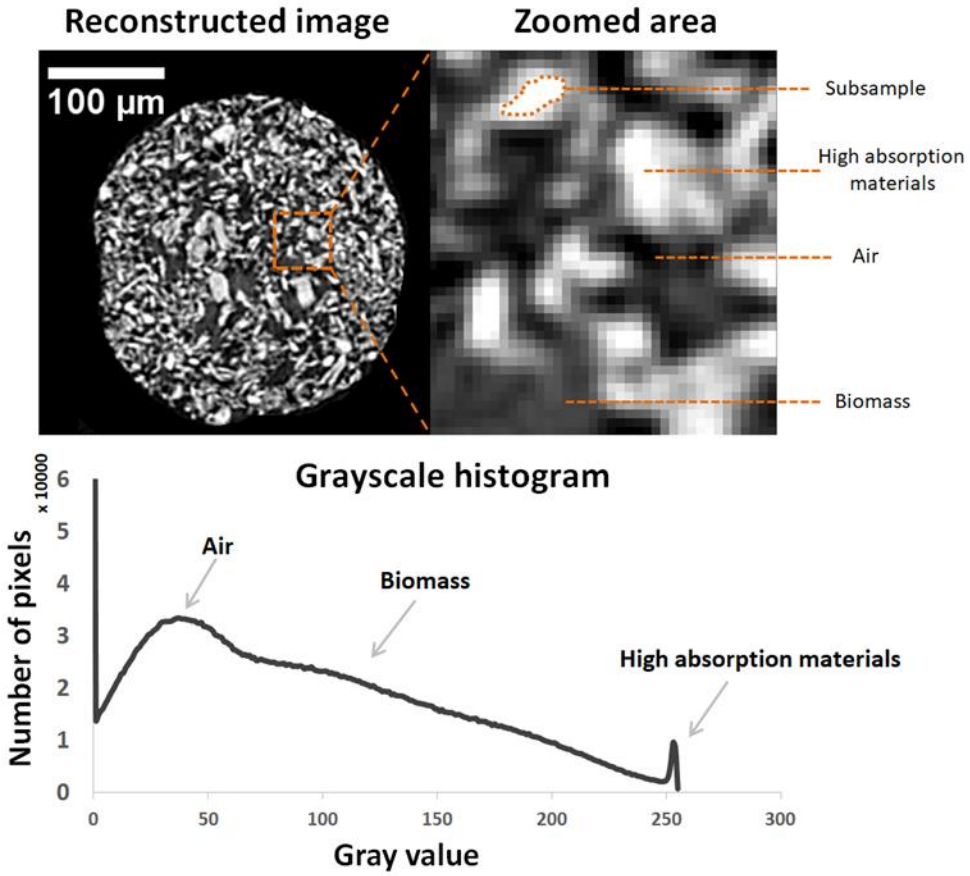

Fig. C.6. An example of 2D cross-section of the reconstructed and corresponding grayscale histogram for a raw switchgrass particle. Zoomed area is highlighted as the dashed line in the reconstructed images.

Different multiples of the standard deviations were investigated to examine how it changes the results for each material. Figure C.7 shows two example of 2D cross-sections, a zoomed area, and the segmented images of the zoomed area acquired from 2.5 standard deviations of the mean. The segmented image shows the voids in black, the high absorption in white, and the biomass in gray. The thresholds obtained from different standard deviations are shown in the grayscale histogram of the raw and charred switchgrass particles. If the gray value is assumed to be normally distributed for each

biomass constituent, between 69% and 99.7% of the materials would be within one and three standard deviations away from the mean, respectively. Therefore, by visual inspections of segmented images obtained from each threshold results, it was decided that the best threshold for segmentation is 2.5 standard deviations for the air and high absorption materials. The remaining material was then assigned to be biomass and is shown as gray in figure C.7. An example segmentation result for each constituent in the raw and charred switchgrass particle is shown in Figure C.8. This figure shows the voids in black, the high absorption in white, and the biomass in gray in the final segmentation results. This segmentation method was also applied to other biomass particle images.

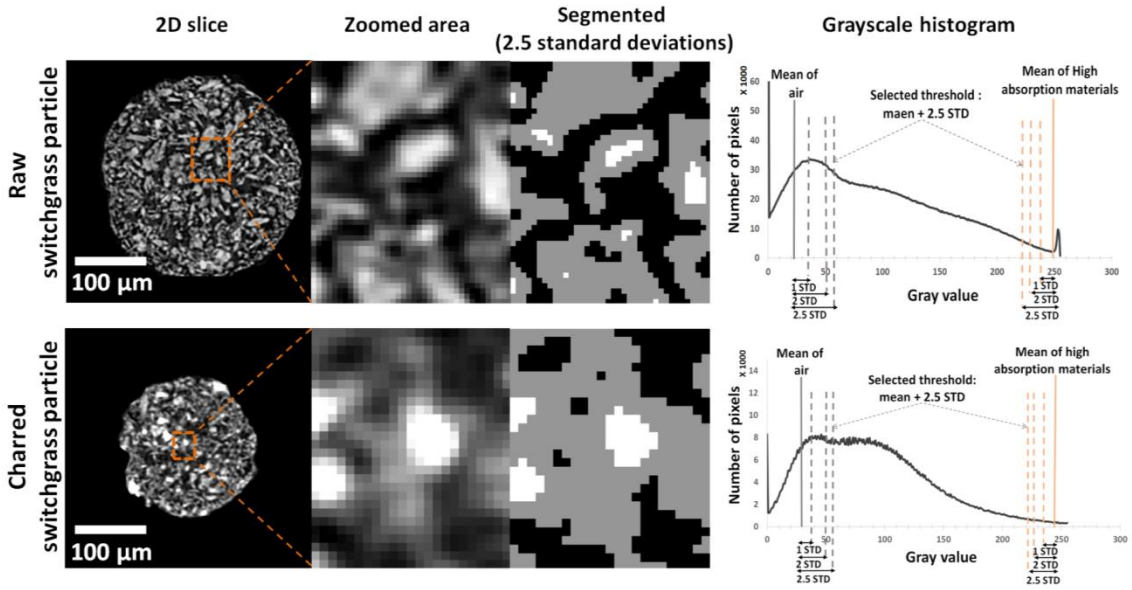

Fig. C.7. An example of a 2D cross-section, a segmented image with the 2.5 standard deviations as a threshold, and corresponding grayscale histogram for a raw and charred switchgrass particle. Zoomed area is highlighted as orange dash line in the reconstructed images.

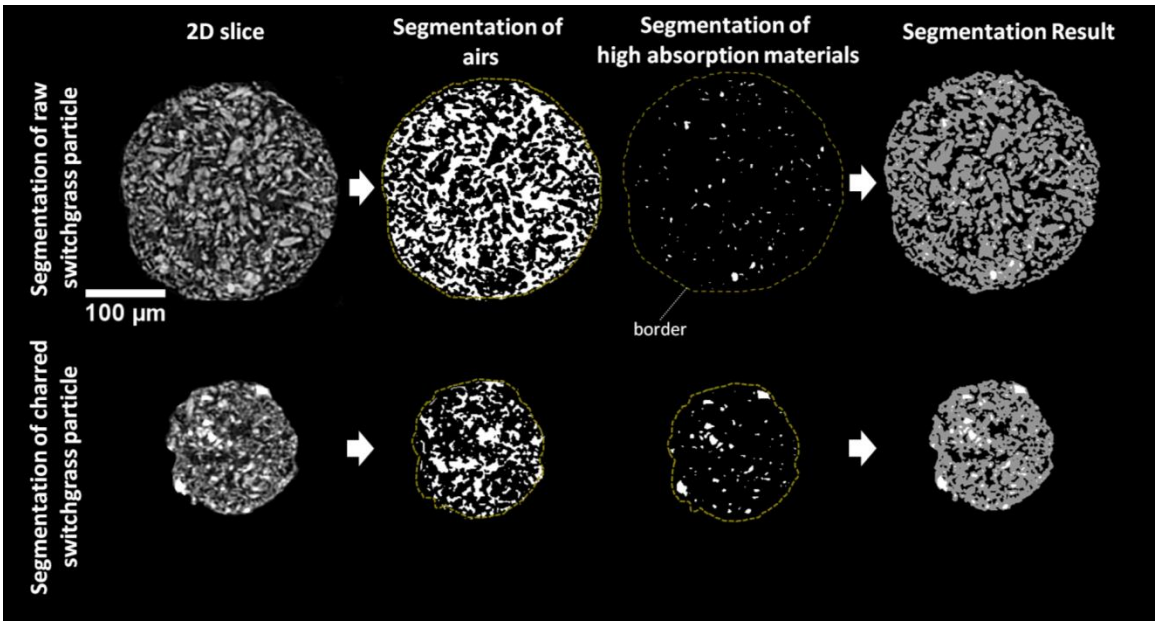

Fig. C.8. An example of segmentation results for each constituent of raw and charred switchgrass particle.

Data interpretation

The 3D segmented XCT datasets can be then used for data interpretation which is the final step of image processing. Based on the goals of the study, different analyses can be used to interpret the XCT datasets. In this dissertation, all data interpretations and 3D visualizations were performed by MATLAB codes, ImageJ, and Amira 4.1.1 software. The following items show some of the analyses performed in this study:

- Size distribution analysis
    - Understand physical and chemical properties of materials.
- Spatial analysis:
    - Understand spatial distribution of materials' components.
- Image subtraction
    - Find probable changes in the same sample under different conditions.

VITA

Ghazal Sokhansefat

Candidate for the Degree of

Doctor of Philosophy

Thesis: FEATURE INVESTIGATION USING MICRO COMPUTED TOMOGRAPHY WITHIN MATERIALS

Major Field: Civil Engineering

Biographical:

Education:

Completed the requirements for the Doctor of Philosophy in Civil Engineering at Oklahoma State University, Stillwater, Oklahoma in May, 2018.

Completed the requirements for the Master of Science in Surveying Engineering/GIS at University of Tehran, Tehran, Iran in 2013.

Completed the requirements for the Bachelor of Science in Civil Engineering, Surveying at K.N.T University of Technology, Tehran, Iran in 2010.

Experience:

Graduate Research Assistant, Oklahoma State University (2014-2018)

Professional Memberships:

American Concrete Institute (ACI)
The American Ceramic Society (Acers)
American Society of Civil Engineers (ASCE)
American Institute of Steel Construction (AISC)